

UPPER LIMIT ON A PALEO-EQUATORIAL RIDGE FROM A TIDALLY-DISRUPTED MOON OF MARS. B. Fan¹ and E. S. Kite^{2, 1} School of Yuanpei, Peking University, 5 Yiheyuan Road Haidian District, Beijing 100871 PRC (fanbowen@pku.edu.cn), ² Department of the Geophysical Sciences, University of Chicago, 5734 South Ellis Avenue, Chicago IL 60637 USA (kite@uchicago.edu).

Introduction: The larger Martian satellite, Phobos, is gradually evolving inwards towards Mars. Evolution studies suggest that in less than 70 Myr, the moon will be tidally torn apart. It was proposed that most of its mass will fall onto the Martian surface, leaving an equatorial ridge of debris [1], while the remaining mass will form a ring and accrete into a new satellite. This process occurs inside the synchronous orbit of Mars, which leads to an ongoing satellite-ring cycle [2] (see Figure 1). Thus, past moon disruption may have occurred and formed ridges.

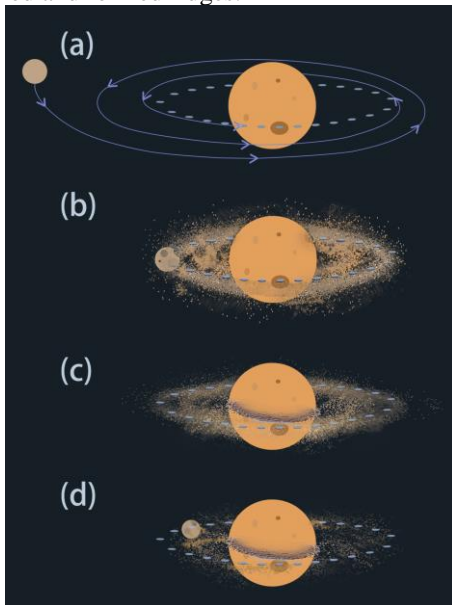


Fig. 1. An ongoing satellite-ring cycle (a) Inward evolution of Phobos (b) Phobos reaches the location of tidal breakup and break apart to form a new ring (c) Most of the ring's mass falls onto the equator, thus forming a ridge (d) The residue accretes into a new satellite.

However, no equatorial ridge-like feature was witnessed on any planets or moons in the solar system except Iapetus [3-4], Saturn's third-largest moon. Here we report our progress on a method to search for equatorial ridge by using Mars and Iapetus topography data and applying it to determine the limits of detection for an equatorial ridge on a terrestrial body like Mars.

Method: Mars and Iapetus topography data were obtained from Mars Orbiter Laser Altimeter (MOLA) and Cassini orbiter [5] separately. For Mars, geological units correspond to Amazonian, early Hesperian, volcanoes and Valles Marineris were masked out [6]. To

include cases when the ridge lies on a slope, we detrended the 2D topography by subtracting a matrix derived from averaging data in radius $\sim 2.5^\circ$ range. Then we fit the 1D zonal mean height from 20° N to 20° S to a diffusion equation for stone ruins [7].

$$h = \frac{h_0}{2x_0} \left(\operatorname{erf} \left(\frac{x + x_0}{\sqrt{4\kappa t}} \right) - \operatorname{erf} \left(\frac{x - x_0}{\sqrt{4\kappa t}} \right) \right)$$

Where x_0 is the half-width, which was set to 10 km. The key parameters for fitting are initial height h_0 and diffusivity plus time κt . Goodness of fitting ω was defined as the size of fitted ridge over normalized error.

Upper Limit on an Equatorial Ridge: The Martian spin axis may have altered significantly during the past ages [8]. If any part of the predecessor moon had fallen onto Martian surface, then much or most of the debris should be near the paleo-equator. This is because the moon will contain some large-diameter particles that are too large to be easily shifted by the wind. We considered 32310 possibilities for the paleo-equator by multiplying the topography matrix by a rotational matrix, with rotated longitude $\Delta\theta$ ranging from -179° to 180° and rotated latitude $\Delta\phi$ ranging from 1° to 90° . For each possibility we calculate goodness of fitting for the best fit, and if there was an equatorial ridge, then it would appear as a maximum on the ω -map like Figure 2.

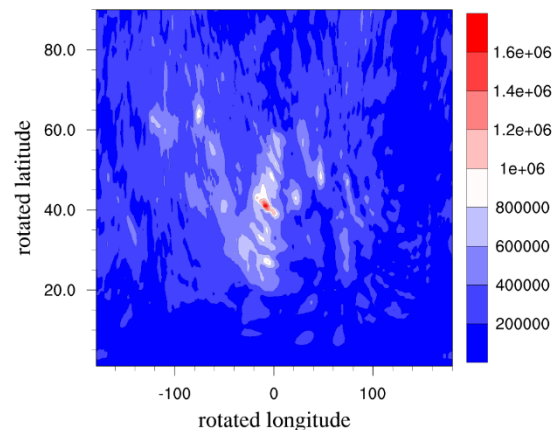


Fig. 2. Goodness of fitting for different paleo-equators. The best candidate for equatorial ridge lies in the central maximum in this map.

However, no ridge was found from the Martian topography. Then we determined our sensitivity limit by adding an equatorial ridge to the real Mars. We considered 2 cases for the equatorial ridge. The first is like

real Iapetus, which means the ridge only cover part of the longitude. In this case, the ridge can be mostly covered by lava, and we would never find it. The other is a ridge without longitudinal variation. This is possible because on Iapetus, there was probably no significant atmosphere when the ridge formed, so ring particles would be stopped only by hitting the surface. Because the surface changes during ridge formation, there is the possibility of positive feedbacks leading to longitudinal variation. On Mars however, the atmosphere can stop even quite big particles. This means that the infalling ring particles are not affected by the topography of the growing ridge, so the ridge should be longitudinally uniform. We performed "Mars + N*Iapetus ridge" for both cases with 10 randomly combined topography. As N decreases from a very large number (the ridge is very clear on the map), h_0 corresponding to the best fit of ridge decreases linearly while kt keeps a constant, meaning the fitting only shrink in size. But as N drops under a critical value N_c (~ 0.2), h_0 begins to decrease nonlinearly and kt rapidly grows to a high value meaning the fitting gradually transforms to a straight line and the ridge is too small to find (selected examples in Figure 3).

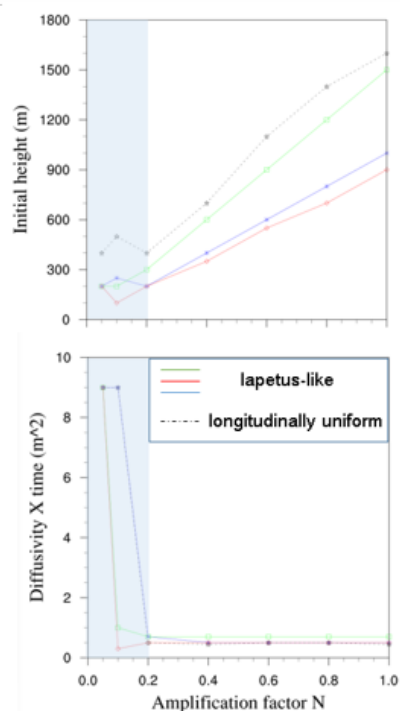


Fig. 3. Initial height and diffusivity-time product corresponding to the best fit (blue areas meaning the ridge can't be detected).

In our study, we define N_c to be the number at which the point corresponding "added ridge" drops out of first 3 maximum areas on ω -map. At $N=N_c$, the ridge is approximately 300m in height and 6° latitude wide,

supposing the density of ridge equals 1860 kg/m^3 [1], the mass of ridge should be $5.7 \times 10^{17} \text{ kg}$ for the Iapetus-like case, or $2.1 \times 10^{18} \text{ kg}$ for the longitudinally uniform case.

Discussion: There are two factors to influence the order of upper limit of the ridge. The first is ridge type. For Iapetus-like ridge, the more ridge lies in geological young units like Northern lowland or Tharsis Montes, the greater the limit will be, and the harder we are able to find it. For longitudinally uniform case, the ridge can never be hidden, and the upper limit value is relatively stable for different ridge position. The second is the degree of detrending. If we detrend more thoroughly, there will be less information in data. For a detectable ridge, the critical height is 2~3 times the surrounding fluctuation ($\sim 100\text{m}$), which is determined by the detrending disk radius. In most of our results, the radius is 2.5° . If we halve the disk radius, then the surrounding fluctuation will be $\sim 50\text{m}$, while the upper limit will decrease by a factor of 2. Though there is no strict constrain of the averaged disk size, an appropriate radius should be $1^\circ\sim 10^\circ$. A too big disk is ineffective for detrending, while a disk with radius less than 1° can erase the ridge even for real Iapetus.

In conclusion, the flexibility for our upper limit is no more than 1 order of magnitude. So the corresponding upper limit on moon radius should be no more than $\sim 65\text{km}$, which is 6 times greater than Phobos. Taken in this sense, if a satellite-ring cycle really happened in Martian history, in the manner proposed by [2], there should be a detectable ridge. However, we found nothing in Martian topography detrended with disk radius = $1.25^\circ, 2.5^\circ$. The possible explanations are (i) the disk radius for detection is too small for Mars topography, (ii) the ridge was totally degraded, (iii) the ridge is not longitudinally uniform, and it was covered by lava, (iv) there wasn't such a satellite-ring cycle as we expected.

Reference: [1] Benjamin A. Black, Tushar Mittal. (2015) *Nature Geoscience* 8(12), 913–917. [2] Andrew J. Hesselbrock, David A. Minton. (2017) *Nature Geoscience* 10(4), 266–269. [3] W.-H. Ip (2006) *Geophysical Research Letters* 33(16), L16203. [4] Andrew J. Dombard et al. (2012) *Journal of Geophysical Research* 117(E3), E03002 [5] P.M. Schenk (2010) *AAS-DPS meeting*, abstract 09.16 [6] Tanaka et al. (2014) *Geologic map of Mars: U.S. Geological Survey Scientific Investigations Map 3292*, scale 1:20,000,000, 43 p., <https://dx.doi.org/10.3133/sim3292>. [7] John Pellerier (2008) *Quantitative Modeling of Earth Surface Process* 2, 45. [8] Isamu Matsuyama et al. (2014) *Annual Review of Earth and Planetary Sciences* 42(1), 605-634.

TRIGGERED STAR FORMATION AT THE PERIPHERY OF THE SHELL OF A WOLF-RAYET BUBBLE AS THE ORIGIN OF THE SOLAR SYSTEM V. V Dwarkadas¹, N. Dauphas², B. Meyer³, P. Boyajian¹ and M. Bojazi³, ¹Dept. of Astronomy and Astrophysics, University of Chicago, 5640 S Ellis Ave, ERC 569, Chicago, IL 60637 (vikram@oddjob.uchicago.edu), ²Origins Lab, Department of the Geophysical Sciences and Enrico Fermi Institute, University of Chicago, ³Dept. of Physics and Astronomy, Clemson University, Clemson, SC.

Introduction: A critical constraint on solar system formation is the high $^{26}\text{Al}/^{27}\text{Al}$ abundance ratio of 5×10^{-5} at the time of formation, which was about 17 times higher than the average Galactic ratio [1,2,3,4]. The $^{60}\text{Fe}/^{56}\text{Fe}$ value measured from meteorites is about 2×10^{-8} , at least an order of magnitude lower than the Galactic background [4,5]. The abundance of ^{26}Al as inferred in meteorites is too high [4,6,7] to be accounted for by long-term Galactic chemical evolution [4,8,9] or early solar system particle irradiation [10,11]. This challenges the assumption that a nearby supernova (SN) was responsible for the injection of these short-lived radionuclides into the early solar system [12], unless one can explain why a SN injected only ^{26}Al and not ^{60}Fe .

Sources of ^{26}Al include SNe, AGB stars, and Wolf-Rayet (W-R) stars. The probability of an AGB star being found near the Sun is extremely small [13], and it is unlikely to simultaneously explain the initial solar system abundance of ^{26}Al , ^{60}Fe , ^{107}Pd and ^{182}Hf [14].

Wolf-Rayet Stars: This suggests W-R stars as the ^{26}Al source [5,15,16,17,18,19,20]. These hot stars form the final phase of post-main-sequence massive stars [21]. W-R stars produce ^{26}Al but no ^{60}Fe , so they fit the requirements. Although stellar evolution models differ in the amount of ^{26}Al produced [22,23,24,25,26,27], an analysis of various stellar evolution models suggests that W-R stars with initial mass over about $50 M_{\odot}$ can provide the requisite amount of ^{26}Al to seed the early solar system in most models. The ^{26}Al is mostly produced during the main-sequence stage, but is mainly emitted in the strong mass-loss that follows the main-sequence phase, including the W-R phase (Figure 1).

Massive stars have strong supersonic winds, with wind speeds of order $1000\text{-}2000 \text{ km s}^{-1}$, and mass loss rates of 10^{-7} to $10^{-4.5} M_{\odot} \text{ yr}^{-1}$. These winds sweep up the surrounding medium to form large wind-blown bubbles, having a low density hot interior surrounded by a high-density cool shell [28,29]. The combined action of wind shocks and ionization fronts due to the hot stars can lead to local increases in the density of the shell, leading to collapse of the shell in some places and the formation of new stars [30,31]. This is known as triggered star formation, and is often seen in bubbles around massive stars [32,33,34,35], including W-R stars [36].

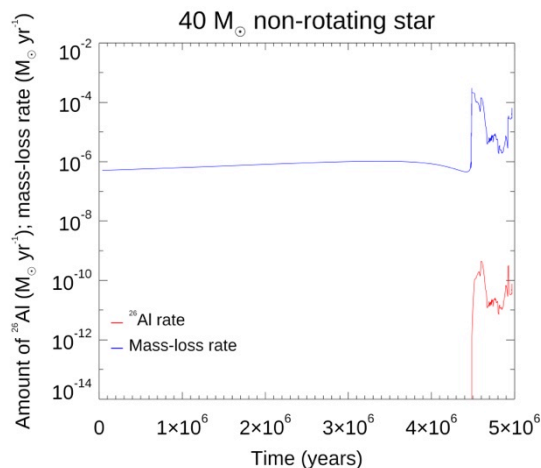


Figure 1: The evolution of the wind mass-loss rate (blue) in a non-rotating $40 M_{\odot}$ star (parameters from [22]). The mass-loss rate is steady throughout the main-sequence phase, but increases dramatically in the red supergiant and W-R phases. In red is the amount of ^{26}Al lost per year via the wind [37]

In our detailed model of the formation of the solar system [37, Figure 2], the collapse of one such shell around a W-R star leads to the formation of the dense cores that give rise to the sun and planetary disk. Aluminium-26 is produced during the evolution of the massive star and released in the wind during the W-R phase. The ^{26}Al subsequently condenses into dust grains that are seen around W-R stars in infrared observations [38,39], and estimated to be about $1 \mu\text{m}$ in size [40]. These large dust grains can survive passage through the reverse shock and the low density shocked wind, reach the dense shell swept-up by the bubble, detach from the decelerated wind with the wind velocity and are then injected into the shell. The dust grains are destroyed in the shell due to ablation and non-thermal sputtering, although a small fraction may survive, while the ^{26}Al is released into the shell. The shell thickness and density varies, as does the velocity of the dust grains, so they will penetrate to different depths in different parts of the shell. Therefore, while some regions may be rich in ^{26}Al , others will not possess significant amounts of ^{26}Al . Such a diversity in ^{26}Al abundance is also seen in meteorites. FUN (with fractionation and unidentified nuclear isotope anomalies)

CAIs [41,42,43] and hibonite rich CAIs are generally ^{26}Al poor [44], whereas spinel hibonite spherules are consistent with the canonical $^{26}\text{Al}/^{27}\text{Al}$ ratio [45].

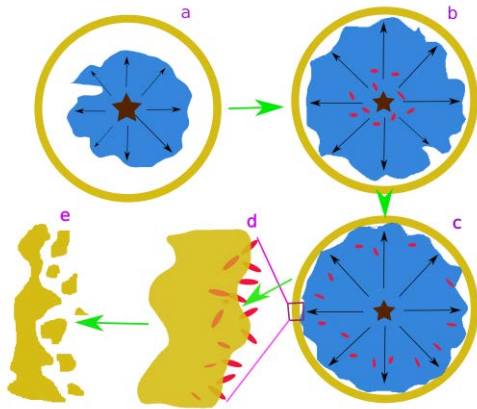


Figure 2: Cartoon version of our model of the formation of the solar system. (a) A massive star forms. Its strong winds and ionizing radiation build a wind-blown bubble. The blue region is wind-blown region; yellow is the dense shell. An ionized region (white) separates them. (b) The bubble grows with time as the star evolves into the W-R phase. At the same time, dust forms in the wind close in to the star, and we assume the ^{26}Al condenses into dust. (c) Dust is carried out by the wind towards the dense shell. (d) The wind is decelerated at the shell, dust detaches from the wind and continues onward, penetrating the dense shell. (e) Triggered star formation is underway. Some material in the shell collapses to form dense molecular cores which will give rise to solar systems. [37]

The final fate of the W-R star is model dependent. In some models the star collapses directly to a black hole [46], with no explosive nucleosynthesis accompanied by production of ^{60}Fe . In other models the star explodes as a SN, but the ejecta distribution is asymmetric [47,48] making it likely that no ejecta will reach the proto-solar system. Even if it does, it is unlikely that the hot, fast ejected material can easily mix with the cooler material in the solar system [49]. Thus it is unlikely that additional ^{60}Fe will be injected into the proto-solar system. The ^{60}Fe present comes from swept-up Galactic material, that could have been cooling for the several million-year stellar lifetime.

We estimate that 1-16% of all stars could have been formed via triggered star formation in bubbles.

References: [1] Lee T. et al (1976), *Geo. Res. Let.*, 3, 109-112. [2] Jacobsen et al. (2008) *EPSL*, 272, 353-

364. [3] McPherson et al. (1995) *Meteoritics*, 30, 365-386. [4] Tang H. and Dauphas N. (2012) *EPSL*, 359, 248. [5] Tang H. and Dauphas N. (2015) *ApJ*, 802, 22. [6] Huss et al. (2009) *Geo. Et Cosmo. Acta.*, 73, 4922-4945. [7] Diehl R et al. (2006), *Nature*, 439, 45-47. [8] Meyer B. and Clayton D. (2000) *From Dust to Terrestrial Planets*, 133-152. Springer. [9] Wasserburg et al. (2006) *Nuc. Phys. A*, 777, 5-69. [10] Marhas K. et al. (2002) *Sci.*, 298, 2182-2185. [11] Duprat J. and Tatischeff V. (2007) *ApJL*, 671, 69-72. [12] Cameron A., and Truran J. (1977) *Icarus*, 30, 447-461. [13] Kastner, J. H., and Myers, P. C. (1994), *ApJ*, 421, 605. [14] Wasserburg, G. J., Karakas, A. I., and Lugaro, M. (2017) *ApJ*, 836,126. [15] Arnould M. et al. (1997), *A&A*, 321, 452-464. [16] Arnould M. et al. (2006), *A&A*, 453, 653-659. [17] Gaidos E. et al. (2009) *ApJ*, 696, 1854. [18] Gounelle M. and Meynet G. (2012) *A&A*, 545, A4. [19] Young, E. D. (2014) *E&PSL*, 392, 16. [20] Young, E. D. (2016) *ApJ*, 826, 129. [21] Crowther, P. A. (2007) *ARA&A*, 45, 177. [22] Ekstrom, S. et al. (2012), *A&A*, 537, A146. [23] Georgy, C., et al. (2012), *A&A*, 542, A29. [24] Georgy, C., et al. (2013), *A&A*, 558, A103. [25] Limongi, M. & Cieffi, A. (2006), *ApJ*, 647, 483. [26] Palacios, A. et al. (2004), *A&A*, 429, 613. [27] Langer, N. et al. (1995), *ApSS*, 224, 275. [28] Dwarkadas, V. V. and Rosenberg, D. (2013) *HEDP*, 9, 226. [29] Toala, J. A., & Arthur, S. J. (2011) *ApJ*, 737, 100. [30] Elmegreen, B., & Lada, C. (1977), *ApJ*, 214, 725. [31] Lefloch, B. & Lazareff, B. (1994), *A&A*, 289, 559. [32] Deharveng, L. et al. (2003), *A&A*, 408, L25. [33] Deharveng, L. et al. (2005), *A&A*, 433, 565. [34] Zavagno, A. et al. (2007), *A&A*, 472, 835 [35] Brand, J. et al. (2011), *A&A*, 527, 62. [36] Liu, T. et al. (2012), *ApJ*, 751, 68. [37] Dwarkadas, V. V., Dauphas, N., Meyer, B., Boyajian, P., and Bojazi, M., (2017), *ApJ*, 851, 147 [38] Rajagopal, J, et al. (2007), *ApJ*, 671, 2017. [39] Marchenko, S. & Moffat, T. (2007), *ASPC*, 367, 213. [40] Marchenko, S. et al. (2002), *ApJ*, 565, L59. [41] Esat, T. M., Papanastassiou, D. A., and Wasserburg, G. J. (1979), in LPSC Conf Vol 10, 361-363. [42] Armstrong, J. T., Hutcheon, I. D., and Wasserburg, G. J. 1984, in LPSC Conference, Vol. 15, 15. [43] MacPherson, G. J., Bullock, E. S., Janney, P. E., et al. 2007, in LPSC Conf, Vol. 38, 1378. [44] Koop, L., Davis, A. M., Nakashima, D., et al. 2016, *GeoCoA*, 189, 70. [45] Liu, M.-C., McKeegan, K. D., Goswami, J. N., et al. 2009, *GeoCoA*, 73, 5051. [46] Sukhbold, T., & Woosley, S. E. 2016, *ApJL*, 820, L38. [47] Maeda, K., Kawabata, K., et al. (2008), *Science*, 319, 1220. [48] Mazzali, P. A., Kawabata, K. S., Maeda, K., et al. (2005), *Science*, 308, 1284. [49] Goswami, J. N., and Vanhala, H. A. T. 2000, *Protostars and Planets IV*, 963

IMPLICATIONS OF HADEAN MINERALOGICAL DIVERSITY FOR ORIGIN OF LIFE STUDIES. E. A. Bell¹, D. Trail^{1,2}, T. M. Harrison¹, and P. Boehnke^{3,4}; ¹Department of Earth, Planetary & Space Sciences, UCLA, Los Angeles, CA 90095, ²Department of Earth & Environmental Sciences, University of Rochester, Rochester, NY 14627, ³Department of the Geophysical Sciences, University of Chicago, Chicago, IL 60637, ⁴Chicago Center for Cosmochemistry, Chicago, IL

Introduction: Because the Hadean eon (pre-4.03 Ga) is defined by the absence of a terrestrial rock record, acquiring knowledge of what minerals then existed must necessarily be by implication. Neither of the two approaches thus far utilized – thought experiment [1] and documenting primary inclusions in Hadean detrital zircons [2] – is likely to provide a complete inventory, but the former has the potential for serious misdirection.

The presence or absence of key mineral phases during the Hadean has significant implications to the plausibility of certain pathways to life. For example, the RNA World hypothesis posits an evolutionary stage in which self-replicating RNA molecules arose before the emergence of DNA and proteins [3]. Each nucleotide in RNA contains a ribose sugar with attached bases (ACGU) and two phosphate groups. Thus a postulated paucity of terrestrial phosphate minerals on early Earth as a source of reactive phosphorous [4] could have forestalled biopoiesis. The observation of leachable apatite inclusions in Hadean Jack Hills zircons [5] suggests otherwise. Although ribose is unstable in many environments, aqueous solutions containing high borate concentrations stabilize that molecule [6,7,8]. Several authors have argued that borate minerals didn't exist in sufficient quantities when the prebiotic synthesis processes that led to RNA occurred [1,9]. However, laboratory partition experiments coupled with B contents of >4 Ga zircons [10] suggest that Hadean crustal B concentrations were similar to modern Earth.

Hadean mineral speculations: Hazen [1] concluded that Hadean Earth supported fewer than 10% of the ~4800 known mineral species and that the “relative Hadean mineralogical parsimony is a consequence of the limited modes of mineral paragenesis prior to 4 Ga”. Four criteria were enumerated that eliminated minerals from consideration as significant Hadean phases. These assumptions are: (1) rare minerals today were never widely distributed or volumetrically significant, (2) minerals arising primarily at convergent boundaries didn't exist because plate tectonics had not yet initiated, (3) biologically-mediated minerals were absent because all life is post-Hadean, and (4) redox-sensitive minerals requiring a high f_{O_2} didn't predate the Great Oxidation Event. We note that i) since only one quarter of known minerals are documented from >25 localities [1], criterion (1) is also true for all but ~15% of the presently known mineral species, ii) while

there is absolutely no evidence that plate tectonics was not operating on Earth during Hadean times, there is evidence that it may have been [11], and iii) while there is absolutely no evidence that life did not arise during the Hadean, there is some evidence that it might have [12,13]. While redox-sensitive minerals requiring an f_{O_2} higher than the hematite-magnetite buffer were likely rare on Hadean Earth, local conditions might have supported them in microenvironments [e.g., 13].

Observed Hadean minerals: We have thus far identified fourteen minerals as primary inclusions in Hadean Jack Hills zircons [2]. They are: quartz, plagioclase, alkali feldspar, muscovite, biotite, hornblende, sphene, apatite, monazite, ilmenite, rutile, Fe-oxides, Al_2SiO_5 , and graphite [2]. About two-thirds of all documented primary inclusions are quartz and muscovite and thus there appears little question that I- and S-type granitoids coexisted during the Hadean and that the quartz-deficient TTGs were not a significant source [cf. 1].

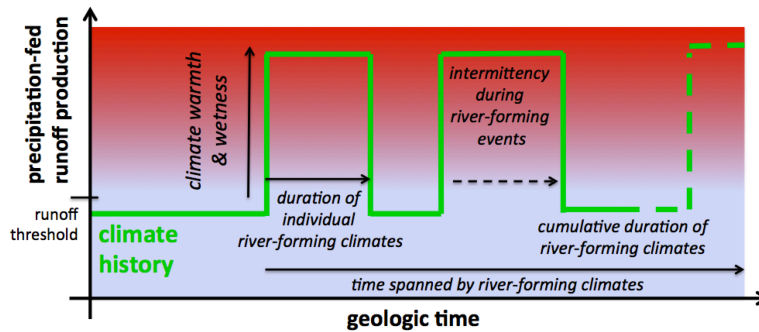
As a comparator, we surveyed a large number of zircons from Phanerozoic I-, S-, and A-type granitoids and found them to host thirty-one distinct mineral inclusions (i.e., a 0.65% occurrence rate relative to the known total), ranging from the expected granitic species (e.g., quartz, feldspars, micas) to the surprising (e.g., NaCl, Cu). However, as any one locality contains only three to nineteen included mineral species (10 ± 4), the Jack Hills suite could be viewed as reflecting similar mineralogic diversity as today. If a similar scaling relationship exists between these two populations and their respective global mineralogic domains, even comparing overall mineral occurrence rates (i.e., 32:15) would imply that a minimum of 2,000 (i.e., $15/0.0065$) minerals were present during the Hadean. But many of the ~4,800 known minerals form by fluid interactions in the upper few km of crust, a zone almost exclusive of zircon formation. Thus not finding zeolites, sulfates, borates or other such inclusions in Hadean zircons is not evidence they didn't then exist, but rather that they either haven't yet been observed or were not amenable to capture.

Summary: Geochemistry provides no significant limitation on the type or abundance of minerals that may have been present on Hadean Earth. Speculations in the literature that claim to impose such restrictions risk inhibiting thought regarding possible scenarios for the emergence of life on Earth.

References:

- [1] Hazen, R. M. (2013) *Am. Jour. Sci.*, 313, 807-843. [2] Bell E. A. et al. (2015) *Lithos* 234, 15-26. [3] Neveu, M. et al. (2013) *Astrobiology*, 13, 391-403. [4] Griffith, E. J. et al. (1977) *Orig. Life*, 8, 71-85. [5] Bell E.A. et al. (2018) *Chem. Geol.* 10.1016/j.chemgeo.2017.12.024 . [6] Benner, S.A., et al. (2012) *Acc. Chem Res.*, 45, 2025-2034. [7] Ricardo, A. et al. (2004) *Science* 303, 196. [8] Kim, H.J., et al., 2011. *Journ. Am. Chem. Soc.*, 133, 9457-94,68. [9] Grew, E. S. et al. (2011) *Origins of Life and Evolution of Biosphere*, 41, 307-316. [10] Trail D. et al. (2017) *Before Life: The chemical, geological and dynamical setting for the emergence of an RNA World*. Boulder, CO Workshop, Oct. 9-12, 29-30. [11] Hopkins M. et al. (2008) *Nature*, 456, 493-496. [12] Battistuzzi et al. (2004) *BMC Evol. Biol.*, 4, 44-51. [13] Bell E.A. et al. (2015) *Proc. Nat. Acad. Sci.*, 112, 14518-14521.

KEY PARAMETERS FOR EARLY MARS CLIMATE RESEARCH. Edwin S. Kite, University of Chicago (kite@uchicago.edu)



Introduction: In the last few years, published explanations for rivers and lakes on early Mars have ranged from intermittent $<10^2$ -yr-duration volcano/impact-triggered transients to $>10^6$ -yr-duration humid greenhouse climates. As a set, these models represent an embarrassment of riches for the Mars research community, so geologic data are sorely needed to discriminate between the models. Fortunately, new analyses provide better constraints on the number, duration, intermittency, and intensity of the river-forming climates. However, as shown at the October 2017 Early Mars Conference, these geologic constraints have not been summarized in a way that is digestible for the modeling community. Here I focus on physical parameters that can be used as input or test data for numerical models of post-Mid-Noachian climate and atmospheric evolution.

Number of river-forming climates: ≥ 2 (high confidence). For this abstract, I define a river-forming climate as a >10 yr time interval during which precipitation-sourced water runoff occurred during most years. Valley networks formed in the Late Noachian / Early Hesperian (LN/EH) [1]. Then, after an interval of deep wind erosion indicating dry conditions [2,3], alluvial fans and closed-basin lakes formed in the Late Hesperian and/or Amazonian (LH/A) [4,5]. [3] and [6,7] suggest division of the LH/A climate into 2 or 3 river-forming events. The LN/EH valleys represent an intense, but relatively late and topographically superficial [8] geomorphic event. Pre-LN landscape modification has been interpreted to be fluvial [9].

Final drying-out of the rivers of Mars <3.5 Ga (high confidence). Crater counts indicate rivers at 3.0 Ga [4,10]; (2 Ga on the Robbins chronology [11]). This is consistent with crosscutting relationships [5] and with a K-Ar date at Gale [12]. Because melting snow and ice should be difficult for $P < 0.1$ bar [13], these late dates set us the challenge of finding a sink for CO_2 that could be efficient relatively late in Mars history [14].

Duration of longest river-forming climate: >3 kyr (high confidence), $>10^5$ yr (medium confidence). Hydrological analysis using orbiter topography, indicate individual lakes lasted >3 kyr (assuming dilute flow

$<1\%$) [15-16]. The Murray mudstone in Gale Crater is water-altered and rhythmically laminated, with mud-cracks only near the top of the logged section, and is interpreted as a lake deposit. If mm-thick laminae are interpreted as annual lake varves, then the absence of evidence for drying-up lower in the section suggests lake lifetime $>10^5$ yr [17]. Orbiter data indicate river-forming deposits built up over $>10^6$ yr [18] but hiatuses cannot be excluded. These durations, as well as column runoff production >1 km (medium confidence) [19], mean that runoff could not be directly produced by impact energy [20-21].

Peak runoff production >0.1 mm/yr (high confidence). Hydrologic calculations and width-discharge correlations indicate runoff production > 0.1 mm/yr [19,22,23]. These rates can be explained by either snowmelt or rainfall (but see the new global database of Kite et al., this conf.).

Intermittency during wet events: peak runoff production $<10\%$ of the time (high confidence). Many, but not most, lakes during the LN/EH overflowed. Almost no lakes overflowed during the LH/A [24]. To avoid all lakes overflowing, given high peak runoff production and long lake duration, runoff production must have been unsteady during the wet events [25]. Extremely slow average alluvial fan build-up rate during the LH/A wet event [7] further suggests unsteady runoff. Fluvial intermittency need not require intermittent habitability. Life persists in climates too dry for rivers [26].

Paleo-atmospheric pressure, P : <1 bar (medium confidence), >0.012 bar (high confidence). The modern atmosphere+ice CO_2 reservoir is 0.012 bar [27]. Small craters interbedded with river deposits indicate thin atmosphere $\sim(3.6-3.8)$ Ga; <1 bar according to the bolide burn-up/break-up model of [28]. However, this might correspond to periods of atmospheric collapse interspersed with river-forming climates. $P \sim 0.01$ bar suggested by ~ 3.6 Ga bedforms [29] might also record atmospheric collapse. Meteorite noble gas data have been interpreted to require $P > 0.5$ bar at 4 Ga, but also $P < 0.4$ bar at ~ 4 Ga [30-31]. There is little direct geological evidence for instantaneous $P > 0.012$ bar, as opposed to cumulative loss/outgassing of >0.012 bar. Gently landing the Little-

ton meteorite requires $P > (0.012 - 0.044)$ bars [32]. [33] suggests $P > 0.12$ bar ~ 3 Ga to gently land 1 volcanic bomb sag. The lower bound on the modern C escape-to-space flux is ~ 0.01 (bars CO_2)/Gyr, or even lower [34].

Years of sediment deposition recorded by sedimentary rocks: $>10^8$ yr (very high confidence). Sedimentary rocks require less water to form than rivers, but rhythmically-layered sedimentary rocks probably require some liquid water ([35], but see also [36]). Tying of rhythmic bedding to orbital frequencies allows sediment deposition duration to be calculated [37-38]. Counts of craters at one of the many unconformities within sedimentary sequences also yield durations $>10^8$ yr [6], so the total time spanned by sedimentary-rock build-up was $\gg 10^8$ yr.

Duration of surface liquid water at an “average” place on Mars: $<10^7$ yr (medium/high confidence). The persistence of minerals that dissolve readily in water show that post-Mid-Noachian aqueous alteration on Mars could not have been both global and long-lasting [39-42].

Maximum ocean size: $>1.1 \times 10^6$ km² (high confidence). Geomorphological evidence indicates a sea in Eridania [43]. Explaining the Eridania sea is even more challenging than explaining the (disputed, putative) Oceanus Borealis, because Oceanus Borealis (but not an Eridania-sized sea) is somewhat self-sustaining in climate models.

Peak warmth: $>270\text{K}$ (very high confidence), $>298\text{K}$ (medium confidence). The aqueous deposits of Mars required liquid water to form. Salinity is unlikely to permit much lower temperatures; for example, Mg-sulfate deposits are common, and the $\text{MgSO}_4\text{-H}_2\text{O}$ eutectic is 270K . Meteorite evidence for $>298\text{K}$ is compelling [44], but might correspond to lake-waters warmed by a solid-state greenhouse effect beneath ice cover.

Peak mean annual temperature: $>250\text{K}$ (high confidence). Thicker atmospheres that are suspected to be required for rivers and lakes on Mars damp out diurnal temperature oscillations. The lack of evidence for icy conditions along the MSL traverse hints at ice-free lakes [45]. Groundwater circulation occurred, but might be sustained through permafrost by advection, or in steady state beneath taliks.

Duration of valley-network-forming climate episode: $>10^5$ yr (medium confidence). Sediment transport calculations indicate $>10^5$ yr are needed to form the valley networks [46]. If the Mars valley networks were cut into weakly-indurated sediment, then shorter formation durations are possible [47], but in-place Mars rock strength is similar to adobe bricks or weak concrete on Earth, *not* a loose sand-pile (high confidence) [48]. When modern estimates of systematic error for counts are folded in, published THEMIS crater counts [1] are consistent with all VNs forming in a short time. Future work might seek craters interbedded during the VNs.

Surface-formed phyllosilicates – the key to early Mars climate? With some exceptions, the above-summarized data are consistent with a fairly cold (snow/ice-melt) climate [49,50]. In contrast, the simplest interpretation of the clay profiles (e.g. Mawrth) is $>10^{(4-5)}$ yr of clement ($\sim 300\text{K}$) climate [51]. One possibility is that Mawrth is a window into a climate that predates the VNs. Alternatively, pedogenic clays could be formed by cold, acidic waters [52].

Wrap-up: In the early 2000s, geomorphic data were used to argue for a wet early Mars; mineralogical data were more ambiguous. In 2018, these roles have perhaps reversed - the orbiter-geomorphic lower limits summarized above may be less constraining than the phyllosilicate evidence! MSL traverse data have been reported by the MSL sedimentology team as supporting warmer/wetter climates than are required by the orbiter-geomorphic lower limits. At the conference, I will graphically summarize available constraints, and discuss how climate models – such as the recently proposed Limit Cycle idea [53] – hold up when confronted with these constraints.

References. (Many great papers are omitted from this abstract due to space limits.) [1] Fassett & Head 2008, *Icarus* v.195 [2] Palucis et al., 2016, *JGR* [3] Irwin et al. 2004, *JGR* v.109(E9) [4] Grant & Wilson 2011, *GRL* [5] Wilson et al., 2016, *JGR* [6] Kite et al. 2015, *Icarus* [7] Kite et al. 2017, *GRL* [8] Luo et al. 2017, *Nature Comm.* [9] Irwin et al. 2013, *JGR* [10] Dickson et al. 2009, *GRL* [11] Robbins 2014, *EPSL* [12] Martin et al. 2017, *JGR* [13] Hecht 2002, *Icarus* [14] M. Mansfield et al., in review *JGR* [15] Irwin et al. 2015, *Geomorphology* [16] Williams & Weitz 2014, *Icarus* [17] Hurowitz et al. 2017, *Science* [18] Kite et al. 2013, *Icarus* [19] Dietrich et al., in Tsutsumi & Laronne, *Gravel Bed Rivers* 2017 [20] Turbet et al 2017, 4th Conf. on Early Mars [21] Steakley et al. 2017, 4th Conf. on Early Mars. [22] Palucis et al. 2014, *JGR Geology* [23] Irwin et al. *Geology* 2005 [24] Goudge et al. 2016, [25] Barnhart et al. 2009, *JGR* [26] Amundson et al. 2012, *GSA Bull.* [27] Bierson et al. 2016 *GRL* [28] Kite et al. 2014, *Nature Geosci.* [29] Lapôtre et al. 2016, *Science* [30] Cassata et al. 2012, *Icarus* [31] Kurokawa et al. 2018, *Icarus* [32] Chappelow et al. 2016, *LPSC* [33] Manga et al. 2012, *GRL* [34] Lundin et al. 2013, *GRL* [35] McLennan et al. 2005, *EPSL* [36] Niles et al. 2017, *Nat. Comm.* [37] Lewis et al. 2008, *Science* [38] Lewis & Aharonson 2014, *JGR* [39] Stopar et al. *GCA* 2006 [40] Tosca & Knoll *EPSL* 2009 [41] Elwood Madden et al. 2009, *Geology* [42] Ruff & Hamilton 2017, *Am. Mineral* [43] Irwin et al. 2002, *Science* [44] Halevy et al. 2011, *PNAS* [45] Grotzinger et al., *Science* 2015 [46] Hoke et al. 2011, *EPSL* [47] Rosenberg & Head 2015, *P&SS* [48] G.H. Peters et al. 2017, *GRL* [49] Wordsworth et al. 2016, *AREPS* [50] Head 2017, 6th Conf. on Mars Atmosphere [51] Bishop & Rampe 2016, *Icarus* [52] Louizeau et al 2018, *Icarus*. [53] Batalha et al. 2016 *EPSL*.

EVAPORATION OF SPINEL-RICH CAI MELTS: A POSSIBLE LINK TO CH-CB CAIs. M. A. Ivanova^{1,2}, R. A. Mendybaev³, S. I. Shornikov¹, K. M. Ryazantsev¹, and G. J. MacPherson². ¹Vernadsky Institute, Kosygin St. 19, Moscow 119991 (meteorite2000@mail.ru); ²Department of Mineral Sciences, National Museum of Natural History, Smithsonian Institution, Washington, DC 20560; ³University of Chicago, Chicago, IL 60637.

Introduction: The most important processes in formation of calcium-aluminum inclusions (CAIs) were condensation, melting and evaporation. The bulk compositions of CAIs record the cumulative effects of these high-temperature and largely volatility-controlled processes during the first several million years of solar system history [1]. We recently presented results on thermodynamic modeling of evaporation of CAIs with different compositions from CV3 chondrites, and compared their evaporation trends with the bulk compositions of CAIs from CV3 and CH-CB chondrites [2]. The calculations showed that unlike for most other CAI composition melts, evaporation of a melt with a spinel-rich and calcium-poor CAI composition (*5aN*) starts with faster evaporation of Si over Mg, resulting in a compositional trend that well fits the CAI compositions of CH-CB chondrites [2]. Unlike most CAIs from CV chondrites, *5aN* is a pristine fine-grained spinel-rich inclusion with no traces of melting or evaporation. Its Al₂O₃-enriched bulk composition has a non-solar CaO/Al₂O₃ ratio of ~0.3. The bulk chemical composition of *5aN* is plotted in the anorthite field of spinel-rich CAIs on a Ca₂SiO₄-Al₂O₃-Mg₂SiO₄ diagram [2].

Here we report experimental results on the evaporation of a CAI *5aN*-like composition and compare them with thermodynamic calculations. The results are used to investigate the evolution of the bulk chemical composition of *5aN* during evaporation and to check if *5aN*-like CAIs could serve as precursors of CAIs in CH-CB chondrites.

Experimental and analytical methods: As a starting material in the experiments we used a CAI *5aN*-like composition prepared by mixing MgO, SiO₂, Al₂O₃ and CaCO₃ with CaO/Al₂O₃ ratio of ~0.3. The composition was evaporated in a vacuum furnace at 1900°C for 0 to 45 minutes (Table 1) at total pressure ~10⁻⁶ torr using experimental procedures per [4, 5]. One run (“*5aN*-3”) was quenched as soon as the furnace temperature have reached 1900°C; its analyzed composition is taken as the starting composition in all our experiments. Texture and chemical composition of the evaporation residues were studied at the University of Chicago using TESCAN LYRA3 FIB/FESEM equipped with an Oxford AZtec x-ray microanalysis system, and at the Smithsonian Institution using a FEI NOVA NanoSEM 600 SEM (EDS) and JEOL 8530F Hyperprobe (WDS). Mineral chemistry of evaporated

residues was also performed by JEOL 8530F Hyperprobe.

Results: The typical textures of the *5aN* experimental residues are shown in Fig.1. Most of the run products (Fig. 1a) consist of intergrowths of quench textured “Christmas tree”-like spinel and glass. The most evaporated samples *5aN*-1 and *5aN*-7 which lost all its MgO and SiO₂ (Table 1) are composed mostly of hibonite and CaAl₂O₄ with a minor amount of CaAl₄O₇ (Fig. 1b). It is interesting to note that as evaporation proceeds spinel gradually becomes more saturated in Al₂O₃ compared to the stoichiometric one.

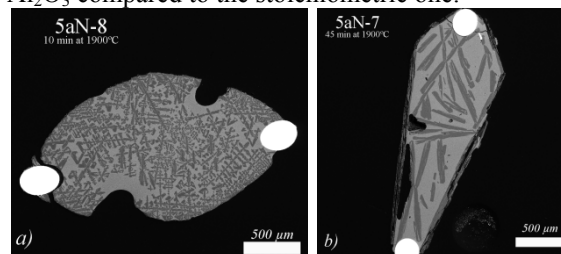


Fig. 1. Backscattered electron images of the experimental residues: a) typical texture with “Christmas tree”-like spinel (dark) and glass (light); b) texture of most evaporated residues with hibonite (dark) and CaAl₂O₄ (light).

Table 1. Bulk compositions of evaporated samples

sample	time, min	MgO, wt%	Al ₂ O ₃ , wt%	SiO ₂ , wt%	CaO, wt%	CaO / Al ₂ O ₃	% Mg lost	% Si lost
<i>5aN</i> -3	0	16.02	37.72	33.71	12.56	0.33	0.0	0.0
<i>5aN</i> -6	5	15.77	43.07	27.17	14.00	0.33	13.8	29.4
<i>5aN</i> -8	10	14.46	46.07	23.91	15.56	0.34	26.1	41.9
<i>5aN</i> -5	15	12.69	50.59	19.87	16.85	0.33	41.0	56.0
<i>5aN</i> -2	15	11.43	57.63	13.95	16.99	0.29	53.3	72.9
<i>5aN</i> -4	25	6.49	63.62	9.11	20.79	0.33	76.0	84.0
<i>5aN</i> -1	30	0.01	76.88	0.09	23.02	0.30	100.0	99.9
<i>5aN</i> -7	45	0.00	76.66	0.05	23.29	0.30	100.0	99.9

% Mg and % Si lost have been calculated relative to *5aN*-3 (0 min run) chemical compositions of which has been considered as a starting composition of the samples before evaporation at 1900 °C

Bulk compositions of experimental run products of *5aN* are presented in Table 1 and plotted on a Ca₂SiO₄-Al₂O₃-Mg₂SiO₄ diagram (Fig. 2). The diagram also shows the calculated evaporation trajectory of CAI *5aN* as well as available experimental evaporation trajectories of *CAIB* [5] and *CAI4* [6] melts with bulk compositions somewhat close to that of *5aN*.

As refractory Ca and Al do not evaporate under conditions of the experiments (CaO/Al₂O₃ ratio in evaporation residues would remain constant until all Si and Mg are lost), the weight loss of samples is caused by evaporation of Mg and Si. Fig. 3 shows the experimental evaporation trajectories for *5aN* along with

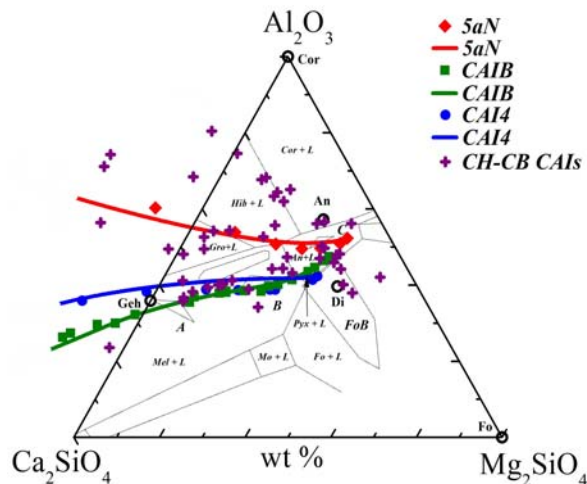


Fig. 2. Experimental (lines) and calculated (symbols) compositional trends of CAIs material: *5aN*, *CAI4* and *CAIB* evaporation compare to CH-CB CAIs bulk compositions.

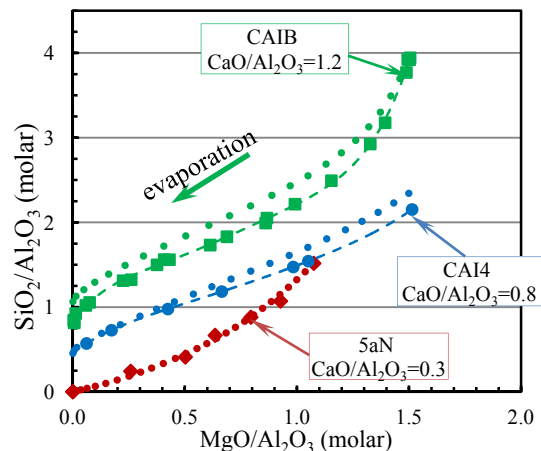


Fig. 3. Experimental trajectories for *5aN*, *CAIB* [5] and *CAI4* [6] melts evaporated at 1900 °C in vacuum. Dots are thermodynamic calculations; dashed lines are best fits to the experimental data. Starting composition of *CAI4* used in the calculations contained 1 wt% more SiO_2 , and 0.5 wt% less Al_2O_3 than the composition used in the experiments.

those for *CAIB* [5] and *CAI4* [6], and the thermodynamically calculated trajectory for *5aN* melt. First, note good agreement between calculated and experimentally determined trends. Second, evaporation of *5aN* starts with much faster loss of Si compared to Mg, which is similar to the initial *CAIB* trend. This might be due to the fact that the initial chemical compositions of both *5aN* and *CAIB* melts are plotted in anorthite stability field in Fig. 2. As evaporation proceeds, the rates of Si and Mg loss become comparable, and in highly processed *5aN* melt Mg evaporates faster than Si and the trend shifts toward Ca-aluminates. In case of evaporation of more SiO_2 -rich and MgO-poor *CAIB*

melt with $\text{CaO}/\text{Al}_2\text{O}_3=1.2$, the residual melt evolves toward gehlenite-rich melilite.

Unlike our *5aN* and *CAIB* melts, an initial faster loss of Mg compared to Si was observed when MgO-rich forsteritic melts were evaporated in vacuum [4, 7] and in thermodynamically calculated trends for several CAIs from CV chondrites [2, 3, 9]. Note also the different evaporation trajectories of *5aN* and *CAI4* melts with the same $\text{MgO}/\text{Al}_2\text{O}_3$ and $\text{SiO}_2/\text{Al}_2\text{O}_3$ ratios (~ 1.1 and ~ 1.5 correspondingly, where *5aN* and *CAI4* curves intersect in Fig. 3), yet different $\text{CaO}/\text{Al}_2\text{O}_3$. Taken together, these differences in evaporation trajectories are most likely due to the difference in starting melt compositions. This suggests that melt structure plays an important role during the evaporation process.

Discussion. As shown on Fig. 2, the compositional trends of evaporated *5aN*, *CAIB* and *CAI4* melts obtained in experiments and by theoretical model calculations are very similar. The experiments confirm our thermodynamic calculations based on the theory of associated solutions and on experimental data for activities of oxides in the system $\text{CaO-MgO-FeO-Al}_2\text{O}_3\text{-TiO}_2\text{-SiO}_2$ [3,8]. Both experiments and calculations show that evaporation of CAI *5aN*-like melt results in a compositional trend that well fits the CAI compositions of CH-CB chondrites [2] (Fig. 2). The reason why the evaporative trend of *5aN*-like melt is different from those with other compositions studied (like *CAIB* or *CAI4*) is not clear: it might be due to the melt composition being in the anorthite stability field with high concentrations of Al_2O_3 ; or is caused by acidity-basicity factors of the melts [10].

Our results showed that spinel-rich melts can be possible precursors for very refractory population of CAIs from CH-CB chondrites. If so, they should show fractionated isotopic effects in Mg and O, but CAIs from CH-CBs didn't record such the effect [11]. Lack of isotopic signatures can be explained by melting of the precursors under relatively high-pressure conditions. Further isotopic investigations may help to resolve this problem.

References: [1] MacPherson G. J. (2014) Treatise on Geochemistry (second edition), 1 (Ed. A. M. Davis) 139–179. [2] Ivanova M. A. et al. (2017) *LPS XLVIII*, Abs. #1363. [3] Shornikov S. I. et al. (2017) *LPS XLVIII*, Abs. #1964. [4] Mendybaev R. A. et al. (2013) *GCA*, 123, 368–384. [5] Richter F. M. et al. (2007) *GCA*, 71, 5544–5564. [6] Mendybaev R. A. and Richter F. M. (2016) *LPS XLVII*, Abs. #2929. [7] Mendybaev et al. (2014) *LPS XLV*, Abs. #2782. [8] Shornikov S. I. et al. (2015) *International Conf. XVI, Physico-chemistry and Petrology in the Earth Sciences*, 281–284. [9] Ivanova M. A. et al. (2016) *LPS XLVII*, Abs. #2315. [10] Yakovlev O. I. et al. (2017) *Geochem. Int.* 55, 3, 251–256. [11] Krot A. N. et al. (2009) *GCA* 73, 4963–4997.

NEW CONSTRAINTS ON THE MAJOR NEUTRON SOURCE FOR *s*-PROCESS NUCLEOSYNTHESIS IN AGB STARS. N. Liu^{1,2}, R. Gallino³, A. M. Davis⁴, R. Trappitsch^{4,5}, T. Stephan⁴, P. Boehnke⁴, L. R. Nittler², C. M. O'D. Alexander², and M. Pellin^{4,6}, ¹Department of Physics, Washington University in St. Louis, St. Louis, MO 63130, USA, nliu@physics.wustl.edu, ²Department of Terrestrial Magnetism, Carnegie Institution for Science, Washington, DC 20015, USA, ³Dipartimento di Fisica, Università di Torino, Torino 10125, Italy, ⁴The University of Chicago, Chicago, IL 60637, USA, ⁵Lawrence Livermore National Laboratory, CA 94550, USA, ⁶Argonne National Laboratory, Argonne, IL 60439, USA.

Introduction: Asymptotic Giant Branch (AGB) stars are the stellar site for the main *s*-process (slow neutron capture process), with ^{13}C being the major neutron source via $^{13}\text{C}(\alpha, n)^{16}\text{O}$ [1]. Formation of ^{13}C via $^{12}\text{C}(p, \gamma)^{13}\text{N}(\beta^+ \nu)^{13}\text{C}$ within the so-called “ ^{13}C -pocket” requires mixing protons from the convective H envelope into the radiative He intershell, a locally unstable thermodynamic state that is extremely difficult to treat in stellar models, because many physical mechanisms may compete in the pocket formation.

Presolar grains are ancient stellar relicts, and a majority of presolar SiC grains, the mainstream (MS) grains, came from low-mass AGB stars with *s*-process isotopic signatures. The rare Y and Z grains also originated in AGB stars, but of lower metallicity. In our previous investigation of ^{13}C -pocket uncertainties, we obtained correlated Sr and Ba isotope ratios in single SiC grains, and the data consistently point to the existence of large ^{13}C -pockets in AGB stars [2,3,4]. However, a recent study [5] showed that these ^{13}C -pocket characteristics failed to match Ni isotopic data from MS grains. The reason for this disagreement is unclear, but may be partially because the Torino AGB stellar model adopted in [5] had several improvements compared to the one used in [4]. Here, we investigate this problem by comparing the literature MS grain isotope data on Sr, Ba, and Ni to the updated Torino AGB models with the main aim of testing the recently proposed large ^{13}C -pocket produced by magnetohydrodynamic simulations in [6] (hereafter T17 pocket). We also report new Sr, Mo, and Ba isotope data for a large number of Y and Z grains to investigate the characteristics of ^{13}C -pockets in AGB stars with varying metallicities.

Experiments & Models: Detailed descriptions of Torino AGB models can be found in [2–5]. In this study, we adopted the simulated T17 pocket in our post-processing *s*-process calculations and also varied the ^{13}C concentration in the pocket to search for the best match to the presolar grain data (Fig. 1). Note that the T17 ^{13}C -pocket has a quite flat ^{13}C profile within the pocket and is, therefore, similar to the largest-sized ^{13}C -pocket (hereafter L15 pocket) discussed by [4, Fig. 9h]. To better understand the ^{13}C -pockets in lower-metallicity AGB stars, we also analyzed 42 sub- μm - to μm -sized Y and Z grains for their Sr, Mo, and Ba isotopic compositions with CHILI [8]; 15 MS grains were also measured during the same session (Fig. 2). These grains had been

measured with a NanoSIMS 50L instrument at Carnegie for their C, N, and Si isotope ratios prior to the CHILI analysis. We obtained Mo isotope ratios in all 42 grains; Sr and Ba isotope ratios were obtained in only about one-third of the grains, indicating lower efficiencies of the Sr and Ba resonance ionization schemes and/or lower Sr and Ba concentrations in the grains.

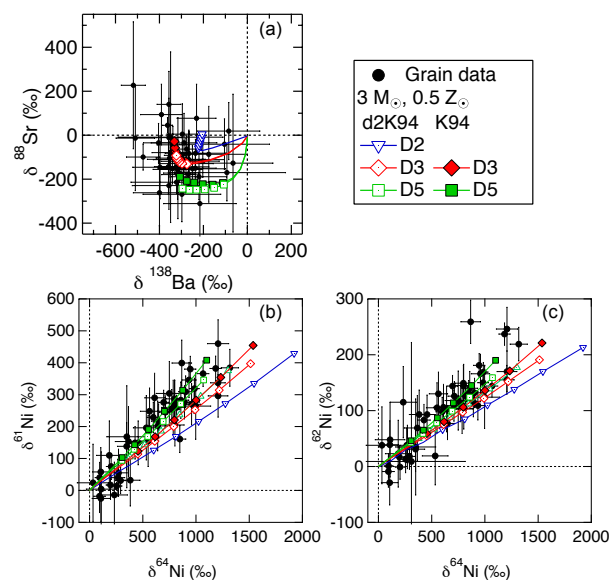


Fig. 1. Comparison of MS grain data [2–5] to Torino AGB model calculations for a $3 M_{\odot}$, $0.5 Z_{\odot}$ AGB star by adopting the T17 ^{13}C -pocket. Each model prediction evolves from zero (initial stellar composition) along colored lines, with symbols plotted on top of the lines when $\text{C}/\text{O} > 1$ in the envelope. K94 refers to the $^{22}\text{Ne}(\alpha, n)^{25}\text{Ne}$ rate recommended by [7] and d2K94 represents the K94 rate reduced by a factor of two. The cases of D2, D3, D5 refer to the ^{13}C concentration (original case) in the T17 pocket divided by a factor of two, three, and five.

MS Grain Constraint: Figure 1a shows that the new AGB stellar model requires a ^{13}C -pocket larger than previously constrained for matching the grain data. Based on the old stellar model, [4] showed that with increasing pocket size, the model predictions for $\delta^{88}\text{Sr}$ continue to increase, and the best match to the grain data is reached by model predictions with a ^{13}C -pocket size four times smaller than that of the L15 pocket (hereafter L15_d4 pocket) during the C-rich phase, whilst model predictions with the L15 pocket yield the

poorest match to the data due to the rapidly growing $\delta^{88}\text{Sr}$ values with increasing thermal pulses (TPs). In contrast, the new calculations (Fig. 1a) show that the T17 pocket, similar to the L15 pocket, can explain the Sr-Ba isotope data. The significant reduction in the predictions for $\delta^{88}\text{Sr}$ mainly results from the incorporation of C-enhanced molecular opacities in the new stellar model, which induces lower stellar temperatures and enhanced mass loss rates. This results in less efficient operation of the $^{22}\text{Ne}(\alpha, n)^{25}\text{Mg}$ source and consequently reduced ^{86}Sr depletion in AGB stars, because the ^{86}Sr nuclei produced in the ^{13}C -pocket are partially destroyed during the peak neutron density induced by the marginal activation of the $^{22}\text{Ne}(\alpha, n)^{25}\text{Mg}$ reaction at the bottom of the He-burning zone during a TP. This effect can be observed in Fig. 1a by comparing d2K94 with K94 calculation results. Also, this explains the better match given by model predictions for a $3 M_{\odot}$ AGB star with respect to those for a $2 M_{\odot}$ AGB star (adopted in previous studies) because of its increased stellar temperature.

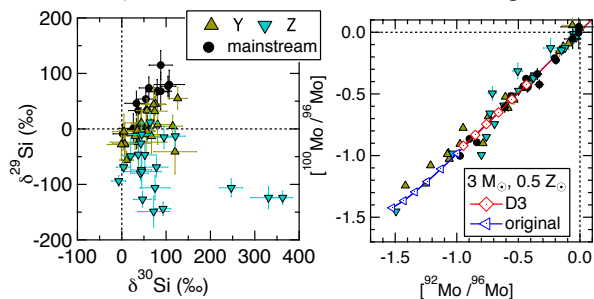


Fig. 2. Three-isotope plots of grain data from this study. The Mo isotope ratios are shown as the \log_{10} of the solar system normalized isotope ratios instead of δ notations. Errors are 2σ . The original case refers to the ^{13}C concentration in the T17 pocket given in [6].

The Sr-Ba isotope data constrains the ^{13}C concentration to lie between the D5 and D2 cases in the T17 pocket, which also provide reasonable matches to the Ni isotope data in Figs. 1(b) & (c). In contrast, by adopting a smaller ^{13}C -pocket (four times smaller than the T17 pocket) in the new Torino AGB models, the D6 case best reproduces the slopes in the three Ni isotope plots (Fig. 11 in [5]), while the D2 case provides the best match to the grain concentrated region in the Sr-Ba isotope plot (not shown). Thus, we can conclude that the discrepancy between the constraints from the correlated Sr-Ba and Ni isotope data is not a result of different stellar models. Instead, the Sr-Ba and Ni data can be explained by adopting a larger ^{13}C -pocket with flattened ^{13}C concentrations, providing support for the large T17 pocket but probably with a reduced ^{13}C concentration. The grain-model agreement in Fig. 1 can be further improved if MS grains came from more massive AGB stars with higher stellar temperatures so that the $^{22}\text{Ne}(\alpha, n)^{25}\text{Mg}$ reaction can operate more efficiently,

producing higher $\delta^{88}\text{Sr}$ values in Fig. 1(a) as well as steeper slopes in Figs. 1(b) & (c).

Y/Z Grain Constraint: Y and Z grains have higher ^{30}Si excesses than MS grains, which likely indicates their origins from AGB stars with lower metallicities relative to the parent stars of MS grains by about a factor of 2–3 (e.g., [9]). We found *s*-process Mo isotopic compositions in 18 of 21 Y, 18 of 21 Z, and 12 of 15 MS grains (Fig. 2). Assuming that the *s*-process indeed operated efficiently in all AGB stars, the normal Mo isotopic compositions measured in some grains probably indicate that up to 20% of grains suffered from severe Mo contamination.

Figure 2 shows that the most anomalous Mo isotope ratios observed in Y and Z grains are more extreme than those of MS grains. Since the *s*-process should in principle operate more efficiently in lower-metallicity AGB stars because of enhanced neutron/seed ratios, the more anomalous Mo isotope ratios of Y and Z grains support the conclusion that their parent AGB stars had lower metallicities than the parent stars of MS grains. In addition, the difference in the *s*-process endmember between Y/Z and MS grains can be explained by the difference between the original and D3 cases, respectively (Fig. 2). Since the *s*-process efficiency is a function of the neutron/seed ratio, the model predictions in the original case for a $0.5 Z_{\odot}$ AGB star are similar to those in the D3 case for a $0.177 Z_{\odot}$ AGB star, except for the slightly higher stellar temperature of the latter. Thus, comparison of grain data to the new Torino AGB models with the T17 pocket implemented for Mo isotope ratios also implies that Y and Z grains came from AGB stars with metallicities up to three times lower than the metallicities of MS grain parent AGB stars, which is consistent with the constraints from light-element isotopic data.

Conclusion: We found that a large ^{13}C -pocket with flattened ^{13}C concentrations is required to consistently explain previous MS grain data on Sr, Ba, and Ni isotopes, which provides support for the dominant role of magnetic buoyancy in forming the ^{13}C -pocket; a reduced ^{13}C concentration could be achieved by additional mixing process(es), as a result of e.g., the stellar rotation motion. In addition, the T17 pocket can also be used to well explain the Mo isotope data of MS, Y, and Z grains, which likely implies the universality of ^{13}C -pockets in AGB stars with varying metallicities.

References: [1] Gallino R. et al. (1998) *ApJ*, 497, 388–403. [2] Liu N. et al. (2014a) *ApJ*, 786, #66 (20pp). [3] Liu N. et al. (2014b) *ApJ*, 788, #163 (7pp). [4] Liu N. et al. (2015) *ApJ*, 803, #12 (23pp). [5] Trappitsch R. et al. (2018) *GCA*, 221, 87–108. [6] Trippella O. et al. (2017) *ApJ*, 818, #125 (9pp). [7] Käppeler F. et al. (1994) *ApJ*, 437, 396–409. [8] Stephan et al. (2016) *IJMS*, 407, 1–15. [9] Amari S. et al. (2001) *ApJ*, 546, 248–266.

LLNL-ABS-744240.

LARGE MASS-DEPENDENT NICKEL ISOTOPE FRACTIONATION IN ORGUEIL CARBONATE: IMPLICATIONS FOR Fe-60 IN THE EARLY SOLAR SYSTEM. P. Boehnke^{1,2}, K. D. McKeegan³, T. Stephan^{1,2}, R. C. J. Steele⁴, R. Trappitsch⁵, A. M. Davis^{1,2,6}, M. J. Pellin^{1,2,6,7}, and M.-C. Liu³, ¹Department of the Geophysical Sciences, The University of Chicago, Chicago, IL, USA (pboehnke@gmail.com), ²Chicago Center for Cosmochemistry, Chicago, IL, USA, ³Department of Earth, Planetary, and Space Sciences, The University of California, Los Angeles, CA, USA, ⁴School of Earth and Environmental Sciences, University of St. Andrews, St. Andrews, UK, ⁵Lawrence Livermore National Laboratory, Nuclear and Chemical Sciences Division, Livermore, CA, USA, ⁶Enrico Fermi Institute, The University of Chicago, Chicago, IL, USA, ⁷Materials Science Division, Argonne National Laboratory, Argonne, IL, USA.

Introduction: Knowledge of the initial abundance of ⁶⁰Fe in the early Solar System is critical for understanding the astrophysical environment of the Sun's formation. This is because ⁶⁰Fe is produced only in stars and not by particle irradiation and has a relatively short half-life (2.62 My, [1]); therefore, a Solar System initial ⁶⁰Fe/⁵⁶Fe ratio, (⁶⁰Fe/⁵⁶Fe)₀, above the galactic background is seen to require a supernova trigger for Solar System formation. For this reason, numerous investigations have sought to determine (⁶⁰Fe/⁵⁶Fe)₀ (see [2], for a review).

High precision measurements of dissolved bulk samples of differentiated and chondritic meteorites by inductively coupled multi-collector plasma mass spectrometry (MC-ICP-MS) are in excellent agreement, and all find (⁶⁰Fe/⁵⁶Fe)₀ < 2 × 10⁻⁸ (e.g., [3]). In contrast, in-situ analyses by secondary ion mass spectrometry (SIMS) often find ⁶⁰Ni excesses in mineral phases with very high Fe/Ni ratios, leading to inferences of (⁶⁰Fe/⁵⁶Fe)₀ up to two orders of magnitude higher than the limits estimated from bulk measurements (e.g., [4,5]), which, if correct, would require an injection of supernova material within a few million years of Solar System formation.

SIMS measurements of nickel isotopes are challenging due to unresolvable isobaric interferences on ⁵⁸Ni by ⁵⁸Fe and on ⁶⁴Ni by ⁶⁴Zn. This means that SIMS nickel isotope measurements can only accurately determine relative abundances of ⁶⁰Ni, ⁶¹Ni, and ⁶²Ni. Therefore, the standard analytical procedure is to correct the measured ⁶⁰Ni/⁶²Ni ratio with the measured ⁶¹Ni/⁶²Ni ratio using an assumed mass fractionation law (e.g., [4,5]). However, ⁶¹Ni is a minor isotope, comprising only ~1.1% of nickel resulting in measurement precision on δ⁶¹Ni₆₂ lower than that of δ⁶⁰Ni₆₂, and therefore making the correction for natural mass-dependent fractionation problematic.

It is important to remember that there are two distinct phases of mass-dependent isotope fractionation, both of which need to be corrected for to accurately calculate any ⁶⁰Ni excess. The first occurs to the sample in nature, perhaps as a result of evaporation, condensation, or diffusion, and needs to be corrected for by measuring two additional isotopes of nickel besides

⁶⁰Ni (e.g., ⁶¹Ni and ⁶²Ni). The second occurs during the analysis (i.e., instrumental mass-fractionation) and can be corrected for by measuring standards under similar analytical conditions. In general, an uncorrected isotopic measurement is affected by the sum of these two independent mass-fractionations, and each must be corrected for before calculating the true ⁶⁰Ni excess. The primary concern in this work is with natural rather than instrumental mass-dependent fractionation.

Here, we present a case study of samples that yielded apparent Fe/Ni fossil isochrons when analyzed by SIMS. We then analyzed the same samples by resonance ionization mass spectrometry (RIMS), which can also reliably measure ⁵⁸Ni, even in the presence of high abundances of iron. We observe significant ⁶⁰Ni/⁶²Ni ratio variability that is clearly caused by mass-dependent isotope fractionation in the sample. Our results demonstrate that natural mass-dependent isotope fractionation of nickel, not previously recognized in SIMS analyses of meteorite samples, can lead to apparent isochrons. Finally, we show that the high inferred (⁶⁰Fe/⁵⁶Fe)₀ from SIMS measurements arises from incorrectly calculated uncertainties, particularly on the ⁶¹Ni/⁶²Ni ratios.

Methods: The samples in this study are three breunnerite grains from the Orgueil carbonaceous chondrite. These iron- and manganese-rich carbonates are characterized by very high Mn/Cr and Fe/Ni ratios, and thus are attractive samples in which to seek evidence for in-situ decay of extinct ⁵³Mn and ⁶⁰Fe. ⁵³Mn/⁵³Cr ages measured on two (Br-25 and Br-33) of these samples show that they formed within ~5 My of Solar System origin [6].

We carried out two analytical sessions for Fe/Ni ratios and nickel isotopes using both the UCLA CAMECA *ims1270* and *ims1290* ion microprobes. In the first session, using the *ims1270*, we collected ⁵⁶Fe⁺, ⁵⁷Fe⁺, ⁶⁰Ni⁺, and ⁶²Ni⁺ in monocollection mode using the axial Faraday cup for iron and the axial electron multiplier for nickel. The primary beam consisted of ~3 nA of O₂⁻ that was focused into a ~30 μm spot. The analyses were carried out at a mass resolving power *m/Δm* of ~5,000, which is sufficient to resolve most molecular mass interferences. Isotopic data were col-

lected after 120 s of presputtering to remove potential contamination from the sample surface. The second analytical session, using the *ims1290*, was nearly identical, with the only differences being collection of an additional mass, $^{58}\text{Fe}^+ + ^{58}\text{Ni}^+$, with the axial electron multiplier, a slightly more intense primary beam of ~ 5 nA of O^- , and 30 s of presputtering.

We performed RIMS analyses on the same samples using the CHICAGO Instrument for Laser Ionization (CHILI) [7]. Our RIMS measurements were carried out with a spatial resolution of <10 μm using a 351 nm desorption laser. The resonance ionization scheme for nickel is detailed in [7] and uses four lasers to ionize nickel atoms ablated from the sample from both the ground state and from a low-lying excited state, which contains $\sim 60\%$ of the desorbed nickel atoms [8]. We used a terrestrial siderite as our primary standard to correct for instrumental mass fractionation. San Carlos olivine was analyzed as a secondary standard and to investigate possible matrix effects. We corrected for a minor contribution of nonresonantly ionized ^{58}Fe on the ^{58}Ni peak by peak-stripping, based on the measured ^{56}Fe abundance and the Solar System $^{58}\text{Fe}/^{56}\text{Fe}$ ratio. This correction was <10 ‰ in all cases. Off-resonance analyses showed small peaks on masses 60 and 62, which we were not able to suppress and were corrected for based on the measured ^{56}Fe abundance. This correction was also small, <10 ‰ in most cases. The uncertainties in our measurements include contributions from counting statistics, background subtraction, and reproducibility of the mass fractionation correction on the standard.

Results: Our SIMS analyses of Orgueil carbonate Br-33 show an increase in $^{60}\text{Ni}/^{62}\text{Ni}$ ratio as a function of $^{56}\text{Fe}/^{62}\text{Ni}$ ratio. This is consistent with an apparent fossil isochron whose slope would imply an $^{60}\text{Fe}/^{56}\text{Fe}$ ratio of $(4.2 \pm 0.5) \times 10^{-7}$ (1σ) at the time of Br-33's formation; the correlation has a mean squared weighted deviation (MSWD) of 4.2. On the other hand, Br-25 shows an elevated but constant $^{60}\text{Ni}/^{62}\text{Ni}$ ratio as a function of $^{56}\text{Fe}/^{62}\text{Ni}$ ratio. A weighted linear regression for the Br-25 data suggests only an $^{60}\text{Fe}/^{56}\text{Fe}$ ratio of $(3 \pm 7) \times 10^{-8}$ (1σ) (MSWD = 1.1) at the time of Br-25's formation.

Our results from measuring these same carbonates using CHILI support the finding of $^{60}\text{Ni}/^{62}\text{Ni}$ ratio variability in Br-25 and Br-33. However, we observe a strong correlation of $\delta^{60}\text{Ni}_{58}$ with $\delta^{62}\text{Ni}_{58}$ that demonstrates that the $^{60}\text{Ni}/^{62}\text{Ni}$ ratio variability is entirely due to mass-dependent isotope fractionation. In two out of our three carbonates (Br-25 and Br-33), we find a large range of mass-dependent isotope fractionation of up to ~ 35 ‰/u, predominantly favoring the light isotopes. Indeed, once we internally normalized the data by cor-

recting for the natural isotope fractionation using the exponential law, they show no $\Delta^{60}\text{Ni}_{62/58}$ excesses that are resolved at the 2σ level.

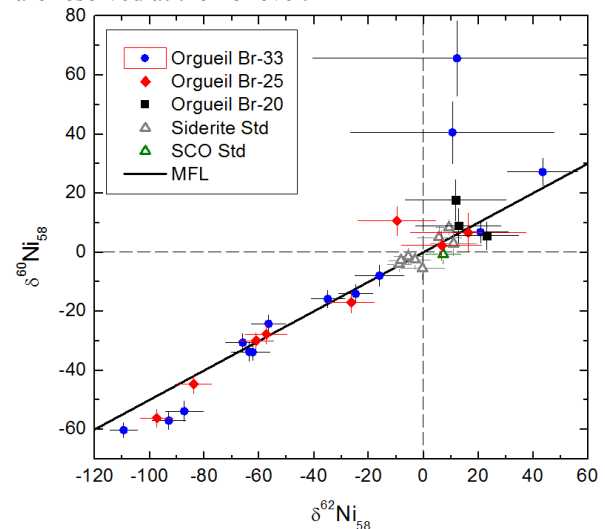


Figure 1: Ni isotopic compositions of individual spots from three Orgueil carbonates, measured using CHILI and normalized to a terrestrial siderite standard. San Carlos olivine (SCO) was measured in the same session to show the limited range of matrix effects. The line labeled “MFL” shows the line along which the measurements should plot if mass-dependent isotope fractionation has occurred. Uncertainties are 1σ .

Summary and outlook: We show that nickel isotopes in meteoritic samples, carbonates from Orgueil, can be isotopically fractionated with a range of 35 ‰/u and that SIMS cannot adequately measure mass-dependent isotope fractionation of nickel in high-Fe/Ni phases. Therefore, we conclude that any ^{60}Ni excess that is comparable to or smaller than 70‰ cannot be uniquely assigned to the decay of ^{60}Fe .

Next we plan to measure Fe/Ni ratios in addition to Ni isotopes using CHILI with our recently modified Ga ion gun to constrain the $(^{60}\text{Fe}/^{56}\text{Fe})_0$ of the Solar System.

References: [1] Rugel G. et al. (2009) *Phys Rev Lett*, 103, 7. [2] Elliott T. and Steele R. C. J. (2017) *Rev Mineral Geochem*, 82, 511–542. [3] Tang H. and Dauphas N. (2015) *Astrophys J*, 802, 22. [4] Mishra R. and Chaussidon M. (2014) *EPSL*, 398, 90–100. [5] Telus M. et al. (2012) *MAPS*, 47, 2013–2030 [6] Steele R. C. J. et al. (2017) *GCA*, 201, 245–259. [7] Stephan T. et al. (2016) *Int J Mass Spectrom*, 407, 1–15. [8] Trappitsch R. et al. (2018) *GCA*, 221, 87–108.

LLNL-ABS-744242

MINERALOGY, PETROGRAPHY, AND OXYGEN ISOTOPIC COMPOSITIONS OF ULTRAREFRACTORY INCLUSIONS FROM CARBONACEOUS CHONDRITES. A. N. Krot^{1*}, C. Ma², K. Nagashima¹, A. M. Davis³, J. R. Beckett², S. B. Simon⁴, M. Komatsu⁵, T. J. Fagan⁵, F. Brenker⁶, M. A. Ivanova⁷, and A. Bischoff⁸. ¹University of Hawai'i, USA, *sasha@higp.hawaii.edu; ²California Institute of Technology, USA; ³University of Chicago, USA. ⁴University of New Mexico, USA; ⁵Waseda University, Japan; ⁶Goethe University, Germany; ⁷Vernadsky Institute, Russia; ⁸Institut für Planetologie, Germany.

Introduction: Ca,Al-rich inclusions (CAIs) with Group II rare earth element (REE) patterns, enriched in less refractory REEs (La, Ce, Pr, Nd, Sm, and Tm), are thought to have condensed from a gaseous reservoir from which more refractory REEs (Gd, Tb, Dy, Ho, Er and Lu) were removed. The carrier(s) of ultrarefractory (UR) REE patterns are still poorly known; hibonite, perovskite, and Zr,Sc-rich phases have been previously considered as potential candidates. Several newly discovered Zr-, Sc-rich minerals in CAIs are potential carriers of UR REE patterns. Systematic studies of oxygen-isotope compositions and REE patterns of such CAIs are scarce. Here we report on the mineralogy, petrology and O-isotope compositions of UR CAIs from CO, CV, CR, and CM carbonaceous chondrites (CCs).

Analytical procedures: The mineralogy and mineral chemistry of UR CAIs were studied with backscatter electron imaging (BSE), electron backscatter diffraction (EBSD), and electron probe microanalysis (EPMA) at CalTech and UH. Oxygen isotopes were measured with the UH Cameca ims-1280 ion microprobe in multicollection mode (FC-EM-EM) using a 15–20 pA Cs⁺ primary beam focused to ~1 μm and rastered over 1×1 μm². Instrumental mass fractionation (IMF) was corrected using Burma spinel (for Zr- and Sc-rich phases, hibonite, spinel, and perovskite), augite (davisite, Sc-pyroxenes, and Al-diopside), San Carlos olivine (for olivine, low-Ca pyroxene, and anorthite), and quartz (for quartz).

Mineralogy and Petrography: The UR CAIs are found in CVs, COs, CRs, CHs, and CMs, where they occur as (i) individual irregularly-shaped (nodular-like) inclusions, (ii) minor constituents of amoeboid olivine aggregates (AOAs) and Fluffy Type A CAIs, (iii) relict inclusions in coarse-grained igneous CAIs (forsterite-bearing Type Bs and compact Type As), and (iv) relict inclusions in chondrules [1–17; this study].

The UR CAIs studied are typically small, < 30 μm in size, and dominated by Zr, Sc, Ti, and Y-rich minerals, including warkite (Ca₂Sc₆Al₆O₂₀), davisite (CaScAlSiO₆), Y-rich perovskite ((Ca,Y)TiO₃), tazheranite ((Zr,Ti,Ca)O_{2-x}), kangite ((Sc,Ti,Al,Zr,Mg,Ca,□)₂O₃), zirconolite CaZrTi₂O₇, eringaite Ca₃(Sc,Y,Ti)₂Si₃O₁₂, allendeite (Sc₄Zr₃O₁₂), lakargite (CaZrO₃), panguite ((Ti,Al,Sc,Mg,Zr,Ca)_{1.8}O₃), thortveitite (Sc₂Si₂O₇), and machiite ((Al,Sc)₂(Ti⁴⁺,Zr)₃O₉). These minerals are often associated with sub-μm grains of platinum group elements (PGEs: Ir, Os, Ru, Mo, and Wo). Most UR CAIs

appear to have escaped melting and are surrounded by Wark-Lovering (WL) rims of Sc-pyroxene, ±eringaite, Al-diopside, and ±forsterite. WL rims are absent around relict UR CAIs in igneous CAIs and chondrules, suggesting their destruction during melting.

Oxygen isotopes: On a three-isotope oxygen diagram, δ¹⁷O vs. δ¹⁸O, compositions of individual minerals from UR CAIs plot along ~slope-1 line. Note, however, since most minerals were analyzed without proper standards, the IMF effects cannot be properly corrected for; therefore, only mass-independent values, Δ¹⁷O = δ¹⁷O – 0.52×δ¹⁸O, are plotted in Fig. 1 and discussed below. Typical uncertainty on Δ¹⁷O is ~ 2.5‰ (2σ).

UR CAIs in CCs of petrologic type ≤3.1. Most UR CAIs from CCs of petrologic type ≤3.1 are isotopically uniform and have ¹⁶O-rich compositions (Δ¹⁷O ~ –23‰). The Murchison UR CAI *MURI* composed of spinel, thortveitite, panguite, davisite, and Sc-rich diopside [8] may be uniformly ¹⁶O-depleted: the only two minerals analyzed in this CAI, thortveitite and Sc-rich diopside, have Δ¹⁷O of ~ –8 to –5‰. There are 3 isotopically heterogeneous UR mineral-bearing objects: (1) #4 (circled number in Fig. 1), an intergrowth of ¹⁶O-rich corundum (Δ¹⁷O ~ –24‰) with euhedral ¹⁶O-poor machiite (Δ¹⁷O ~ 0‰) from Murchison [17], (2) #7, Sc-rich chondrule ZZ from MAC 88107 (CO3.1-like), and (3) #8, a relict hibonite-rich CAI in a type II chondrule (named by [18] as “FeO-rich fragment”) from Acfer 094 (C3.0 ungrouped). Chondrule ZZ consists of forsterite, Sc-bearing high-Ca and low-Ca pyroxenes, and baddeleyite, ± zirconolite. It may be an incompletely melted UR CAI-bearing AOA. Relict forsterite grains in this object retained ¹⁶O-rich signature (Δ¹⁷O ≤ –17‰), whereas olivine, Sc-bearing high-Ca and low-Ca pyroxenes, which appear to have crystallized from chondrule melt, have ¹⁶O-depleted compositions (Δ¹⁷O range from –5 to –4‰, from –4 to –2‰, and from –3 to 0‰, respectively), suggesting gas-melt isotope exchange during melt crystallization. The relict CAI from Acfer 094 consists of hibonite overgrown by Fe,Cr-bearing spinel; hibonite contains inclusions of zirconolite, tazheranite, perovskite, loveringite (Ca(Ti,Fe,Cr,Mg)₂₁O₃₈), and PGEs.

UR CAIs in CCs of petrologic type ≥3.1. Most UR CAIs in CCs of petrologic type ≥3.1 are isotopically heterogeneous. The isotopic heterogeneity appears to correlate with the mineralogy rather than with the inferred

crystallization sequence of individual CAIs. For example, spinel and hibonite of the CAI cores, and Al-diopside and forsterite of the WL rims are always ^{16}O -rich, whereas other minerals are ^{16}O -depleted to various degrees. The Allende UR CAI *Al-2* (#9) is an important exception. It consists of eringaite, spinel, perovskite, and davisite, and is a relict inclusion enclosed by a massive Al-diopside of the host forsterite-bearing CAI. The relict UR CAI shows a relatively small degree of isotope heterogeneity ($\Delta^{17}\text{O} \sim -25$ to -19%), with spinel being slightly ^{16}O -enriched relative to other minerals; spinel is isotopically similar to Al-diopside of the host CAI.

Discussion: The ^{16}O -rich and ^{16}O -poor reservoirs apparently co-existed during the earliest stages of Solar System evolution [e.g., 19–21]. It has been previously shown that most CAIs in CR2–3, CM2, and CO3.0 chondrites are uniformly ^{16}O -rich ($\Delta^{17}\text{O} \sim -23\%$) [22–25], indicating formation in a gas of approximately solar composition. In contrast, most CAIs in CCs of petrologic type ≥ 3.1 are isotopically heterogeneous: melilite, anorthite, grossite, and some Al,Ti-diopside grains are ^{16}O -depleted ($\Delta^{17}\text{O}$ up to $\sim 0\%$) relative to spinel, hibonite, forsterite, and Al-diopside, which are always ^{16}O -rich ($\Delta^{17}\text{O} \sim -23\%$) [e.g., 22, 25, 26]. The nature of this heterogeneity is controversial: condensation in a gas of variable O-isotope composition and postcrystallization O-isotope exchange in the solar nebular and on the chondrite parent asteroids are being discussed [22, 26–28]. We recently concluded that anorthite, melilite, and grossite in Kaba (CV3.1) and DOM 08004 (CO3.1) CAIs experienced O-isotope exchange with ^{16}O -poor aqueous fluids on their parent asteroids [25, 26]. $\Delta^{17}\text{O}$ of these fluids are inferred from $\Delta^{17}\text{O}$ of aqueously-formed fayalite and magnetite in CVs and COs ($-1.5 \pm 1\%$ and $-0.2 \pm 0.6\%$, respectively).

We suggest that the majority of isotopically heterogeneous UR CAIs from CV ≥ 3.1 s and CO ≥ 3.1 s we studied originated in an ^{16}O -rich gas of \sim solar composition, but subsequently experienced postcrystallization O-isotope exchange with aqueous fluids; some isotopically heterogeneous UR CAIs experienced exchange with an ^{16}O -depleted nebular gas during chondrule melting. The isotopically homogeneous UR CAIs preserved their original O-isotope compositions, which in most cases, were ^{16}O -rich. If UR CAI *MUR-1* from Murchison is indeed uniformly ^{16}O -depleted, it may have originated in an ^{16}O -depleted gaseous reservoir, similar to an isotopically uniform ($\Delta^{17}\text{O} \sim -9\%$) fine-grained spinel-rich CAI from the CB3.0 chondrite QUE 94627 [29].

References: [1] Davis A. (1984) *Meteoritics* 19, 214. [2] Davis A. (1991) *Meteoritics* 26, 330. [3] Weber D. & Bischoff A. (1994) *GCA* 58, 3855. [4] Simon S. et al. (1996) *MAPS* 31, 106. [5] El Goresy A. et al. (2002) *GCA* 66, 1451. [6] Uchiyama K. et al. (2008) *LPS* 39, #1519. [7] Ma C. et al. (2009) *LPS* 40, #1402. [8] Ma C. et al. (2011) *MAPS* 46, A144. [9] Ma et al.

(2011) *LPS* 42, #1276. [10] Ma C. (2011) *MAPS* 46, A144. [11] Ma C. (2012) *MAPS* 47, A256. [12] Ivanova M. et al. (2012) *MAPS* 47, 2107. [13] Ma C. et al. (2013) *Amer. Mineral.* 98, 870. [14] Ma C. et al. (2014) *LPS* 45, #1196. [15] Krot A. et al. (2015) *MAPS* 50, A111. [16] Simon S. & Grossman L. (2015) *MAPS* 31, 106. [17] Makide K. et al. (2013) *GCA* 110, 190. [18] Bischoff A. et al. (2006) in *MESS II*, 679. [19] Yurimoto H. et al. (2006) In *Protostars & Planets V*, 849. [20] Krot A. et al. (2008) *ApJ* 713, 1159. [21] Kööp L. et al. (2016) *GCA* 184, 151. [22] Yurimoto H. et al. (2008) *Rev. Mineral. Geochem.* 68, 141. [23] Makide K. et al. (2009) *GCA* 73, 5018. [24] Kööp L. et al. (2017) *GCA* 189, 70. [25] Simon S. et al. (2017) *LPS* 48, #1083. [26] Krot A. & Nagashima K. (2016) *MAPS* 50, #6104. [27] Aléon et al. (2007) *EPSL* 263, 114. [28] Simon J. et al. (2011) *Science* 331, 1175. [29] Krot A. et al. (2017) *GCA* 201, 155.

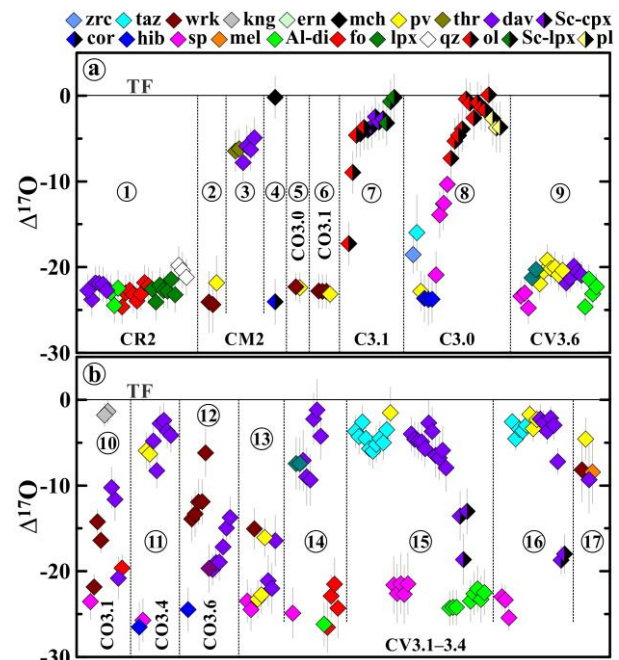


Fig. 1. $\Delta^{17}\text{O}$ of individual minerals in UR CAIs from CCs (1–4 from Y-793261; 2 – *Mur-1*, 3 – *MUR1*, 4 – *UH80-1* from Murchison; 5 – *100* from DOM 08006; 6 – *22-4* from DOM 08004; 7 – *ZZ* from MAC 88107; 8 – *17* from Acfer 094; 9 – *Al-2* from Allende; 10 – *YY* from DOM 08004; 11 – *Oscar* from Ornans; 12 – *Moss-1* from Moss; 13 – *V13*, 14 – *V3* from Vigarano; 15 – *3N-24* from NWA 3118; 16 – *33E* from Efremovka; 17 – *V7* from Vigarano). Al-di = Al-diopside; cor = corundum; dav = davisite; ern = eringaite; grs = grossite; hib = hibonite; kng = kangite; lpx = low-Ca pyroxene; mch = machiite; mel = melilite; ol = Fe-Mg olivine; pl = plagioclase; pv = perovskite; qz = quartz; Sc-px = Sc-rich Al,Ti-diopside (Sc-rich high-Ca pyroxene in 8); sp = spinel (Cr-spinel in 9); taz = tazheranite; thr = thortveitite; wrk = warkite. TF = terrestrial fractionation line. Most UR CAIs from CCs of petrologic type ≤ 3.1 are isotopically uniform, except CAIs incompletely melted during chondrule formation (#7, #8, and, possibly, #4). Most UR CAIs of petrologic type ≥ 3.1 are isotopically heterogeneous: hibonite, spinel, Al-diopside, and forsterite are always ^{16}O -rich, whereas warkite, kangite, eringaite, davisite, Sc-rich Al,Ti-diopside, tazheranite, perovskite, and melilite are ^{16}O -depleted to various degrees.

EVAPORATION KINETICS OF CAI-LIKE MELTS IN LOW-PRESSURE HYDROGEN GAS AND IN VACUUM: SIMILARITIES AND DIFFERENCES. M. Kamibayashi¹, R. A. Mendybaev^{2,3}, F. M. Richter^{2,3} and S. Tachibana^{1,4}. ¹Department of Natural History Sciences, Hokkaido University, Sapporo 060-0810, Japan (michiru@ep.sci.hokudai.ac.jp); ²Department of the Geophysical Sciences, ³Center for Cosmochemistry, University of Chicago, Chicago, IL 60637, USA; ⁴UTokyo Organization for Planetary and Space Science (UTOPS), University of Tokyo, Tokyo 113-0033, Japan.

Introduction: Coarse-grained igneous texture and strong enrichments in heavy magnesium, silicon and oxygen isotopes observed in some calcium-, aluminum-rich inclusions (CAIs) indicate that the CAI precursors have experienced highly energetic heating events that resulted in their melting and evaporation of moderately volatile elements and their associated isotopic fractionations. Extensive laboratory study have been conducted to reproduce chemical and isotopic signatures of the CAIs by evaporating CAI-like melts at high temperatures in vacuum (e.g., [1–5]). Despite the fact that the experiments successfully reproduce the major chemical and isotopic features of “normal” and FUN CAIs, an important concern was whether vacuum experiments adequately describe evaporation of CAI-like melts under low-pressure hydrogen conditions of the solar nebula. Richter et al. [2] evaporated CAI-like melt at 1500°C and $P_{H_2}=2\times 10^{-4}$ bar and showed that evaporation kinetics of Si and Mg is ~100 times faster than expected in vacuum. No direct comparison with vacuum experiments has been made due to very slow evaporation rates at 1500°C in vacuum. Here for the first time we report the results of the study on evaporation kinetics of Mg and Si from the same CAI-like melt that was evaporated at the same temperature (1600°C) in vacuum ($<10^{-7}$ bar) and in low-pressure H₂ gas (1.6×10^{-4} bar). Isotopic fractionation of Mg and Si in these evaporation experiments are reported in a companion abstract by Mendybaev et al. [6].

Experimental: As a starting material we used a composition (15.7 wt% MgO, 36.6 wt% SiO₂, 26.5 wt% Al₂O₃, 21.2 wt% CaO, labeled as CAI4B2) close to those of non-FUN forsterite-bearing CAIs of [7].

Low-pressure hydrogen experiments were conducted at Hokkaido University using premelted (at 1550°C in air) samples on a 0.25 mm diameter Ir-wire loop. The furnace with a sample was evacuated to better than 10^{-9} bar, preheated at 500°C for ~1 hr and after pressure in the chamber decreased below 10^{-9} bar, the sample was heated to 1600°C at ~20°C/min. After 5 min at 1600°C in vacuum, H₂ gas was introduced into the furnace at controlled flow rate such that pressure in the chamber was kept constant at 1.6×10^{-4} bar. After heating for a predetermined time period the sample was quenched by turning power off.

Vacuum evaporation experiments were conducted

at the University of Chicago using the same experimental protocol as in [2–5].

Weight and surface geometry of the samples were measured before and after each experiment. Texture and chemical composition of the evaporation residues were studied using a TESCAN LYRA3 FIB/FESEM with an Oxford AZtec x-ray microanalysis system.

Results: Run durations, chemical composition of the evaporation residues and the calculated evaporation rates of Mg and Si are presented in the table below.

Sample	time min	MgO wt%	SiO ₂ wt%	Al ₂ O ₃ wt%	CaO wt%	Mg lost mole %	Si lost mole %	J_{Mg} mol cm ⁻² s ⁻¹	J_{Si} mol cm ⁻² s ⁻¹
<i>low P_{H2} experiments</i>									
B2-1	0	15.71	36.58	26.52	21.19	0.2			
B2-2	3	15.37	35.17	27.62	21.85	4.6	6.3	9.7E-08	2.0E-07
B2-16	10	14.66	33.54	28.90	22.90	13.6	15.1	1.2E-07	2.1E-07
B2-12	20	12.62	31.44	30.99	24.96	31.2	26.4	1.3E-07	1.8E-7
B2-3	30	3.24	22.15	42.32	32.28	86.5	68.4	2.0E-07	2.2E-07
B2-14	35	9.42	28.89	34.16	27.53	52.9	38.0	1.4E-07	1.6E-07
B2-10	45	5.54	25.35	38.06	31.06	75.7	52.3	1.6E-07	1.7E-07
B2-4	60	0.02	0.73	63.03	36.22	99.9	99.1	1.3E-07	1.9E-07
<i>vacuum experiments</i>									
B2-25	300	14.35	34.00	27.92	23.72	16.0	14.5	3.7E-09	5.2E-09
B2-22	600	12.76	32.13	30.01	25.10	29.2	23.4	3.7E-09	4.6E-09
B2-21	1200	7.87	27.92	35.47	28.74	63.2	44.0	3.6E-09	3.9E-09
B2-23	1700	4.02	23.75	40.1	32.13	83.1	57.0	4.1E-09	4.4E-09
B2-20	1800	0.09	9.40	50.6	39.90	99.7	86.6	3.9E-09	5.4E-09
B2-24	2100	3.40	22.89	41.27	32.44	85.9	59.2	3.7E-09	4.0E-09
B2-18	2400	0.00	13.59	48.01	38.40	100.0	79.2	3.2E-09	3.9E-09

The typical textures of run products are shown in Fig. 1: most evaporation residues appear as clear glasses (Fig. 1a) except for the most evaporated samples that quenched into intergrowth of åkermanitic melilite plus glass (Fig. 1b) or into CaAl₂O₄ (Fig. 1c).

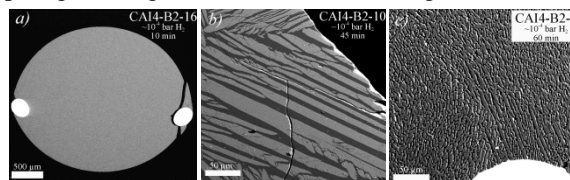


Fig. 1. Typical textures of CAI4B2 residues: a) clear glass CAI4B2-16; b) CAI4B2-10 quenched into intergrowth of åkermanitic melilite (light) plus glass (dark); c) CAI4B2-4 quenched into CaAl₂O₄.

Evaporation fluxes of Mg and Si were obtained by taking into account the initial and final weights and surface areas of a sample calculated assuming that molten droplets are spheroids with axis equal to a diameter of Ir-wire loop and to a thickness of the droplet. Corrections for size of the droplets at 1600°C were made using density-composition-temperature relationships of [8].

The table shows that Si in low-pressure H₂ experiments at 1600°C evaporate by ~35% faster than Mg:

$J_{Mg} \sim 1.4 \times 10^{-7}$ and $J_{Si} \sim 1.9 \times 10^{-7}$ moles/cm²/s. Evaporation rates of Si and Mg in vacuum experiments ($J_{Mg} \sim 3.8 \times 10^{-9}$ and $J_{Si} \sim 4.6 \times 10^{-9}$ moles/cm²/s) are about 40 times slower than in vacuum. Figure 2 shows that despite different evaporation rates of Si and Mg under the different conditions, their evaporation trajectories are the same. Compositions of most evaporation residues (excluding the most evaporated sample with MgO < 0.1 wt%) in Fig. 2 plot along a line with the same slope of ~ 1.4 .

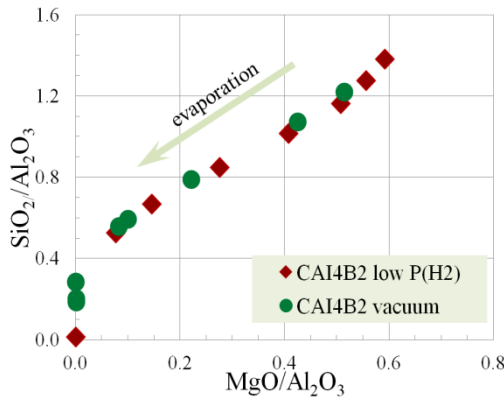


Fig. 2. Evaporation trajectories of CAI4B2 in low-pressure H₂ and in vacuum experiments at 1600°C.

Discussion: Figure 3 compares evaporation rates of Mg and Si from CAI4B2 melt in vacuum and in low-pressure H₂ at 1600°C with those of previous works with CAI-like melts [2-3]. The Figure shows that for all compositions studied (except for BCAI melt evaporated at P_{H2} = 2 × 10⁻⁴ bar at 1500°C [2]) Si evaporates somewhat faster than Mg. The reason for faster evaporation of Mg compared to Si from BCAI melt most likely is due to melt composition: starting BCAI melt is forsteritic, while all other melts are anorthitic or melilitic in composition.

Vacuum evaporation rate of Mg determined in this study is slightly higher than that for CAIB melt at 1600°C [3], but are in good agreement with extrapolation from higher temperatures [3].

The evaporation rates of Mg and Si at 1600°C in low-pressure H₂ (1.6 × 10⁻⁴ bar) are ~ 40 times larger than those in vacuum, while those at 1500°C and 1.8 × 10⁻⁴ bar were calculated to be ~ 100 times larger than in vacuum [2]. Mg evaporation rate measured in our experiments is consistent with the extrapolated value from [2], which calculated the evaporation rates of Mg from CAI-like melt at 1500–1300°C when the evaporation coefficient of ~ 0.07 was adapted. The evaporation coefficient of ~ 0.07 is also consistent with those reported in vacuum experiments [2, 3].

The difference in evaporation rates in vacuum and in low-pressure hydrogen can be explained by the increase in the equilibrium vapor pressures of Mg and Si

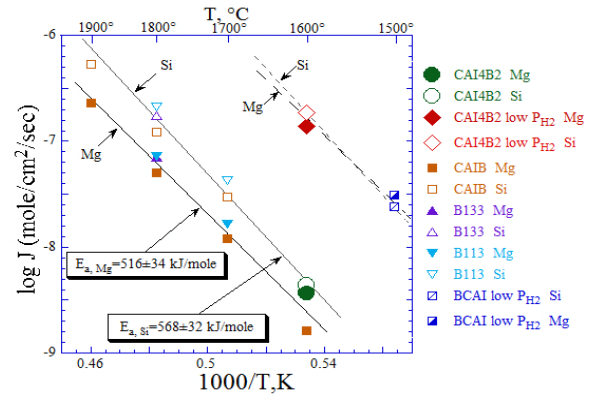


Fig. 3. Evaporation rates of Mg (closed symbols) and Si (open symbols): CAI4B2 – this work; CAIB – from [3]; B133, B113, BCAI – from [2].

when H₂ is present. While hydrogen promotes much faster evaporation of Mg and Si from CAI-like melts, it does not change the evaporation trajectory.

Using all available data on evaporation rates of Mg and Si from CAI-like melts (Fig. 3), we determined activation energies $E_{a,Mg} = 516 \pm 34$ kJ/mole and $E_{a,Si} = 568 \pm 32$ kJ/mole for vacuum evaporation. These activation energies also fit experimentally determined evaporation rates at P_{H2} $\sim 2 \times 10^{-4}$ bar at 1500°C and 1600°C (dashed lines in Fig. 3).

Conclusions: 1) Evaporation at 1600°C in low pressure H₂ (1.6 × 10⁻⁴ bar) is faster than in vacuum, as expected; 2) chemical evaporation trends in low-pressure H₂ and in vacuum are the same; 3) the evaporation rates of Mg and Si from molten CAI-like liquids can be expressed as $J_i = J_{0i} e^{-E_{RT}}$ with, in case of vacuum evaporation, $J_{0Mg} = 6.0 \times 10^5$ mol/cm²/s, $J_{0Si} = 3.4 \times 10^7$ mol/cm²/s and activation energies of 516 ± 34 kJ/mol for Mg and 568 ± 32 kJ/mol for Si. To model evaporation under more realistic solar nebula pressure of P_{H2} $\sim 2 \times 10^{-4}$ bar, $J_{0Mg} = 3.5 \times 10^7$ mol/cm²/s and $J_{0Si} = 1.3 \times 10^9$ mol/cm²/s should be used. For other compositions and other hydrogen pressures the values of J_{0i} are proportional to their vapor pressure that can be calculated by thermodynamic modeling as described in [9].

References: [1] Davis A. M. et al. (1990) *Nature*, 347, 655–658; [2] Richter F. M. et al. (2002) *GCA*, 66, 521–540; [3] Richter F. M. et al. (2007) *GCA*, 71, 5544–5564; [4] Mendybaev R. A. et al. (2013) *LPSC 44th*, Abstract #3017; [5] Mendybaev R. A. et al. (2017) *GCA*, 201, 49–64; [6] Mendybaev R. A. et al. (2018) *LPSC 49th* (this volume); [7] Bullock E. S. et al (2012) *Meteoritics*, 47, 2128–2147; [8] Lange R. A. and Carmichael I. S. (1987) *GCA*, 51, 2931–2946; [9] Grossman L. et al. (2000) *GCA*, 64, 2879–2894.

FIRST-PRINCIPLE COMPUTATIONS OF EQUILIBRIUM POTASSIUM ISOTOPIC FRACTIONATION IN ORTHOCLASE. H. Zeng¹, N. Dauphas¹, M. Meheut², M. Blanchard², G. Galli^{3,4}, ¹Origins Lab, Department of the Geophysical Sciences and Enrico Fermi Institute, The University of Chicago (dauphas@uchicago.edu), ²Géosciences Environnement Toulouse, Observatoire Midi-Pyrénées, CNRS UMR 5563, Université Paul-Sabatier, ³Institute for Molecular Engineering, The University of Chicago, ⁴Materials Science Division, Argonne National Laboratory, IL

Introduction: The isotopic compositions of minerals and rocks provide important clues on the processes that shaped the composition of planetary bodies. As an example, Wang and Jacobsen used the heavy potassium isotopic composition of lunar rocks as evidence arguing that a high-energy and high-angular momentum giant impact scenario was responsible for the formation of the Moon, and casting some doubts on the canonical model.^[1] Experimentally examining some of the processes responsible for fractionating isotopes in lunar rocks is highly challenging due to the extreme conditions associated with the Moon forming impact.

Among various approaches to all these seemingly intractable problems, first-principle calculation based on density functional theory (DFT) has been proven to be an extremely versatile tool, which was used to investigate intricate chemical reaction mechanisms^[2] and crystal structures of material in the core of planets.^[3] Herein, we present a first-principle computation of the reduced partition function ratio (β factors) for K in potassium bearing mineral, orthoclase. The rationale for calculating the β factor for potassium in orthoclase is that during condensation of K from circumterrestrial debris to the moon, K would condense into silicates, and orthoclase is taken as the model of silicates during the formation process. We are interested in understanding how K isotopes would partition during the condensation to understand what caused K isotope variations in lunar samples and pose further constraints on the giant impact theory.

Method: The computation is based on DFT and conducted using the Quantum ESPRESSO software.^[4] Plane-wave basis set and Perdew-Burke-Ernzerhof (PBE) generalized gradient approximation (GGA)^[5] as exchange correlational functional were employed. Pseudopotentials were obtained from the ONCV library.^[6] The large size of the orthoclase unit cell, which contains 52 atoms, made the computation process time consuming and at the time of writing this abstract, the influence of some parameters are still being tested. The cutoff energy (85 Ry) and the size of a uniform Monkhorst-Pack k-point grid^[7] (3x2x3) were determined as the total energy converged within 15 meV/atom. The convergence with respect to q-point (under test and will be published in the poster) was determined as doubling the number of q points with $\ln\beta$ changing less than 0.1‰.

Starting from the experimental structure of orthoclase,^[8] the crystal structure was first relaxed until the difference in total energy between two consecutive self-consistent iterations was less than 10^{-4} Ry with a force convergence threshold 5×10^{-4} a.u. and a pressure convergence threshold 0.1 Kbar. After structural relaxation, phonon dispersion relationships for two different isotopes (³⁹K, ⁴¹K) were computed based on density functional perturbation theory (DFPT or linear response).

The equilibrium isotopic fractionation factor of an element Y between two phases a and b can be written in the form of reduced partition functions ratios β :

$$\alpha(a, b, Y) = \frac{\beta(a, Y)}{\beta(b, Y)}$$

where $\beta(a, Y)$ is the reduced partition function ratio between phase a and a perfect gas of elemental Y. The β factors can be computed from the vibrational frequencies of a given material through following equation:^[9]

$$\beta = \left(\prod_{i=1}^{3N} \prod_{\{q\}} \frac{v_i}{v'_{q,i}} \times \frac{e^{-\frac{hv_{q,i}}{2kT}}}{1 - e^{-\frac{hv_{q,i}}{kT}}} \times \frac{1 - e^{-\frac{hv'_{q,i}}{kT}}}{e^{-\frac{hv'_{q,i}}{2kT}}} \right)^{\frac{1}{nN_q}}$$

where $v_{q,i}$ and $v'_{q,i}$ are the vibrational frequencies of the vibrational mode i with wave vector q , N is the number of atoms in the unit cell, and N_q is the number of q points in the Brillouin zone. The calculation was done independently in Chicago and Toulouse (the parameters listed above are for the Chicago computation), so as to compare the reproducibility of the DFT calculation and the influence of some of the choices made in DFT calculations. Huang et al.^[10] previously calculated the β factor of K in orthoclase and their results differ from preliminary calculations.

Results: The relaxed lattice parameters are provided in Table 1. They agree well with experimentally measured values.^[8] A preliminary result of computed β factors from Toulouse is shown in Fig. 1 with the calculated β factor expressed in term of $\ln\beta$ and fitted against $\frac{1}{T^2}$. The Chicago results and a comparison between the two results will be presented in the conference with greater details.

	Calculation	Experiment	Difference
a (Å)	8.774	8.588	2.2%
b (Å)	13.107	13.005	0.8%
c (Å)	7.306	7.192	1.6%
beta	115.582°	116.026°	-0.4%

Table 1. Calculated and experimental lattice parameters of orthoclase (monoclinic).

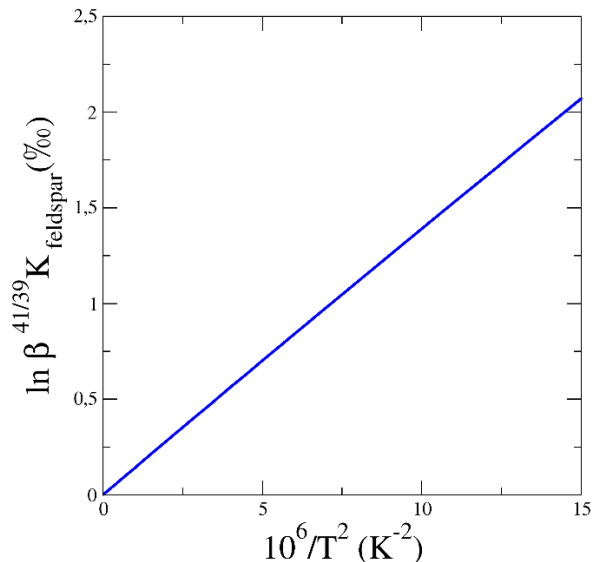


Figure 1. Calculated $\ln\beta$ versus $\frac{1}{T^2}$. The fitted relationship is $1000\ln\beta^{41/39}K = 0.143 \times \frac{10^6}{T^2}$ (Toulouse calculation; the Chicago results will be presented at the conference).

Conclusion: We provide a detailed scheme of first-principle computation of the equilibrium fractionation ratios for orthoclase. The implications of those calculations on interpretations of the K isotopic record of lunar rocks will be discussed at the conference.

References:

- [1] K. Wang, S. B. Jacobsen, *Nature* **2016**, 538, 487.
- [2] K. Honkala, A. Hellman, I. N. Remediakis, A. Logadottir, A. Carlsson, S. Dahl, C. H. Christensen, J. K. Nørskov, *Science* **2005**, 307, 555-558.
- [3] K. Umemoto, R. M. Wentzcovitch, P. B. Allen, *Science* **2006**, 311, 983-986.
- [4] aG. Paolo, et al., *Journal of Physics: Condensed Matter* **2009**, 21, 395502; b P. Giannozzi, et al., *Journal of Physics: Condensed Matter* **2017**, 29, 465901.
- [5] J. P. Perdew, K. Burke, M. Ernzerhof, *Physical Review Letters* **1996**, 77, 3865-3868.
- [6] D. R. Hamann, *Physical Review B* **2013**, 88, 085117.
- [7] H. J. Monkhorst, J. D. Pack, *Physical Review B* **1976**, 13, 5188-5192.

- [8] H.-Y. Tseng, P. J. Heaney, T. C. Onstott, *Physics and Chemistry of Minerals* **1995**, 22, 399-405.
- [9] J. Bigeleisen, M. G. Mayer, *The Journal of Chemical Physics* **1947**, 15, 261-267.
- [10] Huang S. et al., in *LPSC 47*, **2016**, p. 2261.

INSIGHTS INTO REDOX CYCLING ON EARLY EARTH FROM THE MASS FRACTIONATION LAW OF IRON ISOTOPES IN ARCHEAN SEDIMENTS. A. W. Heard¹, N. Dauphas¹, O. J. Rouxel², N. X. Nie¹, ¹Origins Laboratory, Department of the Geophysical Sciences and Enrico Fermi Institute, The University of Chicago, 5734 South Ellis Avenue, Chicago, IL 60637, United States (andyheard@uchicago.edu), ²Department of Oceanography, University of Hawaii, Honolulu, HI 96822, United States.

Introduction: Iron is an element of great astrobiological interest because of its abundance in planetary surface environments, its multiple redox states, and its processing by microbial metabolisms. The presence of ferric iron in Archean banded iron formations (BIF) indicates that iron oxidation occurred in the surface ocean at a time when the atmosphere and deep ocean on Earth were anoxic. Removal of ferric iron left an imprint on Archean ocean chemistry [1], and deposition of ferric iron on the anoxic sea floor created redox disequilibria ripe for exploitation by microbial life such as through dissimilatory iron respiration (DIR), a metabolism which emerged very early in the history of life on Earth [2-3]. Recent discoveries by the Mars Science Laboratory mission have revealed that an ancient lake in Gale Crater also hosted a redox stratified environment, where Fe (and Mn) oxidized in near surface waters were deposited in disequilibrium with an anoxic lake bottom [4].

Redox processes induce large fractionations in iron isotope ratios, and among BIF and sedimentary pyrites there is a >4‰ variation in $\delta^{56}\text{Fe}$ of Archean rocks. Removal of isotopically heavy ferric iron oxides to create BIF with positive $\delta^{56}\text{Fe}$ should have left the Archean ocean with an isotopically depleted ferrous iron reservoir [1]. The case has been made [1] that this depleted reservoir was recorded in shales and sedimentary pyrites, which feature extremely negative $\delta^{56}\text{Fe}$. These signatures cannot be, however, uniquely interpreted as reservoir effects because secondary processes, such as kinetic effects during pyrite mineralization [5], or DIR [6], also create isotopically depleted ferrous iron phases. The extent of fractionation in a single iron isotope ratio cannot distinguish between these various processes; but the slope of the mass-fractionation law for two iron isotope ratios, $\delta^{56}\text{Fe}$ and $\delta^{57}\text{Fe}$, may be distinct for different fractionation processes and therefore confirm or deny genetic relationships between different sedimentary reservoirs. We are conducting high-precision triple iron isotope analyses on a suite of Archean sedimentary rocks with a large range of $\delta^{56}\text{Fe}$ to assess any variation in the mass fractionation law.

Samples and methods: BIF samples are from South Africa, Western Australia, Baffin Island and Greenland and span an age range of 3.8 – 2.3 Ga (billion years). Shales and associated pyrites are from

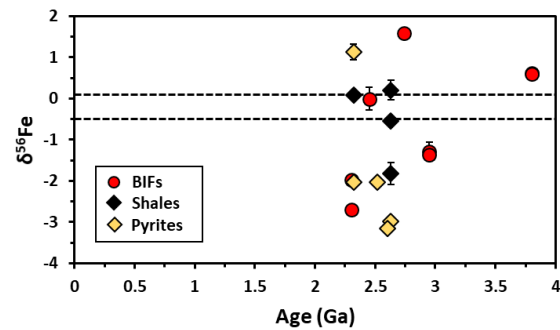


Figure 1: Age and iron isotopic composition expressed as $\delta^{56}\text{Fe}$ of BIF, shale and pyrite samples analyzed in this study. The black dashed lines represent the range of possible initial oceanic values.

2.63 – 2.32 Ga sedimentary basins in South Africa and Western Australia (all shown in Fig. 1).

Powdered rock samples and whole clean pyrite grains were digested in HF-HNO₃-HClO₄, then HCl-HNO₃-HClO₄, and separation of iron was performed on AG1-X8 200-400 mesh Cl-form anion exchange resin using standard [7-8] and long column [9-10] chemistry procedures. Isotopic analyses were made on a Neptune MC-ICPMS in high resolution mode with an Aridus II desolvating nebulizer. Standard-sample bracketing was used and uncertainties are expressed as the 95 % confidence interval of average values. The slope of the mass fractionation law was determined by internal normalization of ⁵⁶Fe/⁵⁴Fe to a fixed ⁵⁷Fe/⁵⁴Fe along the reference exponential law (Fig. 2).

Mass fractionation laws: Mass fractionation laws imparting precise slopes in three-isotope diagrams have previously been studied for O, Mg, S, Ca, Ti, and Fe [9-16], but this has yet to be investigated for Fe isotopes in multiple sedimentary rocks. Mass fractionation laws are straight lines in three-isotope diagrams when the δ' notation is used:

$$\delta' = 1000 \times \ln((\delta/1000)+1).$$

The slope θ for the three-isotope diagram can be parameterized as:

$$\theta_{i1,i2,i3} = \frac{m_{i2}^n - m_{i1}^n}{m_{i3}^n - m_{i1}^n},$$

where m_i the mass of the isotope i [17]. The value of n characterizes the slope of different mass-dependent fractionation laws.

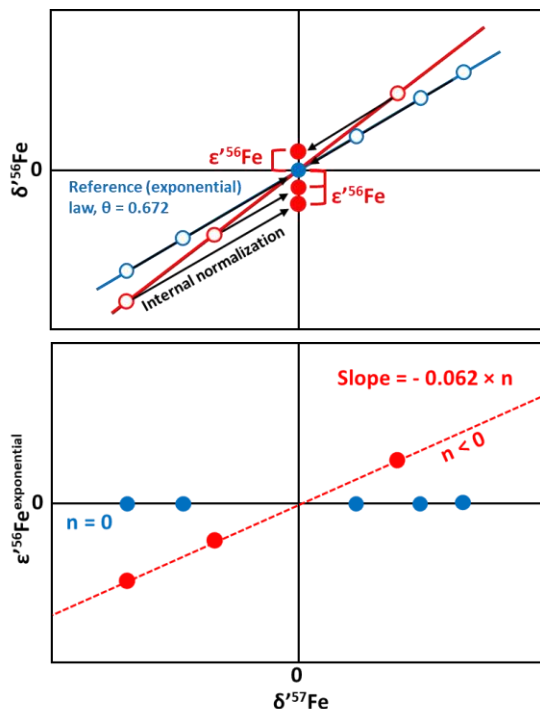


Figure 2: *Top.* Illustration of internal normalization of $\delta^{56}\text{Fe}$ values to a fixed $^{57}\text{Fe}/^{54}\text{Fe}$ along the reference exponential law. Open and closed symbols represent measured and internally normalized values respectively. *Bottom.* Slope of a sample mass fractionation law (red) relative to the reference law (blue) in $\epsilon'^{56}\text{Fe}$ vs. $\delta^{57}\text{Fe}$. Slopes are not to scale.

Slopes in three-isotope space vary only subtly, so for visualization purposes one isotope ratio is given as its deviation from the exponential law in parts per 10^4 by using the ϵ' notation (Fig. 2). A Taylor approximation relates the slope of ϵ' vs. δ' directly to n , to give the equation for iron isotopes [10]:

$$\epsilon'^{56}\text{Fe} = -0.062 \times n \times \delta'^{57}\text{Fe}.$$

Processes that have different iron isotope mass fractionation laws will have different values of n , and thus their products will have distinct $\epsilon'^{56}\text{Fe}$ vs. $\delta'^{57}\text{Fe}$ slopes.

Results and conclusions: High precision data on the mass fractionation law for BIF have been obtained and analysis of shales and pyrites is ongoing. The BIF samples span a range of $>4\%$ in $\delta^{56}\text{Fe}$, with the most isotopically depleted compositions being found in Mn-rich iron formations formed around the time when the terrestrial atmosphere first became oxygenated. The data follow a single mass fractionation line in $\epsilon'^{56}\text{Fe}$ vs. $\delta^{57}\text{Fe}$ with a slope of 0.057 ± 0.006 , which corresponds to an exponent $n = -0.91 \pm 0.09$. Therefore the BIF mass fractionation law is in agreement with the high-temperature equilibrium limit law ($n = -1$) and with ferrous and ferric iron reservoirs formed by UV photo-oxidation of aqueous ferrous iron ($n = -1.05 \pm$

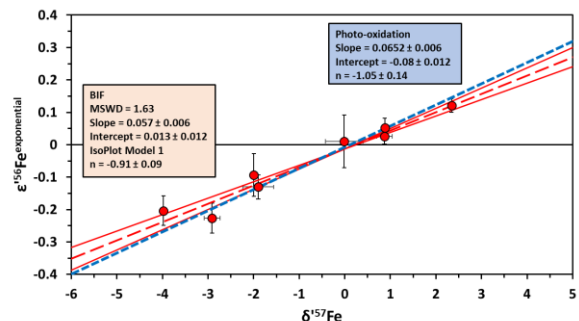


Figure 3: Mass fractionation law (red dashed line) for a number of BIF samples (red circles). The slope of the fractionation law is consistent with that found for the UV photo-oxidation process (blue dashed line) [16].

0.14) [16]. That process has been proposed to have caused iron oxidation on early Earth [18] and Mars [4,16], and the hypothesis is consistent with isotopic data from this study. If Archean shale and pyrite iron isotope signatures passively record the depletion of the oceanic iron reservoir by ferric oxide removal [1], then those samples would follow the same mass fractionation law as BIF. If those samples follow a different mass fractionation law such a result will indicate secondary processes played a major role in their isotopic depletion. Therefore our work will shed light on redox processes in Earth's earliest oceans and possibly biological processes involved in the deposition and reworking of iron-rich chemical sediments.

References: [1] Rouxel, O. J. *et al.* (2005) *Science*, 307, 1088-1091. [2] Vargas, M. *et al.* (1998) *Nature*, 395, 65-67. [3] Lovley, D. R. (2004) *Origins*, 299-313. [4] Hurowitz, J. A. *et al.* (2017) *Science*, 356, eaah6849. [5] Guilbaud, R. *et al.* (2011) *Science*, 332, 1548-1551. [6] Beard, B. L. *et al.* (1999) *Science*, 285, 1889-1892. [7] Dauphas, N. *et al.* (2004) *Anal. Chem.*, 76, 5855-5863. [8] Dauphas, N. *et al.* (2009) *Chem. Geol.*, 267, 175-184. [9] Tang, H. *et al.* (2009) *LPS XXXX*, Abstract #1903. [10] Tang, H. and Dauphas, N. (2012) *EPSL*, 359-360, 248-263. [11] Angert, A. *et al.* (2003) *Glob. Biogeochem. Cycles*, 17, 1030. [12] Young *et al.* (2002) *GCA*, 66, 1095-1104. [13] Davis, A. M. *et al.* (2015) *GCA*, 158, 245-261. [14] Farquhar, J. *et al.* (2003) *Geobiology*, 1, 27-36. [15] Zhang, J. *et al.* (2014) *GCA*, 140, 365-380. [16] Nie N. X. *et al.* (2017) *EPSL*, 458, 179-191. [17] Dauphas, N. and Schauble, E. A. (2016) *Ann. Rev. Earth Planet. Sci.*, 44, 709-783 [18] Cairns-Smith, A. G. (1978) *Nature*, 276, 807-808.

Acknowledgements: This work was funded by NASA Habitable Worlds (NNH16ZDA001N) Grant 16-HW16_2-0110 to N. Dauphas and A. W. Heard.

CAN LUNAR FORMATION THEORIES BE TESTED WITH K ISOTOPES? N. Dauphas¹, M. Meheut², M. Blanchard², H. Zeng¹, G. Galli^{3,4}, R.N. Canup⁵, C. Visscher⁶, N. Nie¹, ¹Origins Lab, Department of the Geophysical Sciences and Enrico Fermi Institute, The University of Chicago (dauphas@uchicago.edu), ²Géosciences Environnement Toulouse, Observatoire Midi-Pyrénées, CNRS UMR 5563, Université Paul-Sabatier, ³Institute for Molecular Engineering, The University of Chicago, ⁴Materials Science Division, Argonne National Laboratory, IL, ⁵PSD, Southwest Research Institute, Boulder, ⁶Dordt College, Sioux Center.

Introduction: The chemical compositions of lunar rocks differ in several respects from those of terrestrial rocks [1]. Among those distinguishing features is the depletion in volatile element K in the Moon relative to the Earth. The abundance of K is most often normalized to that of U because both elements have incompatible behaviors during magmatic processes but U is highly refractory, so the K/U is a simple and direct measure of depletion in volatile element K in planetary bodies (e.g., see Fig. 3 of ref. [2]). Relative to CI chondrites, the Earth is depleted in K by a factor of ~6 while the Moon is depleted by a factor of ~28. For comparison, angrites are depleted in K by a factor of ~110 while chondrites span a range from 0.8 (*i.e.*, an enrichment) for EL to ~4 for CV.

The reason for this depletion is poorly understood. It could have arisen from collision of an ultra-depleted impactor with the protoEarth only if over 80% of the Moon was derived from the impactor, which is achieved in some canonical impact models. If 70% of the Moon came from a K-depleted impactor like angrites [3], the inherited depletion factor in the Moon would have been ~18 [$1/(0.7/110+0.3/6)$], falling short of explaining the K depletion seen in the Moon. Advocating a high impactor contribution in the Moon (>80%) makes the problem of the Earth-Moon isotopic similarity in O, Ti and W more acute. This suggests that the giant impact event must have induced some loss of K.

Vaporization and condensation are processes that are known to induce equilibrium and kinetic isotopic fractionations. Early K isotope measurements showed that lunar rocks had the same isotopic compositions as Earth and chondrites [4] but the precision of those measurements was limited. A recent study revisited this question and found that lunar rocks were enriched in the heavy isotopes of K by +0.4 ‰ [5]. Wang and Jacobsen [5] used this observation to question the canonical giant impact scenario and argued that this was entirely consistent with a high-energy impact scenario involving near-complete homogenization of the Moon and Earth [6-7]. They however did not examine all plausible scenarios for fractionation of K isotopes during impact.

Two important processes can fractionate K isotopes during either vaporization or condensation [8 and ref-

erences therein]. One is kinetic isotopic fractionation, which stems from the kinetic theory of gases through the Hertz-Knudsen equation. This fractionation follows from the consideration that light atoms or molecules tend to impinge surfaces at a higher rate than heavier species. The implication is that evaporation tends to enrich the solid/liquid residue in the heavy isotopes while condensation tends to enrich the condensed phase in the light isotopes. The second process is equilibrium, which leads to enrichments in the heavy isotopes in the phases that forms the strongest bonds. In the case of equilibrium between condensed phase and gas, the former will usually have heavy isotopic composition relative to the latter. The extent to which K depletion will be accompanied by K isotopic fractionation will depend on the role played by these various processes. Very few laboratory experiments have studied K isotopic fractionation during vaporization but important insights can be gained based on theoretical considerations.

Below, we evaluate how equilibrium and kinetic processes could have shaped K isotopic fractionation in the terrestrial and lunar rocks, and discuss implications for Moon-formation theories.

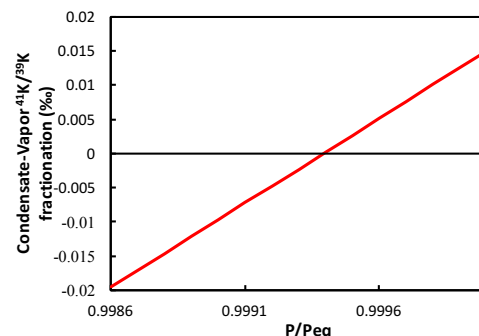


Fig. 1. Instantaneous K isotopic fractionation during condensation (see text and refs. 12 and 13 for details).

Equilibrium and kinetic isotopic fractionation between gas and condensate: Equilibrium isotopic fractionation. Knowing the phases involved and temperature of equilibration is all that is needed to calculate equilibrium isotopic fractionation. Under reasonable conditions for an impact-generated disk, K will condense in the temperature range 4000-3000 K [9-11] with gas K primarily speciated as gaseous atomic K.

For the condensed phase, we used microcline and orthoclase as model silicate compositions (KAlSi_3O_8). The equilibrium isotopic fractionation between coexisting phases (in ‰) is given by the difference in the logarithm of their reduced partition function ratios $1000 \ln \beta$. For an ideal monoatomic gas, $1000 \ln \beta = 0$. We calculated the value of $1000 \ln \beta$ of microcline using the DFT technique. At a temperature of 3000 K, we find an equilibrium fractionation Δ_{eq} between condensate and gas of 0.015 ‰ while a temperature of 4000 K yields a fractionation of 0.009 ‰ for the $^{41}\text{K}/^{39}\text{K}$ ratio. Huang et al. [10] previously reported K equilibrium isotopic fractionation and found values of ~ 0.029 and 0.017 ‰, respectively. These are higher than our calculated values by a factor of 2. Both sets of values are low in regard to the measured isotopic fractionation in lunar rocks.

Kinetic isotopic fractionation. Some high energy impact scenarios consider that sufficient equilibration must have taken place so as to allow the mantle of the Earth to have fully exchanged isotopically with the lunar disk [6,7]. It is thus likely that the vapor was either equilibrated with the condensed phase or simply inherited its composition from the Theia-protoEarth system if everything was vaporized. Any kinetic fractionation would thus most likely have taken place during condensation. Because light isotopes impinge surfaces at a higher rate than heavy isotopes, kinetic fractionation leads to an enrichment in the light isotopes of the condensate [12,13]. The extent of this fractionation is however going to depend on the degree to which the gas is supersaturated relative to thermodynamic equilibrium. If the gas is highly supersaturated (and neglecting any possible mass-dependence of the condensation coefficients), then the kinetic isotopic fractionation factor between condensate and vapor is $\Delta_{\text{ki}} = 1000[(39/41)^{0.5} - 1] = -24.7$ ‰. If the vapor pressure is equal to the equilibrium vapor pressure, then only equilibrium isotopic fractionation will be present.

Isotopic fractionation during condensation. In general, the isotopic fractionation between condensate and gas will depend on $p = P_{\text{eq}}/P$ (where P_{eq} is the equilibrium vapor pressure) [14] (Fig. 1),

$$\Delta_{\text{cond}} = p\Delta_{\text{eq}} + (1-p)\Delta_{\text{ki}}$$

A complicating factor is whether the condensate remains in isotopic equilibrium with the vapor throughout condensation or it is effectively removed (because of kinetic barriers to isotopic exchange). These end-member scenarios can be modeled with batch or distillation models.

Discussion: The observation that needs to be explained is the $\sim +0.4$ ‰ K isotopic fractionation between lunar and terrestrial rocks at $\sim 80\%$ K loss. Ki-

netic effects, because they would presumably enrich the condensates in the light isotopes, cannot explain the heavy isotope enrichment of the Moon relative to the Earth. Batch equilibrium also cannot explain this fractionation because the equilibrium fractionation factor is too small. A Distillation model does not help because the heaviest that the condensate can get is the equilibrium fractionation factor at the onset of condensation. If kinetic effects are present, the isotopic fractionation could be much higher but it would be opposite in sign. Our *ab initio* calculation and theoretical considerations suggest that to first order, the isotopic fractionation imparted to condensates in the aftermath of an energetic giant Moon-forming impact should be smaller or even opposite in sign to the observed K isotopic enrichment measured in lunar rocks. Wang and Jacobsen [5] reached an opposite conclusion because they considered evaporation as the driver for the isotopic fractionation but it is not clear what the physical setting would be for such evaporation to take place. The only way that this could work is if some condensates are re-evaporated because of decoupling with the gas but this is not a straightforward prediction of the model. Re-evaporation of condensates or moonlets after decoupling from the gas in the canonical model would also lead to heavy isotope enrichments in low-energy impact scenarios. Fundamentally, there is nothing that distinguishes high-energy impact models from the canonical model with regard to K isotopic fractionation, as both are partial condensation models.

Conclusion: The equilibrium K isotopic fractionation between condensate and vapor is too small to explain the heavy K isotopic composition of the Moon and kinetic effects make the situation worse. A heavy K isotope enrichment of the Moon is not a straightforward prediction of either high-energy or low-energy impact models.

References: [1] Dauphas N. et al. (2014) *Phil. Trans. R. Soc. A* 372, 20130244. [2] Davis A.M. (2006) In: *Meteorites and the Early Solar System II*, 295-307. [3] Canup R.M., Asphaug E. (2001) *Nature* 412, 708-712. [4] Humayun M., Clayton R.N. (1995) *GCA* 2131-2148. [5] Wang K, Jacobsen S.B. (2016) *Nature* 538, 487-490. [6] Lock S.J., Stewart S.T. (2017) *JGR Planets* 122, 950-982. [7] Čuk M., Stewart S.T. (2012) *Science* 228, 1047-1052. [8] Richter F.M. et al. (2009) *Chemical Geology* 258, 92-103. [9] Canup R.M. et al. (2015) *Nature Geoscience* 8, 918-921. [10] Huang S. et al. (2016) *LPSC* 47, #2261. [11] Petaev M.I. et al. (2016) *LPSC* 47, #2468. [12] Richter F.M. (2004) *GCA* 68, 4971-4992. [13] Dauphas et al. (2015) *EPSL* 427, 236-248.

MAGNESIUM ISOTOPIC FRACTIONATION DURING EVAPORATION OF CAI-LIKE MELTS IN LOW-PRESSURE HYDROGEN GAS AND IN VACUUM: SIMILARITIES AND DIFFERENCES.

R. A. Mendybaev^{1,2}, F.-Z. Teng³, M. Kamibayashi⁴, R. B. Georg⁵, A. M. Davis^{1,2}, S. Tachibana^{4,6}, and F. M. Richter^{1,2}

¹Department of the Geophysical Sciences, ²Center for Cosmochemistry, University of Chicago, Chicago, IL 60637 (ramendyb@uchicago.edu); ³Department of Earth and Space Sciences, University of Washington, Seattle, WA 98195; ⁴Department of Natural History Sciences, Hokkaido University, Sapporo 060-0810, Japan; ⁵Water Quality Center, Trent University, Peterborough, Ontario L1J5Y1, Canada; ⁶UTokyo Organization for Planetary and Space Science (UTOPS), University of Tokyo, Tokyo 113-0033, Japan.

Introduction: The coarse-grained igneous texture of Type B and compact Type A CAIs suggest that their precursors have experienced high-temperature melting event followed by slow cooling. The melting also resulted in evaporation of moderately volatile elements as indicated by their enrichments in heavy Mg and Si isotopes of up to several ‰ in “normal” CAIs, and up to ~40‰ in $\delta^{25}\text{Mg}$ and ~15‰ in $\delta^{29}\text{Si}$ in highly fractionated FUN and Type F CAIs (e.g., [1–2]). The observed isotopic fractionations have been successfully reproduced in vacuum evaporation experiments (e.g., [3–7]). However, it remains unclear if vacuum experiments adequately describe the evaporation process under low-pressure hydrogen conditions of solar nebula. It is known that evaporation kinetics in H_2 -rich gas is much faster than in vacuum (e.g., [4]), but very little is known about the effects on isotopic fractionations. By measuring Mg isotopic composition of evaporation residues from a limited set of experiments at $P_{\text{H}_2}=2\times 10^{-4}$ bar and 1500°C using the old AEI IM-20 ion microprobe at the University of Chicago, it was shown [4] that the obtained Mg isotopic fractionation factor $\alpha_{25,24}=0.98689\pm 0.00071$ is different from the often-assumed $\alpha_{25,24}=\sqrt{24/25}=0.97980$ and closer to the ones from vacuum experiments. The values of $\alpha_{25,24}$ for vacuum evaporation have been since significantly improved by use of modern analytical instruments [5–7], but no new experiments have been conducted in low-pressure H_2 gas.

The purpose of this work was to produce new data on evaporation of CAI-like melts in low-pressure H_2 gas and compare the chemical and isotopic fractionation trends with those from vacuum experiments. The results of the study on evaporation kinetics are reported in a companion abstract by Kamibayashi et al. [8]. Here we discuss if evaporation under such different conditions affects the isotopic fractionation of Mg.

Experimental: As a starting material in the experiments we used CAI4B2 composition, close to those of non-FUN forsterite-bearing CAIs. As there is no measurable chemical and isotopic fractionation in runs a few minutes long at 1600°C in vacuum [5], we considered CAI4B2-1 (see Table) as starting material. Low-pressure H_2 evaporation experiments were conducted at

Hokkaido University. After premelting in 1 atm air the samples were heated in vacuum at 1600°C for 5 minutes followed by continued heating at 1600°C and $P_{\text{H}_2}=2\times 10^{-4}$ bar (see [8] for details). Vacuum experiments were conducted at the University of Chicago using the same protocol as in [5–7].

Texture and chemical composition of the evaporation residues was studied with a TESCAN LYRA3 FIB/FESEM equipped with an Oxford AZtec x-ray microanalysis system. We used the solution technique to measure Mg isotopic composition with a Nu Plasma II [9].

Results and Discussion: Chemical composition of the evaporation residues and their isotopic composition of Mg (relative to DSM3) are shown in the Table below. Despite faster evaporation of Mg and Si (by ~40×) at $P_{\text{H}_2}=2\times 10^{-4}$ bar compared to in vacuum, their evaporation trajectories remain the same as illustrated in Fig. 1.

Sample	time, min	MgO wt%	SiO ₂ wt%	Al ₂ O ₃ wt%	CaO wt%	$\delta^{25}\text{Mg}$ ‰	$\delta^{26}\text{Mg}$ ‰
<i>low P_{H2} experiments</i>							
CAI4B2-2	3	15.37	35.17	27.62	21.85	-0.97	-1.90
CAI4B2-16	10	14.66	33.54	28.90	22.90	0.04	0.06
CAI4B2-12	20	12.62	31.44	30.99	24.96	2.76	5.42
CAI4B2-3	30	3.24	22.15	42.32	32.28	19.70	38.89
CAI4B2-14	35	9.42	28.89	34.16	27.53	7.18	14.09
CAI4B2-10	45	5.54	25.35	38.06	31.06	15.12	29.81
CAI4B2-4	60	0.02	0.73	63.03	36.22		
<i>vacuum experiments</i>							
CAI4B2-1	5	15.71	36.58	26.52	21.19	-1.66	-3.21
CAI4B2-25	300	14.35	34.00	27.92	23.72		
CAI4B2-22	600	12.76	32.13	30.01	25.10		
CAI4B2-21	1200	7.87	27.92	35.47	28.74		
CAI4B2-23	1700	4.02	23.75	40.1	32.13		
CAI4B2-20	1800	0.09	9.40	50.6	39.90		
CAI4B2-24	2100	3.40	22.89	41.27	32.44		
CAI4B2-18	2400	0.00	13.59	48.01	38.40		
CAI4B2-19	3300	0.08	9.89	49.65	40.38		

Figure 2 shows Mg isotopic composition of CAI4B2 residues, expressed as $1000\times \ln(R/R_0)$, where R is $^{24}\text{Mg}/^{25}\text{Mg}$ in a sample and R_0 is their ratio in the starting material, versus a fraction of ^{24}Mg remaining in the residues, expressed as $\ln(f^{24}\text{Mg})$. Figure 2 shows that all samples evaporated at 2×10^{-4} bar H_2 , except for CAI4B2-10, plot on a line with slope of 11.825 ± 0.0931 which results in Mg isotopic fractionation factors $\alpha_{25,24}=0.98818\pm 0.00009$ exactly the same as $\alpha_{25,24}=0.98822\pm 0.00010$ for CAIB melt evaporated at 1600°C in vacuum [5]. CAI4B2-10 appears as an intergrowth of elongated crystals of gehlenitic melilite ($\text{\AA}\sim 10$), that most likely were crystallized during the run, and glass (Fig. 1b in [8]), while all other samples were quenched

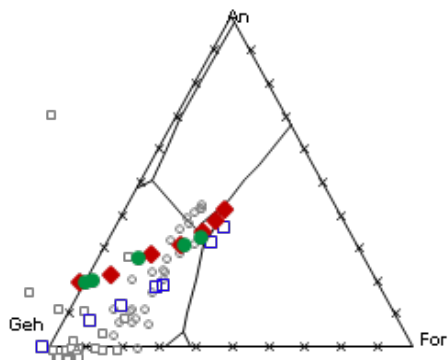


Fig. 1. Evaporation trajectories of CAI4B2 at 2×10^{-4} bar H_2 (red diamonds) and in vacuum experiments (green circles) at 1600°C and 1900°C (open blue squares) [10]. Small grey symbols show compositions of Type B and Type A CAIs.

to clear glasses. It seems possible that some isotopic fractionation could have occurred between the crystalline melilite and the still-evaporating melt during the run which affected the bulk Mg isotopic composition. Therefore, we believe that CAI4B2-10 should not be considered in calculations of the best fit line in Fig. 2.

Figure 3 shows Mg isotopic composition of CAI4B2 residues from low-pressure hydrogen experiments expressed in δ' notation such that $\delta^{25}\text{Mg}' = 1000 \times \ln(\delta^{25}\text{Mg}/1000 + 1)$ and similarly for $\delta^{26}\text{Mg}'$. All experimental residues plot on a well defined line with slope $\beta = 0.51123 \pm 0.00060$ (2std) which is the same as 0.511 of the exponential fractionation line and clearly off the power law (0.501), linear (0.5), ideal Rayleigh (0.516) and equilibrium (0.521) fractionation lines. The value of 0.51123 ± 0.00060 is different from 0.51279 ± 0.00058 [11] obtained from vacuum evaporation experiments with CAIB [5] and FUN [6] melts Mg isotopic composition of which was measured using a Micromass Isoprobe MC-ICPMS. The reason for such differences in fractionation laws is not yet clear. We should note that Mg isotopic composition of FUN2 residues from 1700°C vacuum experiments [12] measured with Nu Plasma MC-ICPMS resulted in fractionation law 0.51234 ± 0.00084 which is the same, within the errors, as 0.51123 ± 0.00060 obtained from our low-pressure H_2 experiments.

Conclusion: By comparing chemical and isotopic compositions of evaporation residues from 1600°C experiments in low-pressure H_2 gas and in vacuum, we conclude: 1) Despite the much faster evaporation of Mg and Si at 2×10^{-4} bar H_2 than in vacuum, their chemical evaporation trajectories remain the same; 2) Evaporation of CAI-like melts in $P_{H_2} = 2 \times 10^{-4}$ bar and in vacuum does not affect Mg isotopic fractionation ($\alpha_{25,24} = 0.98818 \pm 0.00009$ at 1600°C); 3) Mg isotopic fractionation in low-pressure H_2 evaporation experiments

(0.51123 ± 0.00060) follows the exponential law (0.511).

The results presented here for evaporation in $P_{H_2} = 2 \times 10^{-4}$ bars show that chemical and isotopic fractionation is very much the same as in vacuum. Thus previous interpretations of the isotopic fractionation of natural CAIs based on the vacuum experiments remain correct and do not require revisions. One does need to keep in mind that the presence of hydrogen does significantly increase the rate of evaporation [8].

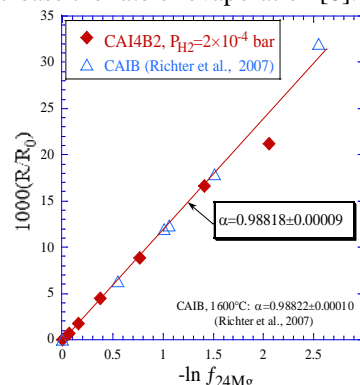


Fig. 2. Mg isotopic compositions of CAI4B2 residues from low-pressure H_2 experiments (red diamonds) vs. fraction of ^{24}Mg remaining in residues relative to CAI4B2-1 ($\delta^{25}\text{Mg} = 0$, $f^{24}\text{Mg} = 1$). CAIB vacuum experiments at 1600°C [5] are shown as open triangles.

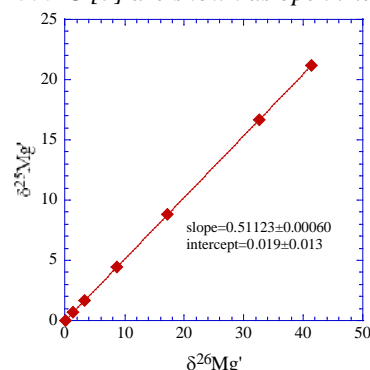


Fig. 3. Mg isotopic composition of residues normalized to CAI4B2-1 ($\delta^{25,26}\text{Mg} = 0$) in the experiments at 2×10^{-4} bar H_2 expressed in δ' notation.

References: [1] Grossman L. et al. (2000) *GCA*, 64, 2879–2894. [2] Williams C. D. et al. (2017) *GCA*, 201, 25–48. [3] Davis A. M. et al. (1990) *Nature*, 347, 655–658; [4] Richter F. M. et al. (2002) *GCA*, 66, 521–540; [5] Richter F. M. et al. (2007) *GCA* 71, 5544–5564; [6] Mendybaev R. A. et al. (2013) *GCA*, 123, 368–384; [7] Mendybaev R. A. et al. (2017) *GCA*, 201, 49–64; [8] Kamibayashi M. et al. (2018) *LPSC 49th* (this volume); [9] Teng F.-Z. et al. (2010) *GCA*, 74, 4150–4166; [10] Mendybaev R. A. and Richter F. M. (2016) *LPSC 47th*, Abstract #2929; [11] Davis A. M. et al. (2015) *GCA*, 158, 245–261; [12] Mendybaev R. A. et al. (2013) *LPSC 44th*, Abstract #3017.

ON THE RARITY OF NEBULAR MATERIALS WITH SOLAR OXYGEN ISOTOPES. L. Kööp^{1,2}, K. Nagashima³, A. M. Davis^{1,2,4}, and A. N. Krot³, ¹Dept. of the Geophysical Sciences, ²Chicago Center for Cosmochemistry, ⁴Enrico Fermi Institute, Univ. of Chicago, Chicago, IL, ³HIGP/SOEST, Univ. of Hawai‘i at Mānoa, Honolulu, HI (E-mail: koeop@uchicago.edu)

Introduction: NASA’s Genesis mission collected and returned with samples of solar wind to Earth. Isotopic measurements revealed that solar wind is ¹⁶O-rich compared to sampled planets (i.e., Earth, Mars) and asteroids. The Sun’s $\Delta^{17}\text{O}$ ($=\delta^{17}\text{O}-0.52\times\delta^{18}\text{O}$) value was inferred to be $-28.4\pm 3.6\%$ (2σ) [1]. While many nebular materials preserved in chondritic meteorites are more ¹⁶O-rich than Earth (e.g., [2–6]), compositions as ¹⁶O-rich as the Sun are exceedingly rare in the meteorite record. For example, most Ca-, Al-rich inclusions (CAIs), the oldest dated materials that formed in the Solar System [7], appear to have formed with a $\Delta^{17}\text{O}$ of $\sim -24\%$ to -23% [2–5], suggesting that a resolved difference exists between the Sun and many of these early formed objects.

Here, we report preliminary O, Ca, Ti, and ²⁶Al-²⁶Mg systematics for a rare CAI (1-2-4) from Murchison with solar O isotopic composition. We also explore the reasons for the scarcity of such objects in the meteorite record.

Methods: O, Al-Mg, and Ca-Ti isotopes were analyzed with the UH Mānoa ims-1280 with conditions similar to those reported in [8], [9], and [5,6,10], respectively.

Results: *Petrologic characteristics:* Mineralogically, CAI 1-2-4 resembles spinel-hibonite inclusions known as SHIBs in CM chondrites [11]. This angular, friable aggregate is $\sim 100\ \mu\text{m}$ across and consists of spinel and hibonite crystals (Fig. 1). Picked from an acid residue of Murchison, voids could be primary or the result of dissolution of silicate minerals. The hibonite grains in this CAI are zoned in MgO and TiO₂, as seen in many SHIBs [5], but usually not in PLAC-type hibonites [6].

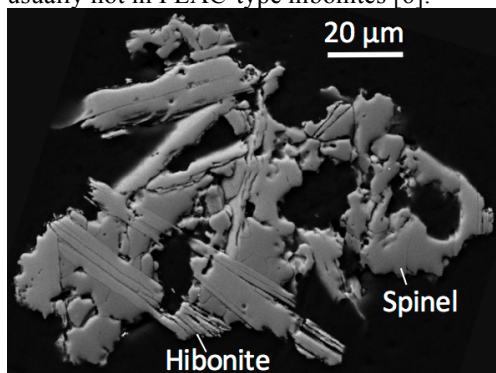


Figure 1. BSE image of CAI 1-2-4.

Oxygen isotopes: CAI 1-2-4 has a $\Delta^{17}\text{O}$ of $-29.1\pm 0.7\%$ (measured in both spinel and hibonite) and is thus as enriched in ¹⁶O as the Sun. The CAI plots slightly to the right of the carbonaceous chondrite anhydrous mineral (CCAM) line along a mass-dependent fractionation trend (Fig. 2).

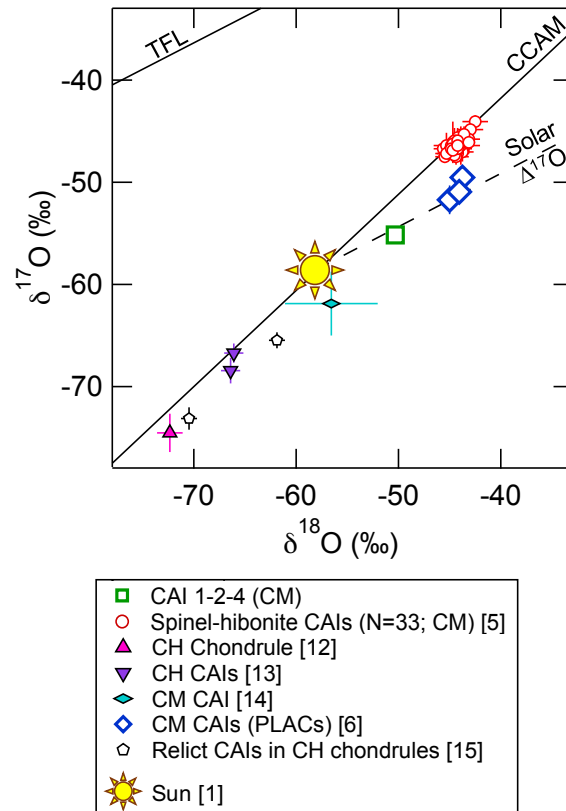


Figure 2. Comparison of O isotopes measured in CAI 1-2-4 with 33 other spinel-hibonite CAIs and with other ¹⁶O-rich Solar System objects, i.e., $\Delta^{17}\text{O}$ lower than common in CAIs.

Ca and Ti isotopes: Two analyses of CAI 1-2-4 reveal depletions in ⁴⁸Ca and ⁵⁰Ti ($-8.1\pm 3.3\%$ and $-11.8\pm 2.4\%$, respectively). These nucleosynthetic anomalies are larger than those in regular, ²⁶Al-rich CAIs from CV chondrites ($|\delta^{50}\text{Ti}|\leq 2\%$ [16]), but are of similar magnitude as those commonly found in FUN CAIs [10], for example. The magnitude of these anomalies is also comparable to ¹⁶O-rich PLAC hibonites [6], for which the range of anomalies decreases with increasing ¹⁶O content (from $>100\%$ at $\Delta^{17}\text{O} \sim -18\%$ to $<10\%$ at $\Delta^{17}\text{O} \sim -28\%$).

²⁶Al-²⁶Mg: Spinel and hibonite analyses show no correlated excesses in ²⁶Mg that would indicate incorporation of live ²⁶Al (Fig. 3). The inferred initial ²⁶Al/²⁷Al is $(0.4\pm 1.5)\times 10^{-6}$. The correlation line has a positive intercept ($\delta^{26}\text{Mg}^*_0 = 1.9\pm 0.2\%$), suggesting either resetting of the ²⁶Al-²⁶Mg system after decay (at least 3.3 Ma after formation of CAIs with canonical ²⁶Al/²⁷Al) or a Mg-iso-

tope anomaly. The latter would be consistent with nucleosynthetic Mg isotopic variation observed in other isotopically anomalous CAIs (e.g., PLAC hibonites and FUN CAIs [e.g., 17]).

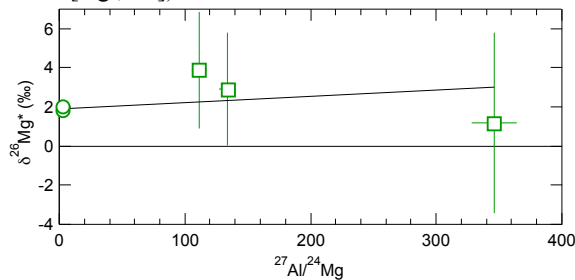


Figure 3. Al-Mg isochron diagram for CAI 1-2-4.

Discussion: Relationship to other SHIBs: While the mineralogy and hibonite mineral chemistry of CAI 1-2-4 resemble those of other CM SHIBs, its isotopic characteristics are unusual. The ^{16}O -enrichment of CAI 1-2-4 is in stark contrast to the 33 SHIBs studied by [5], which cluster at a $\Delta^{17}\text{O}$ of $\sim -23\%$ (Fig. 2a). Twelve of the 33 SHIBs with a $\Delta^{17}\text{O}$ of $\sim -23\%$ have been studied for Ca and Ti isotopes and show no or only marginally resolved anomalies, which is in contrast to the ^{48}Ca and ^{50}Ti depletions found in CAI 1-2-4. The ^{26}Al -poor character is also in contrast to 8 of the 33 SHIBs which were studied for the ^{26}Al - ^{26}Mg system and were found to have $^{26}\text{Al}/^{27}\text{Al} > 1 \times 10^{-5}$ [5]. Isotopically, CAI 1-2-4 is more consistent with PLAC hibonites [6].

^{16}O -rich objects in the meteorite record: CAI 1-2-4 is one of the rare known objects that are as ^{16}O -rich as the Sun. Other objects include a few PLAC hibonites ($\Delta^{17}\text{O}$ between $\sim -26.8\%$ and -28.4% [6]), two hibonite-corundum-bearing objects (A77307-COR-1: $-32.6 \pm 3.2\%$ [18]; BB-5: $-32.5 \pm 4.0\%$ [14]). Five CH chondrite inclusions are more ^{16}O -rich than the Sun ($\Delta^{17}\text{O} \sim -37$ to -32%): a chondrule [12] and four CAIs (two are relicts found in chondrules) [13,15].

The rarity of nebular materials with solar or even more ^{16}O -enriched compositions is not understood. It is noteworthy that CAIs with solar $\Delta^{17}\text{O}$ tend to be among the most refractory examples, but many similarly refractory objects are less enriched in ^{16}O , similar to regular CAIs.

Rarity of ^{16}O -rich CAIs and clustering of others: In self-shielding models (e.g., [19]), the average O isotopic composition of solids is assumed to be solar. In such models, rare CAIs with solar O isotopes could represent objects that (1) formed prior to onset of self-shielding or arrival of ^{16}O -poor water in the CAI formation region, (2) equilibrated with both ^{16}O -rich CO and ^{16}O -poor H_2O at high temperatures, or (3) formed relatively close to the UV source in a region where the wavelength responsible for C^{16}O dissociation had not yet been absorbed. The rarity of ^{16}O -rich objects could perhaps be attributed to an

early formation in scenario 1. However, the vast majority of CAIs have nonsolar O isotopes, indicating that the evolution of solids to ^{16}O -poor compositions had already begun when such CAIs formed. What is puzzling in the self-shielding model is the high frequency of CAIs with a limited range of $\Delta^{17}\text{O}$ values around $\sim -23\%$. Such values are found in both ^{26}Al -rich [3–5] and in some ^{26}Al -poor, isotopically anomalous CAIs [6,10,20], suggesting that conditions were favorable for forming CAIs with uniform, nonsolar O isotopic compositions for an extended period of time or in different regions of the disk.

Alternatively, O isotopic variation may have been primarily driven by inheritance of isotopically distinct primordial gas (^{16}O -rich) and dust (^{16}O -poor) reservoirs [20], ('presolar reservoirs model'), which was favored by [6] due to a relationship between O isotopes and nucleosynthetic anomalies. In this model, CAIs with solar O isotopes represent objects that formed after complete equilibration between primordial dust and gas (e.g., due to full evaporation of primordial dust at a solar dust to gas ratio). The rarity of ^{16}O -rich objects could then be explained if most materials preserved in meteorites formed in a region with dust to gas ratios above solar (e.g., after settling of dust in the midplane) or if temperatures were mostly too low to facilitate efficient equilibration with ^{16}O -rich CO.

Conclusions: We have found a CAI with solar O isotopes, anomalies in ^{48}Ca and ^{50}Ti , and low $^{26}\text{Al}/^{27}\text{Al}$. It is one of the rare examples of Solar System solids that are as ^{16}O -rich as the Sun.

The reasons for the scarcity of solar CAIs and the clustering of many CAIs at comparably ^{16}O -depleted compositions remain unclear. Explanations for the scarcity may be found in the self-shielding and presolar reservoirs models, but the clustering remains a puzzling observation in both models.

References: [1] McKeegan K. D. et al. (2011) *Science*, 332, 1528-1532. [2] Makide K. et al. (2009) *GCA*, 73, 5018-5050. [3] Ushikubo et al., 2011. [4] Bullock et al. (2012), [5] Kööp L. et al. (2016) *GCA*, 184, 151-172. [6] Kööp L. et al. (2016) *GCA*, 189, 70–95. [7] Connelly J. N. et al. (2012) *Science*, 338, 651–655. [8] Nagashima K. et al. (2015) *GCA* 151, 49–67. [9] Park C. et al. (2017) *GCA*, 201, 6–24. [10] Kööp L. et al. (2018) *GCA*, 221, 296–317. [11] Ireland T. (1988) *GCA*, 52, 2827-2839. [12] Kobayashi K. et al. *Geochem. J.*, 37, 663 (2003). [13] Gounelle M. et al. (2009) *ApJ*, 698, L18–L22. [14] Fahey A. J. et al. (1987) *ApJ*, L91–L95. [15] Krot et al. (2017) *GCA*, 201, 185–223. [16] Davis A. M. et al. (2018) *GCA*, 221, 275–295. [17] Liu M.-C. et al. (2009) *GCA*, 73, 5051-5079. [18] Bodéan J.-D. et al. (2014) *LPI Contrib. 1777*, #2025. [19] Lyons J. R. & Young E. D. (2005) *Nature*, 435, 317–320. [20] Krot A. N. et al. (2010) *ApJ*, 713, 1159–1166.

A NEW GLOBAL DATABASE OF MARS RIVER DIMENSIONS.

Edwin S. Kite¹ (kite@uchicago.edu), David P. Mayer^{1*}, Casey J. Duncan², Deirdre Edwards¹

1. University of Chicago. 2 University of Utah. *Now at USGS Astrogeology Science Center, Flagstaff, AZ.

Summary: The scale of ancient Mars rivers – their paleochannel widths and meander wavelengths – is a proxy for past river discharge [1-5]. Discharge, divided by drainage area, yields runoff production, which is a key parameter for selecting between climate models (e.g. rain versus snowmelt).

We will present a new global database of river dimensions for Mars rivers. All of the measured rivers drain catchments of well-preserved drainage area. 172 drainage areas are represented. 50.0% of our sites have HiRISE anaglyphs or DTMs. Repeated ArcGIS traces are merged and analysed in MATLAB. The two main biases in the database are as follows: (1) Because only well-preserved channels are included, the database is biased towards post-Noachian deposits. (2) We measured the largest visible channels in a catchment.

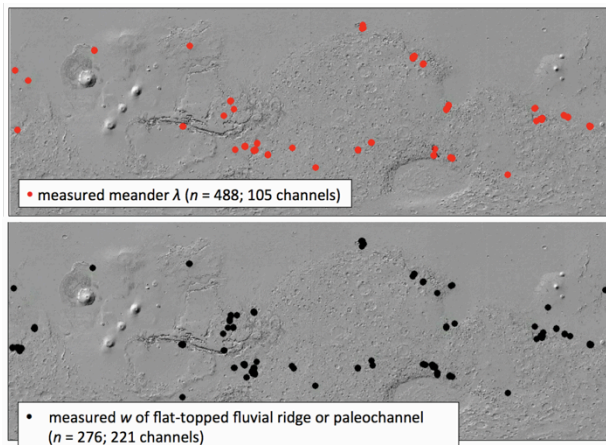


Fig. 1. Locations of sites measured.

Results. Selected preliminary results are shown in Fig. 2; final results will be reported at the conference.

Regional variations and variations with time: Regional variations are less significant than the global trends of (i) large channels that (ii) increase in size with area less rapidly than on Earth. There is a possible trend to smaller river size (for a given catchment area) in the Gale-(Aeolis Planum)-(Zephyria Planum) region relative to the dataset as a whole. All but one of the smallest (<10 km²) catchment areas drain layered sediments in SW Melas Chasma. Those layered sediments are interpreted as airfall. If they are airfall, then the correspondingly small grain size would tend to produce wider channels for a given paleodischarge.

The ages of the measured rivers range from Noachian through Middle Amazonian. At the conference, I will present the results of an ongoing search for trends in runoff production (mm/hr) with geologic epoch.

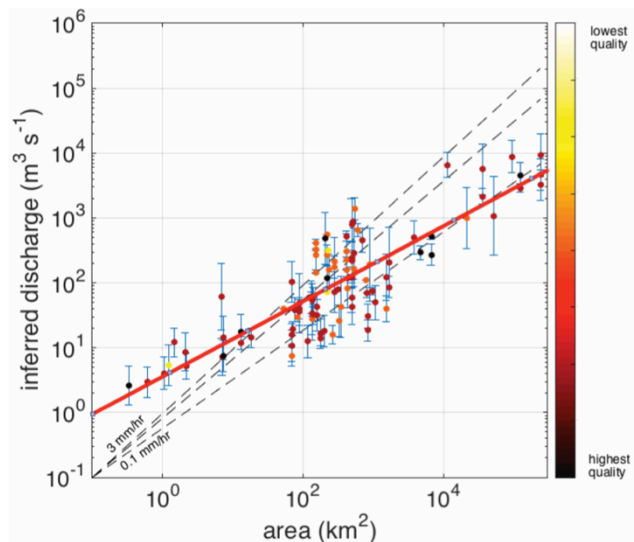


Fig. 2. Meander wavelengths. Discharge inferred using $Q = 0.011 (\lambda / 1.267)^{1.54}$ (ref. 2; but see also 6), where Q is discharge in m³/s and λ is wavelength (m). Paleodischarge inferred using channel width shows similar trends within scatter.

Do the flat tops of sinuous ridges measured from orbit correspond to channel-belt widths, or channel widths? Sinuous ridges near Green River in SE Utah preserve channel deposits and point-bar deposits (Fig. 3). At this site, channel deposits preserved within sinuous ridges can be less than the width of the flat top of the ridge, and in some interpretations the width of the flat top of the ridge corresponds to channel-belt width, not a channel width [7]. These Earth-analog data are a warning against over-interpreting HiRISE DTMs, because the decisive grain-size and bedset-thickness measurements are very difficult from orbit. For many Mars river deposits, the simplest interpretation of sinuous-ridge width is nevertheless that ridge-top width corresponds to inverted channel width. This is because (1) sandblasting-away of floodplain deposits allows diagnostic bedforms, e.g. lateral-accretion deposits, to be recognized from orbit; (2) agreement between meander-wavelengths and paleochannel widths allows cross-checking (but see ref. 6); (3) rivers can transition from negative-relief valley floors to positive-relief channel floors, which decreases the likelihood that either is an artifact.

What causes the large size of Mars channels?: Channels are frequently too big (relative to their drainage area) to be easily reconciled with a seasonal-snowmelt

climate. Here are several possible reasons for big channels:

- Limited image resolution veils smaller channels (Unlikely to be a severe bias for HiRISE).
- Postfluvial modification has enlarged paleochannels. (Cannot explain wide inverted channels, nor large meander wavelengths).
- Reentry heating from distal impact ejecta turned the sky into a griddle, which flash-melted snow and ice [8]. (Cannot transport enough sediment to form alluvial fans).
- Discharges reflect dam-overtopping, not climate-driven runoff. (Unlikely for most sites).
- We see strath terraces or channel amalgamations, not paleochannels [9]. (Plausible for some sites).
- Karst-like modification of paleochannels [10]. (Cannot explain large meander wavelengths).
- Steeper “channels” are debris-flow chutes. (Plausible).

Published work on Earth permafrost-river hydraulic geometry does not support a large permafrost correction [11-13]. We are actively investigating two alternative possibilities: (1) Rivers on Earth adjust their depths to just mobilize sediment (see e.g. ref. 14 vs. ref. 15). Therefore, if grainsize on Mars was small [16], then modest river depths could transport sediment, so discharge could be small for a given width. (2) Rainfall on Early Mars.

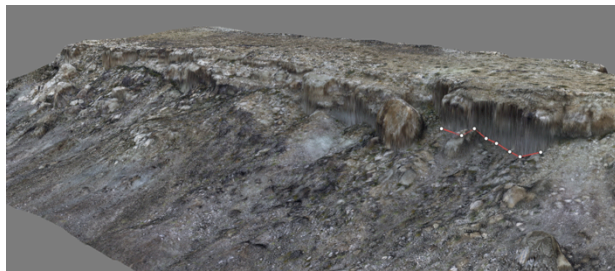


Fig. 3. 3D view of drone-derived Digital Terrain Model (DTM) of SE Utah inverted channel (Oct 2017). Flat top is ~20 m wide. No vertical exaggeration.

Author contributions. E.S.K. analysed Mars data and supervised fieldwork. D.P.M. built the Mars GIS and the Mars DTMs for the project. C.J.D. collected the drone data and built the Earth DTMs. D.E. analysed drone data.

Acknowledgements. Particular thanks to Jonathan Sneed and Sam Holo for contributing to fieldwork. Thanks to Marjorie Chan for logistic and intellectual support for fieldwork. Thanks to the people of the Mars fluvial geomorphology / sedimentology community, especially Becky Williams, Alastair Hayden, Sharon Wilson, Marisa Palucis, Devon Burr, Ross Irwin, Robert

Jacobsen, Caleb Fassett, Nicolas Mangold, David Mohrig, Ben Cardenas, and Roman diBiase. This work was financially supported by the U.S. taxpayer via NASA grants NNX15AM49G and NNX16AG55G.

References. [1] Irwin et al. (2005) *Geology* 33, 489–493. [2] Kite et al. (2015) *Earth & Planetary Science Letters* 420, 55–65 [3] Hajek & Wolinsky (2012) *Sedimentary Geology* 257, 1–30 [4] Burr et al. (2010) *JGR – Planets* J. Geophys. Res. 115 (E7). CiteID E07011 [5] R.M.E. Williams et al. (2009) *Geomorphology* 107, 300–315 [6] Jacobsen & Burr (2018) *Icarus* 302, 407–417 [7] B.R. Nuse (2015) M.S. Thesis, Colorado School of Mines, [8] Goldin, T. J.; Melosh, H. J. (2009), *Geology*, 37, 1135–1138 [9] Hayden, A.; et al. (2017) *48th LPSC*, id.2488 [10] Williams, R., et al. (2017) *GRL* 44, 1669–1678. [11] Hodel (1986) USGS Open File 86-267 [12] Emmett (1972), USGS Open File 72-108 [13] Bieger et al. (2015) *J. Am. Water Resources Assoc.* 51, 842–858 [14] Phillips & Jerolmack, *Science* 2016 [15] Pfeiffer et al. *PNAS* 2017 [16] Haberlah et al. (2010) *Quaternary Science Reviews*. 29, 2673–2693.

MIXED OR LAYERED ICES IN THE OUTER SOLAR NEBULA? F. J. Ciesla¹ and S. Krijt¹, ¹Department of the Geophysical Sciences; University of Chicago; 5734 South Ellis Avenue; Chicago IL 60637; USA (fciesla@uchicago.edu).

Introduction: A major uncertainty in our understanding of the astrochemical evolution of volatiles in the outer solar nebula is the structure of ices on the grains. Often times, ices are treated as being layered, with the most volatile species freezing out last, and thus on top of the less volatile ices. In other studies, the mantles are thought to be mixed, with all species being available to interact with the gas phase; the availability at the surface would just correspond to the abundance of the species in the icy mantle.

Whichever of these pictures is correct is important to discern in developing our understanding of volatile evolution during the early stages of planet formation. It is only the outer-most layers of ice that are able to interact with the surrounding gas or are subject to processes such as photodesorption [e.g. 1]. Further, the ability of certain volatiles to freeze-out onto solids is controlled by the composition of the available substrate. For example, CO is retained by solids much less efficiently when it is frozen out on top of other CO molecules than when it freezes out on top of H₂O [2,3]. Thus the chemical evolution of the outer solar nebula was likely set by the physical properties of the disk.

Here we investigate the formation of an ice mantle as two different species, H₂O and the much more volatile CO, freeze out and are desorbed from a grain as it migrates through the disk in order to determine the likely physical structure of ices in the disk and how this would impact the distribution of volatiles during the early stages of planet formation.

Methodology: As a starting point, we focus on the vertical transport of a grain at a given location of the disk; we will generalize this to two dimensions in the future. We follow the vertical transport] using particle-tracking methods [4,5] to follow how a grain moves through various heights in the disk. The disk is assumed to be in a steady-state with the gas-phase abundance of each species determined by the balance of freeze-out and desorption processes. We have considered a variety of disk structures and properties. For our discussion below, we focus on a region 50 AU from the proto-Sun, at a midplane temperature of 15 K, and with an ambient radiation field of equal to 300x that of the ISM. The vertical temperature profile of the disk is assumed to follow [6], in that below 2 scale heights, the temperature is equal to the midplane temperature and above 3 scale heights the temperature is 3x the midplane temperature. In between, the temperature is found by linear interpolation.

As the grain migrates through these various regions, the loss/gain of CO and H₂O are determined and updated accordingly. In order to track the behavior of each species, the ice covering on the refractory grain core is divided into a mantle and a surface, following [7]. Species on the surface can be exchanged with the gas through adsorption, thermal desorption, and photo-desorption. Mantle species represent surface species which were buried under a newly adsorbed particle. Mantle species can migrate to the surface when a surface species is desorbed.

Results: Figure 1 shows the abundance of the respective species in the gas phase for the case described above. We have assumed that the ices in the disk are originally layered, with a water ice layer surrounding the refractory core and a CO ice layer surrounding it. As a result, water cannot begin to enter the gas phase until all of the CO is lost from the grain, which occurs around 7.5 AU (nearly 2 scale heights) above the disk midplane. If the ices were mixed, water would be more abundant around the disk midplane than assumed here. Thus this is the most conservative assumption.

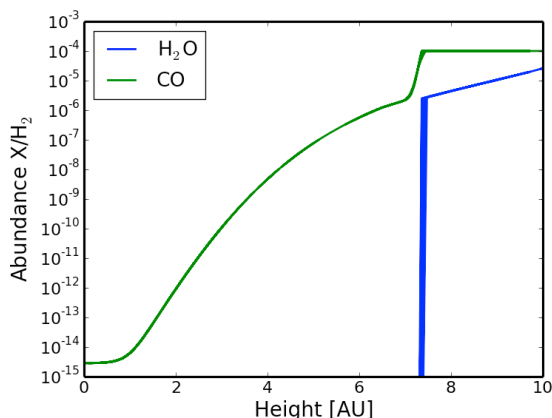


Figure 1: Plot of expected vapor abundances as a function of height above the disk midplane for the model described in the text.

Figure 2 shows the trajectory of a 1 μm grain in the disk, which starts slightly above 3 scale heights (~ 10.5 AU) at the beginning of the simulation. The grain undergoes a random walk in the disk due to the turbulence present (characterized by $\alpha=10^{-3}$), but largely migrates towards the disk midplane due to settling and the higher concentration of mass there [4].

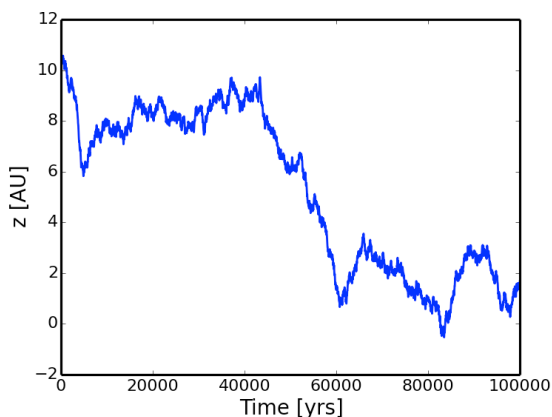


Figure 2: Time evolution of the particle's position above the disk midplane over time.

Comparing Figures 1 and 2, it is seen that the particle migrates above and below the region 7-8 AU above the disk midplane multiple times, providing multiple opportunities for the grain to experience times when freeze-out of solids (and loss from the grain as well). Figure 3 shows the trajectory with a log scale on the x-axis to focus on the early evolution of the particle and the addition of CO and H₂O over time. While water largely accumulates on the grain early, where temperatures are so high in the upper layers that CO does not freeze out, CO is rapidly added once the particle drops to the colder regions of the disk, a few thousand years into the simulation. At this point, it is largely CO that is freezing out, forming a layered structure, though trace amounts of water would be mixed into the CO. However, further upward migration brings the grain to the region where water freezes out on top of the CO layer, for a period lasting until roughly 400,000 years. The deposited water then further buries the CO, possibly trapping it as amorphous ice or leading to more mixing via diffusion within the ice mantle [7].

While all particles are expected to follow unique paths, the example here demonstrates that cycling of grains into the warm molecular-layer of the solar nebula can liberate volatile species and allow them to re-freeze again onto the grains. This would likely cause grains to evolve from a layered structure to a mixed ice structure over time. This effect would be particularly important for volatiles like CO and N₂, whose binding energies (freeze-out temperature) in layered ices (when they bond to themselves) is lower than when they are co-deposited with water in a mixed ice [3]. Thus this effect could effectively trap such volatiles to a greater extent than predicted in models. Further, the mixing of ices would be more significant for species with similar binding energies, rather than the strong differences for CO and H₂O assumed here. This could facilitate reac-

tions between species trapped in ice mantles, and the production of organic molecules by bringing the species together in a water-rich environment [8]. We will continue to quantify this effect and investigate the ability of various ices to be mixed together in the solar nebula.

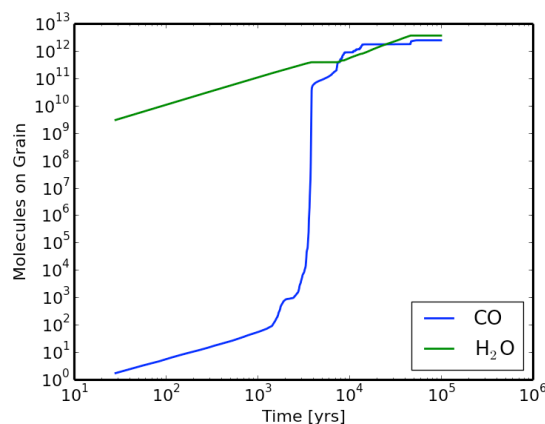
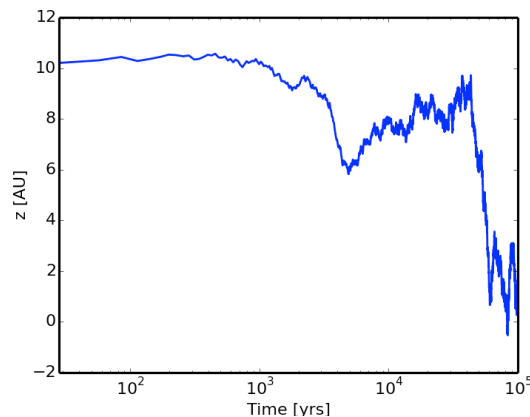


Figure 3: *Top*: Same as Figure 2, but a log scale on the x-axis to highlight the early dynamical behavior of the particle. *Bottom*: Total number of molecules frozen out in the icy mantle of the grain over time. The rapid freeze-out of CO corresponds to the rapid drop in the grains altitude a few thousand years into the simulation.

References: [1] Oberg K. et al. (2009) *A&A* 496, 281-293. [2] Cleaves L. et al. (2014) *Science* 345, 1590-1593. [3] Fayolle E. C. et al. (2016) *Astroph. J. Let.* 816, L28. [4] Ciesla F. J. (2010) *Astroph. J.* 723, 514-529. [5] Ciesla F. J. (2014) *Astroph. J. Let.* 784, L1. [6] Xu R. et al (2017) *Astroph. J.* 835, #162. [7] Fayolle E. C. et al. (2011) *A&A* 529, A74. [8] Fresneau A. et al. (2014) *MNRAS* 443, 2991-3000.

WIDMANSTÄTEN PATTERN RESPONSE TO IMPACTS. R. J. Lyons¹, F. J. Ciesla¹, and N. Dauphas^{1,2}, ¹The Department of the Geophysical Sciences, The University of Chicago, Chicago, Illinois (rjlyons@uchicago.edu), ²Origins Laboratory and Enrico Fermi Institute, The University of Chicago, Chicago, Illinois.

Introduction: Iron meteorites come from the cores of differentiated planetesimals. The Widmanstätten pattern found in these samples developed from the exsolution of kamacite (α , body-centered cubic) from taenite (γ , face-centered cubic) as the core cooled. This growth is temperature dependent, allowing the grain sizes and Ni-concentrations to be used to determine the cooling rate that the core experienced. The cooling rates of these samples provide valuable insight into the thermal evolution and structures of their parent bodies. Early models for the thermal evolution of planetesimals predicted that cores would cool uniformly, such that each part of the core cooled at the same rate, and that these cooling rates indicated the sizes of the planetesimal that each meteorite came from [1]. However, several iron meteorite groups exhibit cooling rates that range over orders of magnitude. For example, IVA iron meteorites have measured cooling rates from 100 to 6600 K/Myr [2], which cannot be produced by a single parent body in the framework of these early models.

Impacts that occur when a body is hot can alter the structures of differentiated planetesimals, eroding the insulating mantle above the core in some regions [3]. Depending on the time of the impact, this can accelerate the rate of cooling that a given body will experience while also leading to orders of magnitude variation in cooling rates in a single core. It is not clear, however, how the formation of the Widmanstätten patterns in these disturbed samples would be affected by changes in cooling rate. If the final Ni concentration profile is different than a non-impacted body the cooling rate of a given sample might be misreported. Here we report preliminary results of our investigation of whether changes in cooling caused by energetic collisions in the early Solar System would lead to distinguishing features in the Widmanstätten patterns in iron meteorites.

Diffusion Model: We follow the 1-D Ni diffusion model described in [4]. The model utilizes a front-tracking, fixed finite-difference grid method described by [5]. We assume kamacite nucleates at regular intervals throughout the melt. The model focuses on the half-distance between two kamacite nucleation sites; this distance is known as the impingement length and is denoted by L . These nucleation sites are assumed to repeat infinitely so no-flux boundary conditions are used. For our undisturbed models, the simulation begins at the nucleation temperature of kamacite (~ 700 C), the cooling rate is held constant, and the material cools to 450 C (below which the diffusion of Ni is negligible). We follow the change in concentration of Ni via diffusion as a

function of time using Fick's second law. The concentration at the interface between the kamacite and the taenite is set by the phase diagram [6]. The interface position is also calculated over time as the concentration profile changes. It is allowed to move to the left or the right depending on the differentials of the Ni concentrations on either side of the interface boundary.

To test the model, we apply it to the simplified, though unphysical, diffusion problem outlined by [7], for which an analytic solution is derived. Figure 1 shows the profile and agreement between our model and the analytic solution. We have also worked to ensure that the results of the code are independent of numerical resolution, and thus are confident in our results.

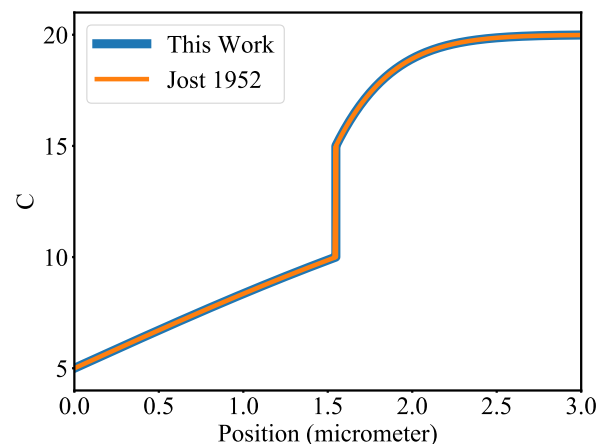


Figure 1: Test of our diffusion model looking at an unphysical situation with an analytical solution determined in Jost 1952. After 1 year of model time our model is nearly identical to the analytic solution.

Preliminary Results: We ran a suite of simulations to determine the final Ni concentration profile in a sample for constant cooling rates between 1 and 10,000 K/Myr. For the runs reported here the impingement length is set to $L=700$ μm with a bulk Ni content of 8.16 wt%, the same as the reference model for the meteorite Toluca [6]. There is also no phosphorus in these simulations. The presence of P would affect the phase diagram and diffusivity of the materials [4,6]. We will be considering these effects in future work, but use this suite of cases as the base models for our initial investigation. Figure 2 is an example of a few constant cooling rate Ni profiles. The large jumps in concentration represent the transition from kamacite (left side) to taenite (right side). As the iron cools the concentration of Ni due to taenite formation at the interface increases. The position of this interface also moves to the right as the

kamacite grows. Note the positions of the half-widths and central Ni concentrations of the taenite bands. The slower the cooling rate the narrower the taenite band and the higher the central Ni concentrations.

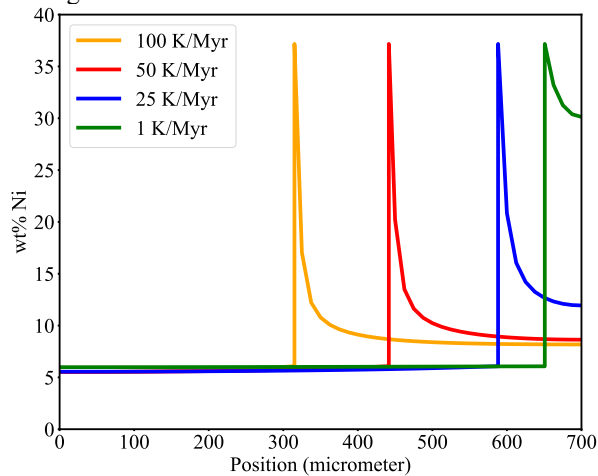


Figure 2: A collection of Ni concentration profiles for constant cooling rates showcasing the positions of the interface and concentrations at the center of the taenite bands.

Previously, we found [3] that an impact onto a 100 km-radius differentiated planetesimal in the early Solar System can erode the insulating mantle and increase the cooling rate of the core by more than an order of magnitude. Specifically, we looked at a head-on impact 50 Myr after the planetesimal's formation. At this time, the mantle has nearly fully solidified but the core is still crystalizing. This increase in cooling rate would occur before the Widmanstätten pattern was fully developed (above temperatures of 450 C). As a result, we have carried out additional simulations, where the cooling rate of the core changes (increases) at some point to determine the effect on the resulting Ni concentration profile.

Figure 3 showcases one such example of this. In this case, the core was assumed to initially be cooling at 10 K/Myr, which is roughly the rate the core of a 100 km-radius planetesimal would cool [1]. During cooling, we increase the cooling rate to 500 K/Myr once the temperature dropped to 575 C, simulating the effects of an impact. Due to the more rapid cooling, Ni has less time to diffuse and for the taenite band to narrow. As a result, the disturbed profile has a wider band of taenite than the constant 10 K/Myr profile, though it is much narrower than the 500 K/Myr profile due to the diffusion that took during the slower cooling at high temperatures. The final half-width of the taenite band can be compared to other constant cooling rate cases, for which we found the closest match to be 23 K/Myr. However, while the band has nearly the same half-width, it does not have

the central taenite Ni content is higher, closer to the 10 K/Myr case.

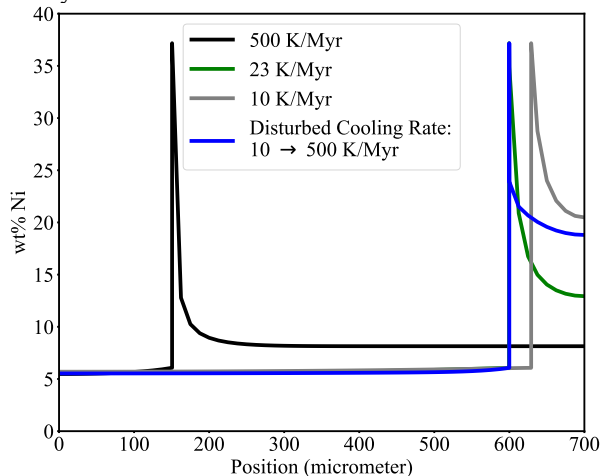


Figure 3: Ni concentration profiles looking at an impacted planetesimal. A 100 km radius body cools at 10 K/Myr (gray line), an impact occurs increasing the cooling rate to 500 K/Myr (black line), and the final impacted profile does not look like either two profiles (blue line). The closest match for the impact profile is that of a 23 K/Myr case (green line).

Discussion/Future Work: Given that impacts between planetesimals are expected to be common within the early Solar System [8], it is likely that some iron meteorite parent bodies should have had their cooling rates disturbed or altered during the development of the Widmanstätten pattern. Thus far, we have seen that a disturbed body may develop a Ni concentration profile with a taenite half-width that matches that of a constant cooling rate. This would lead to erroneous conclusions about the evolution of the parent body. However, the effect of the impact may be identified if the central Ni concentration differs substantially from that predicted by constant cooling rate calculations. We are continuing to explore the wide parameter space to quantify the effects that impacts would have on the properties of the iron meteorites, and will compare our predictions to what is found in the meteoritic data.

References: [1] Haack H. et al. (1990) JGR:SE 95, 5111 [2] Benedix G. K. et al. (2014) ToG 1, 267- 285 [3] Lyons et al. (2017) LPSC [4] Dauphas (2007) MaPS 42, 1597-1613 [5] Crank (1984) Clarendon Press, 425 p. [6] Hopfe and Goldstein (2001) MaPS 36, 135-154 [7] Jost (1952) Academic Press Inc., 558 p. [8] Davison T. M. et al. (2013) MaPS 48, 1894-1918

$^{238}\text{U}/^{235}\text{U}$ IN MARINE CARBONATES AS A TRACER OF PRECAMBRIAN PALEOREDOX CONDITIONS. C. Chen¹, F.L.H Tissot^{1,2}, N. Dauphas¹, A. Bekker³, G.P. Halverson⁴, J. Veizer⁵ ¹Origins Lab, Department of the Geophysical Sciences and Enrico Fermi Institute, The University of Chicago, Chicago, IL (chenxicindy@uchicago.edu), ²Department of the Earth, Atmospheric and Planetary Sciences, MIT, Cambridge, ³Department of Earth Sciences, University of California Riverside, Riverside, CA, ⁴Department of Earth and Planetary Sciences, McGill University, Montreal, Quebec, Canada, ⁵Department of Earth and Environmental Sciences, University of Ottawa, Ottawa, Canada.

Introduction:

The timing and magnitude of the oxygenation of Earth's ocean is still a matter of intense debate. Previous work suggested that the uranium isotope variations recorded in ancient marine sediments, such as shales and carbonates, could provide valuable insights into paleoredox conditions [e.g., 1-11]. In this work, we study U concentration and isotopic composition of a large number of Precambrian carbonates to place constraints on long-term variations in oceanic redox conditions.

Background:

Uranium is a redox-sensitive element that occurs in two main oxidation states in natural waters: U^{4+} and U^{6+} . In the oxic modern ocean, highly soluble U^{6+} exists as a uranyl carbonate complexes [12-14]. In anoxic settings U^{6+} is reduced to U^{4+} , which has low solubility. Precipitation of U under anoxic/euxinic conditions preferentially enriches the sediments in ^{238}U (relative to ^{235}U), resulting in lower $\delta^{238}\text{U}$ values in the residual aqueous U^{6+} form [3,4]. An increase in the extent of oceanic anoxia will thus shift seawater composition towards lower U concentrations and lighter U isotope composition. Furthermore, since the residence time of U in the modern ocean ($\tau \sim 400$ kyr) is much longer than the global ocean mixing time ($\sim 1-2$ kyr), U in seawater is well-mixed and homogeneous vertically and laterally, both in concentration and isotopic composition [5]. It is thus expected that the U isotopic composition of seawater records the global redox conditions.

Quantitative paleoredox reconstructions rely on the capacity of a given paleoredox proxy to capture the global oceanic conditions. This assumption was proven to be valid in the modern ocean for U isotopes [5] and the seawater $\delta^{238}\text{U}$ value reflects the mass balance between riverine inputs and U removal into several sinks with different fractionation factors. The anoxic/euxinic reservoir has the largest fractionation factor compared to other sinks by a factor of three, and consequently the $\delta^{238}\text{U}$ of seawater is largely influenced by the size of the anoxic/euxinic sink: *i.e.*, extent of global oceanic anoxia. As such, estimate of the $\delta^{238}\text{U}$

value of seawater through time will provide constraints on the redox state of the global ocean.

Though black shales were used early on O_2 to track the $\delta^{238}\text{U}$ value of past seawater, marine carbonate is likely to be a more reliable proxy since the fractionation factor associated with the carbonate sink is small [7,15], and varies much less than the one associated with the anoxic/euxinic sink. The wide spatial and temporal distribution of carbonates should make it possible to build a continuous and global record of the redox evolution of Earth's surface environments.

Methods:

In order to reconstruct the long-term redox evolution of the ocean, a large suite of marine carbonates ($n > 200$) are currently being processed for U isotopic analysis (*i.e.*, step-leaching, column chemistry, and high-precision measurement on MC-ICPMS) [see details in 5]. The samples were carefully selected so as to satisfy three crucial criteria: (1) the samples must be marine sediments deposited in the open ocean in order for the U isotopes to record the global seawater signature, (2) the samples must have experienced limited secondary alteration in order to minimize elemental and/or isotopic resetting of the U systematics, (3) the entire sample set must span most of Earth's history, with a high time resolution. We identified the least altered and best-preserved samples based on a combination of petrography and an array of geochemical tracers that reveal the extent of post-depositional resetting of geochemical signatures (Mg/Ca, Sr/Mn, $\delta^{18}\text{O}$ and $\delta^{13}\text{C}$ values) [16,17].

A simple step-leaching approach was developed and we added the amount of 1N HCL to digest only 1% of the samples in order to remove the easily mobilized U, which is more likely to have secondary origin. This can help us access the original $\delta^{238}\text{U}$ signal recorded by the carbonates and minimize artifacts from secondary processes. The remaining bulk carbonates were digested using 1N HCL and insoluble residues were removed via centrifugation.

Results:

Using the two-step leaching protocol, we measured the U concentration and isotope composition of 68 carbonate samples ranging in age from 0.68 Ga to 2.85

Ga. The data obtained so far is presented together with a compilation of literature data in Figure 1.

U concentrations are unvariably low throughout the Archean and most of the Proterozoic. The sample with high [U] at 1.5 Ga is likely an outlier. An increase in [U] seems to start as early as 0.81 Ga, consistent with the rise of atmospheric oxygen level during the Neoproterozoic Oxygenation Event (NOE) as inferred from other paleoredox proxies [18]. No clear secular trend is visible in the $\delta^{238}\text{U}$ values of marine carbonates. While several sample sets record the extensive anoxic conditions with coherently low $\delta^{238}\text{U}$ values at ~ 2.42 Ga as well as at ~ 1.05 Ga, U isotopic composition is quite variable and, taken at face value, the $\delta^{238}\text{U}$ values of many Archean samples would suggest that the Archean oceans were not more extensively anoxic than the Phanerozoic oceans. This is clearly in disagreement with studies focused on other proxies or the U concentrations reported here and in previous studies for Precambrian carbonates and shales. One possible explanation is that in the Archean, U residence time in the oceans was much shorter than what it is today and the U isotopic composition of carbonates was stronger influenced by proximal sources and quantitative uptake in extensively anoxic oceans. In contrast, larger range of U isotope fractionations along with larger [U] recorded by carbonates deposited starting with the NOE might reflect longer seawater U residence time and non-quantitative uptake once extensively developed oxic environments emerged. Our results provide an important baseline for seawater U isotopic composition throughout Earth's history. Further work should be focussed to fill in the remaining gaps in our secular U isotope record of carbonates.

References: [1] Andersen, M. B. et al. (2014) *Earth and Planetary Science Letters*, 400, 184-194. [2] Montoya-Pino C., Weyer S., et al. (2010) *Geology*, 38, 315–318. [3] Weyer S. et al. (2008) *Geochim. Cosmochim Acta*, 53, 845-857. [4] Stirling C.H. et al. (2007) *Earth and Planetary Science Letters*, 264, 208-225. [5] Tissot, F.L.H. and Dauphas, N. (2015) *Geochim. Cosmochim Acta*, 167, 113-143. [6] Brennecka, G.A., et al. (2011) *PNAS*, 108(43), 17631-117634. [7] Romaniello, S.J., et al. (2013) *Chemical Geology*, 362, 305-316. [8] Dahl, T.W., et al. (2014) *Earth and Planetary Science Letters*, 401, 313-326. [9] Azmy, K., et al. (2015) *Palaeogeography, Palaeoclimatology, Palaeoecology*, 440, 440-454. [10] Lau, K.V., et al. (2016a) *PNAS*, 113(9), 2360-2365. [11] Lau, K.V., et al. (2016b) *Earth and Planetary Science Letters*, 485, 282-292. [12] Langmuir, D. (1978) *Geochim. Cosmochim Acta*, 42(6), 547–569. [13] Dong, W.M. and

Brooks, S.C. (2006) *Environmental science & technology* 40, 4689-4695. [14] Endrizzi, F. and Rao, L.F. (2014) *Chem-Eur J* 20, 14499-14506. [15] Tissot, F.L.H. et al. (in prep). [16] Veizer, J. et al. (1989) *Geochim. Cosmochim Acta*, 53(4), 845-857. [17] Veizer, J. et al. (1989) *Geochim. Cosmochim Acta*, 53(4), 859-871. [18] Lyons T.W., et al. (2014) *Nature* 506, 307-315.

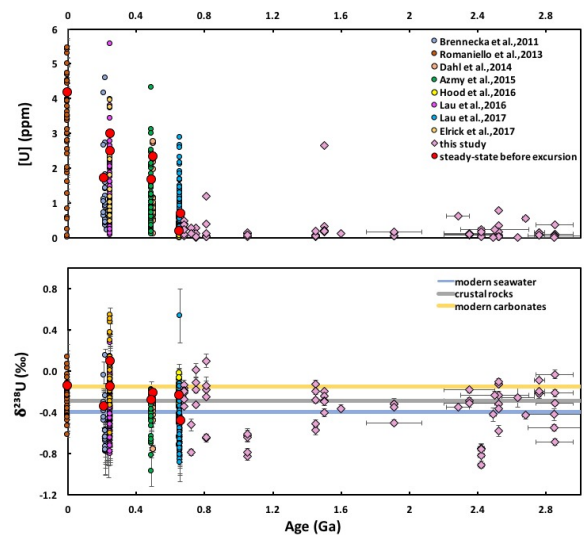


Figure 1: U concentration and isotopic composition as a function of age of the carbonates.

ESTABLISHING THE LIQUID PHASE EQUILIBRIUM OF ANGRITES TO CONSTRAIN THEIR PETROGENESIS. F. L. H. Tissot¹, M. Collinet¹, N. Dauphas² and T. L. Grove¹, ¹Dept. of the Earth, Atmospheric and Planetary Sciences, Massachusetts Institute of Technology, Cambridge, MA, USA (tissot@mit.edu), ²Origins Lab, Dept of the Geophysical Sciences and Enrico Fermi Institute, The University of Chicago, Chicago, IL.

Introduction: Angrites are a series of differentiated meteorites, extremely silica undersaturated and with unusually high Ca and Al contents [1]. They are thought to originate from a small planetesimal parent body of ~ 100-200 km in radius ([2-3]), can be either plutonic (*i.e.*, cumulates) or volcanic (often referred to as quenched) in origin, and their old formation ages (4 to 11 Myr after CAIs) have made them prime anchors to tie the relative chronologies inferred from short-lived radionuclides (*e.g.*, Al-Mg, Mn-Cr, Hf-W) to the absolute Pb-Pb clock [4]. They are also the most volatile element-depleted meteorites available, displaying a K-depletion of a factor of 110 relative to CIs.

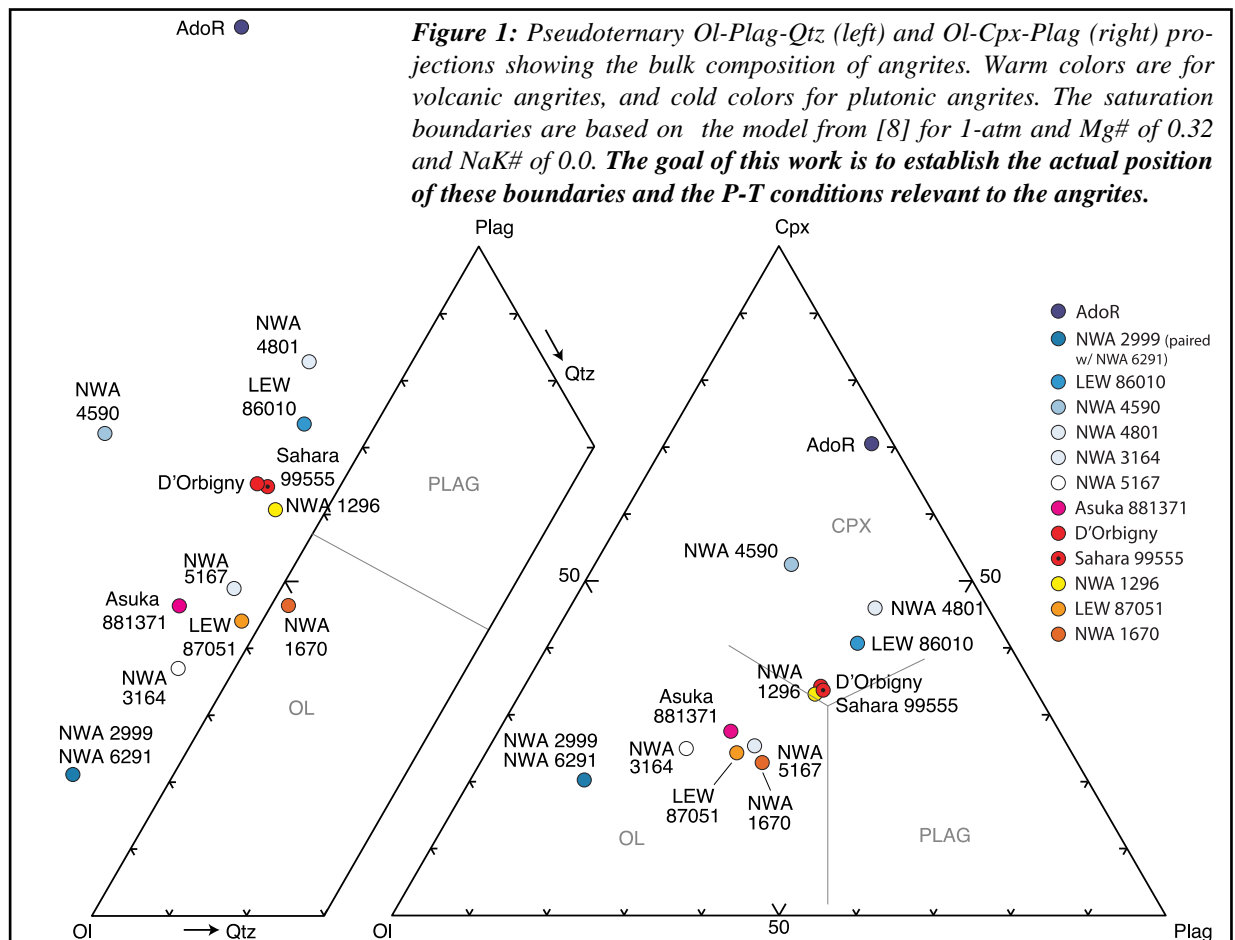
The limited number of angrite specimens available and their unusual chemical compositions have long hindered our understanding of their petrogenesis. The seminal angrite petrogenetic study of Longhi [5] had to rely on the only 4 specimens available at that time,

which included two very similar quenched angrites (Asuka 881371, Lewis Cliff 87051, hereafter LEW 87051), one plutonic angrite (Lewis Cliff 86010, hereafter LEW 86010) and the very atypical plutonic angrite Angra dos Reis (hereafter, AdoR), a 98% pyroxene cumulate.

At this writing, the angrite collection contains 16 different types of angrites and includes 5 plutonic angrites, 9 volcanic angrites, 1 dunitic angrite (Norhtwest Africa 8535, hereafter NWA 8535 [6]) and 1 angrite that might represent an intermediate stage between volcanic and plutonic angrites (Norhtwest Africa 10463, hereafter NWA 10463, [7]). This increased sample set provides us with an opportunity to refine our understanding of the angrite petrogenesis.

Two groups of quenched angrites:

When projected in pseudoquaternary Ol-Cpx-Plag-



Qtz diagrams, two compositional groups appear amongst quenched angrites (Fig. 1). Group 1 contains angrites Asuka 881371, LEW 87051 and Norhtwest Africa 1670 (hereafter, NWA 1670), while Group 2 includes angrites D'Orbigny, Sahara 99555 and Norhtwest Africa 1296 (hereafter, NWA 1296). Group 2 plot very near the Ol-Plag-Cpx-melt 1 atm saturation boundary as predicted by [8] for a liquid with Mg # = 0.32 and NaK # = 0.0 of these angrites. Group 1, on the other hand, is in the olivine primary phase space and calculations of fractional crystallization of olivine from these liquids converges on the composition of the Group 2 [4], at the expected Ol-Plag-Cpx saturation boundary [8]. This relationship between the two quenched angrite groups has been proposed by previous studies on the basis of major and minor element trends in Ol, Cpx and Plag minerals and cooling rates experiments (*e.g.*, [9-11]).

As a first step in deciphering the conditions of magmatic processing experienced by the angrites, the goal of our study is to investigate the phase equilibrium of a natural angrite from Group 2 to determine the actual location of the saturation boundary and the P-T conditions relevant to the composition and fO_2 of the angrites.

Previous experiments:

To date, no experimental studies have been performed on natural angrites to constrain the phase equilibria relevant to the angrite petrogenesis. Previous experimental studies have tried either (i) to produce angritic melt by partial melting of chondrites (*e.g.*, Allende and Murchison, [12-13]) or devolatilized chondrites ([14]), or (ii) to constrain the cooling rates of the quenched angrites by performing crystallization experiments [9, 15]. The only attempt at constraining the phase equilibria of angrites was done by [5], using liquid boundaries and solid solution parameterizations in the CMAS+Fe system (from [16]).

This work:

We have undertaken a series of 1 atm equilibrium experiments on a representative composition of the quenched Group 2 (D'Orbigny) angrites. Starting composition is an oxide mix. The mix was conditioned 3 days in a gas mixing furnace at 1050°C to react the oxides to more stable minerals. Experiments are performed in iron capsules placed in evacuated silica tubes, imposing an oxygen fugacity close to the Quartz-Fayalite-Iron buffer ($fO_2 \sim IW-1$, [17-18]), relevant to the angrite samples, whose fO_2 is thought to be between IW and IW+1 ([19-20]). Our initial results show that on the D'Orbigny composition chosen, the experimental charge is saturated with Olivine (Fo 51),

Anorthite (An 100) and hercynite-spinel (65-35) at near liquidus conditions (1143°C). The experiment contains 13 % olivine, 16 % plagioclase, 71 % liquid and trace amount of spinel. Based on the composition of equilibrium olivine cores and the glass, we calculate equilibrium exchange coefficient between Fe and Mg, Kd_{Ol-Liq}^{Fe-Mg} , of 0.284, in agreement with the range of values for basaltic low-Ti, low alkali melts.

Discussion:

The D'Orbigny angrite is saturated with Ol (Fo 63), Anorthite (An 99.9-100), and Al-Ti bearing diopside-hedenbergite (fassaite). Our experimental charge at 1143°C is saturated with Ol (Fo 51) and Anorthite (An 100), but a fassaite pyroxene has not yet appeared, presumably because the pressure of our experiment is too low and that the actual crystallization pressure must be greater than 1 atm.

Experiments at lower temperatures and higher pressure are underway to determine the conditions of multiple saturation with olivine + anorthite + clinopyroxene for this angrite group. The pressure of angrite multiple saturation could provide new constraints on the minimum size of the angrite parent body. We will report the results of these new experiments at the meeting.

References: [1] Keil, K., (2012) *Chemie der Erde*, **72**, 191-218. [2] Weiss, B.P. et al. (2008) *Science*, **322**, 713-716. [3] Scott, E.R.D. and Bottke, W.F. (2011) *MAPS*, **46**, 1878-1887. [4] Tissot, F.L.H. et al. (2017) *GCA*, **213**, 593-617. [5] Longhi, J. (1999) *GCA* **63**, 573-585. [6] Agee, C. et al. (2015) *LPSC*, abstract #2681. [7] Santos, A. et al. (2016) *LPSC*, abstract #2590. [8] Grove, T.L. et al. (1992) *Mantle Flow and Melt Generation at Mid-Ocean Ridges*, **71**, 281-310. [9] Mikouchi, T. et al. (2000) *LPSC*, abstract #1970. [10] Floss, C. et al. (2003) *GCA*, **67**, 4775-4789. [11] Sanborn M and Wadhwa M. (2010) *LPSC*, abstract #1490. [12] Jurewicz, A.J.G. et al. (1991) *Science*, **252**, 695-698. [13] Jurewicz, A.J.G. et al. (1993) *GCA*, **57**, 2123-2139. [14] Jurewicz, A. et al. (2004) *LPSC*, abstract #1417. [15] Mikouchi, T. et al. (2001) *Met. Soc. Conf.*, abstract #5344. [16] Shi, P. (1992) *Contrib. to Min. and Petro.*, **110**, 139-153. [17] Grove, T.L. and Bence A. (1977). *Lunar and Planetary Science Conference Proceedings*. [18] Krawczynski, M.J. and Grove, T.L. (2012) *GCA*, **79**, 1-19. [19] Brett, R. et al. (1977) *EPSL*, **35**, 363-368. [20] Mckay, G. et al. (1994) *GCA*, **58**, 2911-2919.

Annealing of amorphous water at cryogenic temperature. R. Yokochi¹, ¹ Department of the Geophysical Sciences, The University of Chicago (5734 S. Ellis Avenue, Chicago, IL 60637, USA, yokochi@uchicago.edu)

Introduction: Previous experimental studies reported that amorphous water can efficiently encapsulates ambient gases during its condensation at low temperature and high deposition rates [1,2], reflecting the physical and chemical conditions of the surrounding environment. It was suggested that the gas trapping may be understood as two stage process; gas adsorption onto ice surface and subsequent burial by added layer of ice, based on the pressure-dependent nature of the gas trapping at 77K [3]. In response to moderate heating, the trapped gas may be mobilized if significant change in physical properties of ice, which may affect the degassing profiles of comets if gas-rich amorphous water ice is one of building blocks of comets. Here we investigated the surface property change of amorphous water ice in response to moderate heating, via BET adsorption method using Ar.

Methods: The experimental system (Fig. 1) consists of a cryogenic chamber (V_c), water vapor reservoir (V_w), a gas reservoir (V_g), and pumps, following the basic design of the setup presented in Yokochi et al. [3]. The V_c includes an MKS Baratron gauge (P_g) and a vacuum shielded glass tube that can be cooled at desired temperatures above 12K using a closed-cycle He cryocooler. The tube is cooled by a copper heat conductor, and uncooled section of the tube is heated by a heating wire around 265K in order to minimize the moderately cooled surface area where ice condensation could occur at various intermediate temperatures. The V_w is equipped with a liquid water reservoir and another MKS Baratron gauge (P_w) for determining the quantity of water deposited. A gas pipette is attached to V_g for introducing calibrated aliquots of gas reproducibly into V_c . All components outside the vacuum shroud are maintained at a constant temperature of 313 K. A Lakeshore cryogenic temperature controller controls the temperature of the glass tube using the temperature reading from silicon diode sensors attached to the copper heat exchanger. The temperature inside the glass tube was evaluated based on the vapor pressure of Ar [4]. The deviation of the internal temperature from the sensor reading was between 1.5-1.9 K for a temperature range between 35.1 and 64.3K.

Water vapor was introduced via the leak valve from V_w to V_c to form water ice in the cooled volume. The quantity of deposited water ice was deduced from the pressure before and after the deposition in V_w . Subsequently, calibrated aliquots of gas were introduced to V_c from V_g . The pressure was measured by

P_g after each gas injection. The adsorption isotherm was determined via repeated gas injection and pressure measurements. The effect of annealing was also examined by heating the ice over several hours. The adsorption isotherm was always measured at a constant temperature of 50K after cooling from higher annealing or deposition temperature.

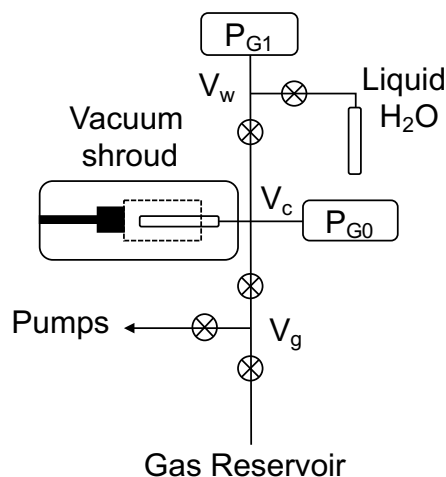


Figure 1: Schematic diagram of the experimental system.

Results: The BET plots of two sets of experiments are shown in Fig. 2a and 2b. The adsorption capacity of amorphous water ice significantly decreased at each 10 K increment heating step: The monolayer capacity decreased by about a factor of 2 after heating at 100K, and by a factor of 10 after heating at 160K where one expect the structural change of ice.

The amorphous ice deposited at different temperatures [50, 60, 70 and 80K] also show systematic difference in the surface adsorption capacity (Fig. 2b). The ice deposited at elevated temperature has lower gas adsorption capacity than the ice deposited at 50K and heated at the same elevated temperature.

Discussions:

The higher adsorption capacity of ice formed at low temperature suggest that the amorphous water ice formed at different temperatures has different structures, and causes higher efficiency of gas trapping at

low temperature, in addition to the temperature effect on gas adsorptions.

Annealing of amorphous water occurs at low temperature, as low as 60 K, and it appears that any heating of ice causes change in surface (and probably structural) properties. It suggests that gas-loaded amorphous water ice, if present in the subsurface of comets, would start releasing gas in response to slight heating, and may cause gradual pore pressure increase. Such effect may have significant bearing on the degassing profiles of comets, and needs to be investigated. Another interesting finding of this work is that the ice formed at moderately temperatures has show relatively high adsorption capacity when cooled. Surface of cooled grains in cold region may host significant quantity of gas, which could subsequently be trapped by such processes as overgrowth.

References: [1] Bar-Nun A., Dror, J., Kochavi, E., Laufer, D. (1987) *Phys. Rev. B* 35, 2427-2435. [2] Nonesco, G., Bar-Nun, A., Owen, T. (2003) *Icarus* 162, 183-189. [3] Yokochi, R., Marboeuf, U., Quirico, E., & Schmitt, B. (2012). *Icarus*, 218(2), 760-770. [4] Fray, N., & Schmitt, B. (2009). *Planetary and Space Science*, 57(14-15), 2053-2080.

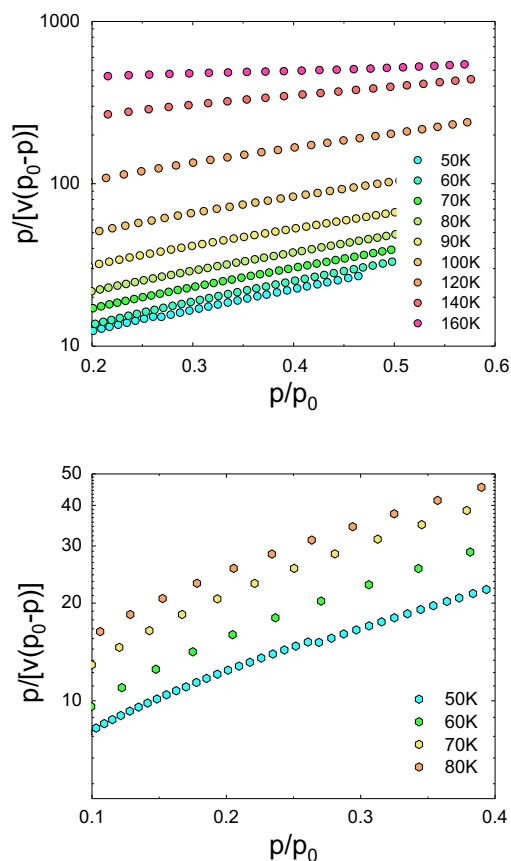


Figure 2: BET plots of adsorption experiments. [Top] Effect of heating on ice deposited at 50K. The [Bottom] Amorphous ice deposited at different temperatures.

I-Xe STUDIES OF AQUEOUS ALTERATION IN THE ALLENDE CAI CURIOS MARIE. O. Pravdivtseva¹, A. Meshik¹, F. L. H. Tissot², N. Dauphas³. ¹Laboratory for Space Sciences and Physics Department, Washington University, CB1105, One Brookings Drive, Saint Louis, MO 63130 (olga@physics.wustl.edu), ²Department of the Earth, Atmospheric and Planetary Sciences, MIT, Cambridge 02139, ³Origins Lab, The University of Chicago.

Introduction: The Allende fine-grained inclusion *Curious Marie* is a unique CAI. It is depleted in uranium but contains large ²³⁵U excess [1], providing new evidence that ²⁴⁷Cm was alive in the Early Solar System, as has been previously suggested [2], and leading to an updated (²⁴⁷Cm/²³⁵U)_{initial} ratio of $(1.1 \pm 0.3) \times 10^{-4}$.

A model initial ²⁶Al/²⁷Al ratio $[(6.2 \pm 0.9) \times 10^{-5}]$ has been calculated for *Curious Marie* using its bulk Al/Mg ratio and the uniform $\delta^{26}\text{Mg}^* \sim +4\text{‰}$ [3] which is similar to the canonical initial solar system value within error. This implies not only an early condensation of the CAI precursor, but also an early onset for the aqueous alteration as well. If this episode of aqueous alteration was responsible for the depletion of U in *Curious Marie*, the initial solar system value for ²⁴⁷Cm/²³⁵U ratio is $(5.6 \pm 0.3) \times 10^{-5}$ [3].

Curious Marie, an extremely altered U-depleted fine-grained CAI, characterized by a group II REE pattern with extensive replacement of high-T phases by low-T alteration products such as nepheline and sodalite. I-Xe chronometry for coarse- and fine-grained Allende CAIs have been previously reported [4,5] with I-Xe ages reflecting the time of alteration. To better delineate the aqueous alteration sequence in Allende CAIs we analyzed Ne, Ar, Kr and Xe isotopic compositions in *Curious Marie* CAI. Here we discuss Xe isotopic composition and the I-Xe chronometry for this sample.

Experimental: 27.1 mg of *Curious Marie* was extracted using dental tools under a stereoscopic microscope. The sample was split into two aliquots, 6.7 mg and 20.4 mg. The smaller one, together with the Shallowater standard, was irradiated in the Missouri University Research Reactor (MURR), receiving $\approx 2 \times 10^{19}$ n/cm².

Xe from irradiated *Curious Marie* CAI was released in step-wise heating extractions in the W coil of our resistance furnace starting with 800°C and up to the melting of Pt (1770°C), with 50°C steps in 1100–1700°C interval. The isotopic composition of the released Xe was measured by high transmission ion-counting mass spectrometry [6] with sensitivity for ¹³²Xe of 5.88×10^{-16} cm³ STP/count. Unirradiated *Curious Marie* CAI was analyzed following the same step-wise heating protocol, but in that sample, we also measured the isotopic compositions of Ne, Ar and Kr.

Results: Xe in both *Curious Marie* aliquots is dominated by natural radiogenic Xe components. Concentrations of ¹²⁹Xe are 3×10^3 higher than the trapped ¹³²Xe, with yet smaller additions of fission Xe. Analyses of the unirradiated *Curious Marie* aliquot revealed ^{80,82}Kr contributions from natural neutron-capture on ^{79,81}Br, with ⁸⁰Kr/⁸²Kr ratio of 2.6, similar to what was previously reported for Allende inclusions [7]. A cosmogenic neutron contribution was also observed as excess ¹²⁸Xe. In the unirradiated sample it resulted in a correlation between radiogenic ¹²⁹Xe (from ¹²⁹I decay) and ¹²⁸Xe (from cosmogenic neutron capture). The ¹²⁹Xe/¹³²Xe versus ¹²⁸Xe/¹³²Xe isochron for the MURR irradiated sample is ~ 1000 greater than for the naturally irradiated sample. This means *Curious Marie* experienced a thermal equivalent cosmogenic neutron fluence of 2×10^{16} n/cm².

Irradiation in the reactor with the thermal neutrons fluence of $\approx 2 \times 10^{19}$ n/cm² results in the ¹²⁸Xe concentrations that are compatible with those for ¹²⁹Xe, with typical ¹²⁹Xe/¹²⁸Xe ratios that are ~ 1 . So, for the irradiated *Curious Marie* CAI, contribution to ¹²⁸Xe from the cosmogenic component constitute only about 0.1% of the total measured ¹²⁸Xe, and its effect on the resulting I-Xe age is negligible. Three-isotope plot for the irradiated *Curious Marie* aliquot is shown in Figure 1.

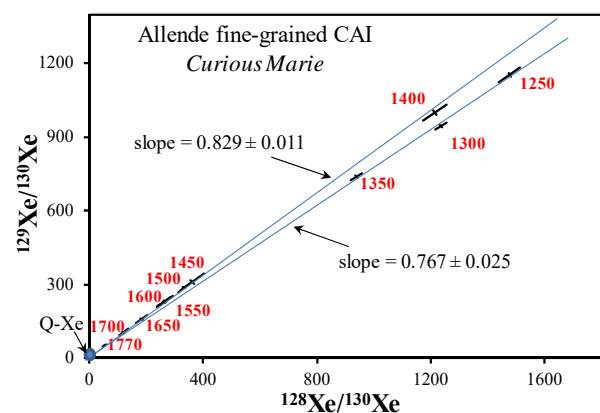


Figure 1. Three-isotope plot for the Allende *Curious Marie* CAI. The I-Xe isochrons (free-fit, not forced through Q-Xe) correspond to low- and high-temperature releases of radiogenic Xe.

Apparently, the I-Xe system survived intact in two different mineral phases in *Curious Marie*, contrary to what was previously observed for Allende CAIs [4]. The difference in slopes of the two isochrons corresponds to a difference in closure times of 1.8 ± 0.4 Ma for these two phases (Fig1), independent of other factors. Relative to the Shallowater standard (4562.4 ± 0.2 Ma [8]), the low- and high-temperature host phases closed 3.2 ± 0.7 Ma and 1.4 ± 0.2 Ma after that standard, corresponding to absolute closure times of 4559.2 ± 0.7 Ma and 4561.0 ± 0.2 Ma.

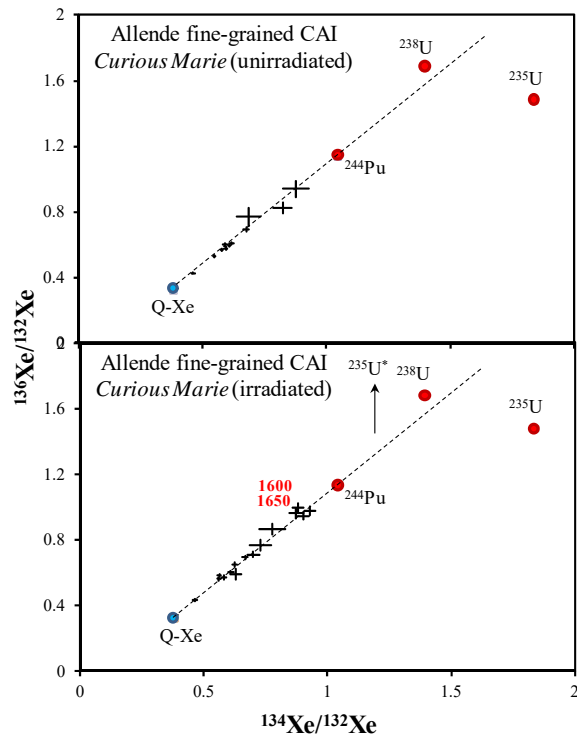


Figure 2. The observed fission compositions in the Allende *Curious Marie* aliquots.

The release profiles of fission Xe differed for the irradiated and unirradiated *Curious Marie* samples, suggesting multiple parent isotopes. Likely parents of fission Xe in meteorites are ^{238}U ($t_{1/2} = 4.47 \times 10^9$ y), ^{244}Pu ($t_{1/2} = 8.0 \times 10^7$ y) and ^{248}Cm ($t_{1/2} = 3.4 \times 10^5$ y) [9]. Presence of live ^{247}Cm at the closure time of the I-Xe system will manifest itself only in the neutron irradiated sample since ^{247}Cm decays into ^{235}U . Both samples have major release peaks corresponding to the low-temperature carrier phase. The observed fission composition in this peak for both samples is consistent with Xe from the spontaneous decay of ^{244}Pu . The release profile of fission ^{132}Xe for the irradiated *Curious Marie* aliquot also had smaller peak at 1600–1650°C temperature steps (Fig.2), most likely due to neutron-induced fission of ^{235}U . ^{136}Xe is always over represent-

ed in the neutron irradiated samples due to neutron capture on live ^{135}Xe ($T_{1/2} = 9.10$ h) ($^{235}\text{U}^*$, Fig.2).

The observed difference in the release profiles of the irradiated and unirradiated *Curious Marie* samples suggests that U is most likely associated with the high-temperature iodine-carrier phase.

Low-temperature iodine-carrier phase in both *Curious Marie* aliquots demonstrated ^{130}Xe excesses that were not accompanied by excesses on ^{124}Xe , expected in case of the spallation contribution (Fig3). We observed similar excess in the same temperature range in one of the previously analyzed fine-grained Allende CAIs [4]. This may well be due to neutron capture on ^{129}Xe , phenomena observed in the (natural) neutron-irradiated Oklo samples [9]. This is, however, also consistent with Xe component of noble gases carried by pre-solar grains of silicon carbide and points to the possibility that pre-solar SiC grains survived in CAIs.

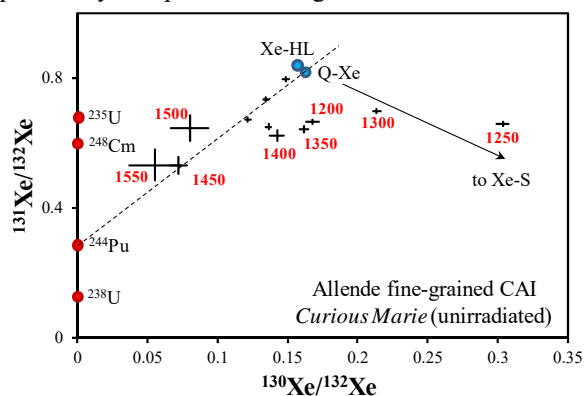


Figure 3. Three-isotope plot for the unirradiated *Curious Marie*.

Curious Marie has proven to be an unusual CAI, where two iodine-carrier phases preserved chronological information. Uranium is most likely associated with a high-temperature phase in this sample. If the I-Xe age of this phase of 4561.0 ± 0.2 Ma reflects the time of U loss, the initial $^{247}\text{Cm}/^{235}\text{U}$ ratio is higher than $(5.6 \pm 0.3) \times 10^{-5}$. The ^{130}Xe excess associated with the low temperature iodine carrier phase suggests that pre-solar SiC may have survived processing of the CAI precursor material.

Supported by NASA grants NNX13AD14G.

References: [1] Tissot F.L. H. et al. (2016) *LPSC* 47, Abstract#1605. [2] Brennecka G. et al. (2010) *Science* 327, 449–451. [3] Tang et al. (2017) *GCA* 207, 1–18. [3] Swindle T. et al. (1988) *GCA* 52, 2215–2229. [4] Pravdivtseva O. et al. (2003) *GCA* 67, 5011–5026. [5] Hohenberg C. M. (1980) *Rev. Sci. Instrum.* 51, 1075–1082. [6] Göbel R. et al. (1982) *GCA* 46, 1777–1792. [7] Pravdivtseva O. et al. (2017). *GCA* 201, 320–330. [8] Ming T. and Anders E. (1988) *GCA* 52, 1235–1244. [9] Meshik A. et al. (2004) *PRL* 93, 182302-1.

THE REE ISOTOPIC COMPOSITIONS OF THE EARTH. J.Y. Hu¹, N. Dauphas¹, F.L.H. Tissot^{1,2}, R. Yokochi^{1,3} and T.J. Ireland¹, ¹Origins Laboratory, Department of the Geophysical Sciences and Enrico Fermi Institute, The University of Chicago, Chicago IL, ²Department of the Earth, Atmospheric and Planetary Sciences, MIT, Cambridge, MA, ³Department of Earth and Environmental Sciences, University of Illinois at Chicago, Chicago, IL.

Introduction: Lanthanides are a group of 14 naturally occurring elements with atomic numbers ranging from 57 (La) to 74 (Lu), which are also known as rare earth elements (REE). REEs are ubiquitous in minerals and rocks. The chemical properties of REEs vary as smooth functions of their atomic numbers, a phenomenon known as the contraction of the lanthanides. This is the main control behind REE fractionation in minerals and rocks. The relative abundance of REEs is usually presented as the REE pattern by normalizing the concentrations in the sample to those in reference materials such as chondrites and shales.

REEs exhibit a significant range in terms of volatilities, with 50% condensation temperatures between 1647 and 1356 K at a total pressure of 10^{-4} bar according to condensation calculations [1]. Highly fractionated type II REE patterns are reported in CAIs and likely to be related to the condensation and evaporation processes that happen in the earliest stage of the solar system. Such process may induce significant isotopic fractionation on individual REEs, which is suggested by Tm abundance anomalies and Ca MDFs in CAIs. The Isotopic signature of CAIs may also be inherited in chondrites and cause planetary isotopic variations. Studying the isotopic fractionation of the REEs will shed light on the processes that occur in the early solar system.

Here we present the first systematic study on MDF of 7 REEs including Ce, Nd, Sm, Eu, Gd, Dy and Yb. The samples that we have analyzed are geostandards and span from high temperature igneous rocks to low temperature samples such as manganese nodules. Based on the samples we have measured, we estimate the isotopic composition of the bulk silicate earth.

Methodology: The samples we have studied here are geostandards which span from high to low temperature including 4 basalts (BCR-2, BHVO-2, BIR-1a, W-2), 1 andesite (AGV-2*), 1 granite (G3), 1 carbonatite (COQ-1), 1 shale (SDC1), 1 limestone (CCH-1) and 2 manganese nodules (NODA-1, NODP-1). To ensure accurate measurement, we have

developed an all-Teflon, pneumatically actuated, high performance liquid chromatography system (FPLC) to purify individual REE from one another [2]. Every sample is first passed through a pre-packed TODGA column to extract REEs from the matrix [3]. The REEs of each sample are then loaded on the FPLC for separation, after which purified REEs are measured on a Thermo Scientific MC-ICPMS upgraded to Neptune Plus specifications with the addition of an OnTool Booster pump. REEs with 4 or more isotopes (Ce, Nd, Sm, Gd, Dy and Yb) are measured via double-spike technique while Eu is analyzed by Dy doping to guarantee that the precision is high enough to distinguish natural isotopic fractionation. All the REE MDFs are reported based on the in-lab isotopic standards that are prepared in the Origins Lab and available upon request.

Results and Discussion: The typical external reproducibility of the REE isotopic analyses is approximately 0.02‰ per amu (Fig. 1). For the samples that have been measured, the natural fractionations of each REE are generally homogeneous, ranging from 0.10 to 0.25‰ per amu. The ranges of fractionations are most prominent for Sm and Eu while heavy REEs do not show large fractionations. No strong relationship is observed between Ce/Eu anomalies and MDFs after considering the curvature of the REE patterns. Two manganese nodules (NODP-1 and NODA-1) show the heaviest Ce isotope composition, which are consistent with the previous study [4]. The estimated average isotopic composition of the bulk silicate earth is -0.02‰ for $\delta^{142/140}\text{Ce}$, -0.02‰ for $\delta^{146/145}\text{Nd}$, -0.18‰ for $\delta^{149/147}\text{Sm}$, +0.34‰ for $\delta^{153/151}\text{Eu}$, +0.06‰ for $\delta^{157/155}\text{Gd}$, 0.00‰ for $\delta^{163/162}\text{Dy}$ and +0.02‰ for $\delta^{174/173}\text{Yb}$.

References: [1] Lodders, K. (2003). The Astrophysical Journal, 591(2), 1220. [2] Ireland (2013) Chemical Geology. 357, 203-214. [3] Pourmand A., Dauphas N. and Ireland T.J. (2012). Chem. Geol. 291, 38-54. [4] Nakada, R., Takahashi, Y., & Tanimizu, M. (2016). Geochimica et Cosmochimica Acta, 181, 89-100.

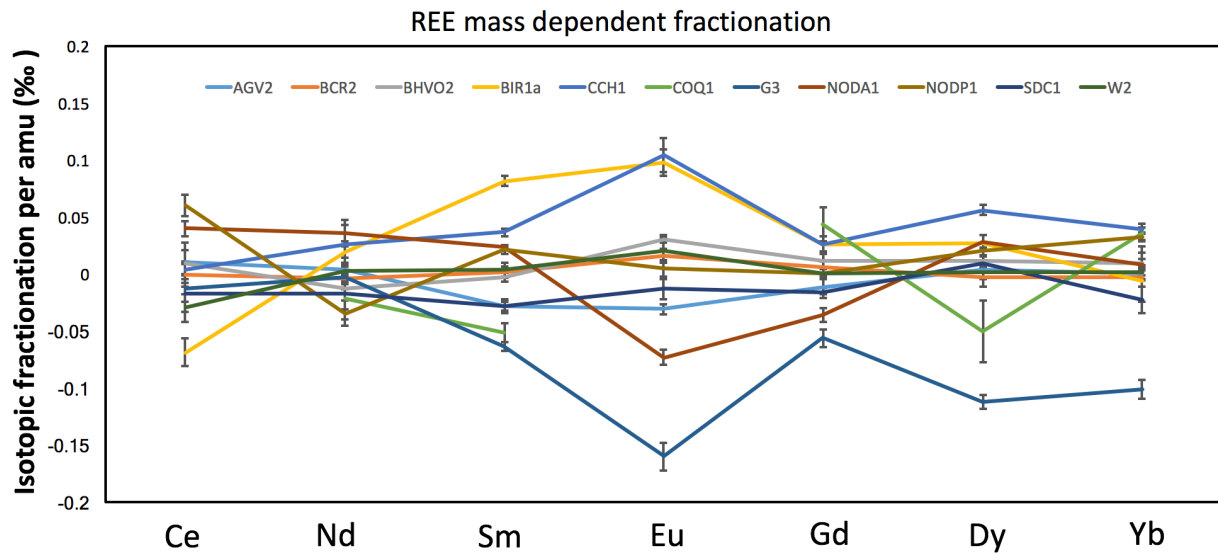


Fig. 1. Isotopic compositions of 7 REEs of geostandards. Y-axis is the isotopic fractionation of REEs per amu after renormalizing to the average of all geostandards.

SEARCHING FOR ANISOTROPIC EROSION IN THE FAN-BEARING CRATERS OF EARLY MARS

J. W. Sneed^{1*}, E. S. Kite¹, D. P. Mayer^{1,2}. ¹University of Chicago, Chicago IL (sneedjw@uchicago.edu)

²United States Geological Survey Astrogeology Science Center, Flagstaff AZ

Introduction: Despite clear evidence of ancient fluvial sedimentary processes, decades of Mars research provide no conclusive account for the presence of warm conditions that could support liquid water on the planetary surface [1][2]. Many of the processes that would account for the proposed transient liquid water on modern Mars would also produce anisotropic slopes [3]. This motivates a search for the fingerprints of similar processes on more ancient slopes. Did transient periods of snowmelt production on slopes with prolonged exposure to direct sunlight influence the development of late Hesperian or early Amazonian basins [4][5]?

If direct sunlight can act as a control on erosion rates by regulating liquid water availability, then anisotropy in slope orientation might be observed in response. In the case of younger, mid-to-high latitude modern processes, pole-facing slopes are systematically gentler than glaciated equator-facing slopes [6]. However, it has not been established whether a similar

process was active in the surface evolution of ancient Mars.

When deeply incised by alluvial fan source regions despite a limited drainage area, circular crater walls provide a natural testing bed, because their modern degraded state may be readily compared to a well-understood initial configuration and because they provide a wide range of exposures at any potential angle. Therefore, we undertake a broad survey of the erosional patterns in such craters in order to look for signs of insolation angle as a major determinant of liquid water availability.

Methods: We examine eight low-latitude crater systems associated with large alluvial fans, as well as either partial or full coverage by 6m-per-pixel CTX stereopairs. These include, e.g., Harris, Ostrov, and Holden craters. Using the NASA Ames stereo pipeline [7], 24m-per-pixel DEM images are extracted and smoothed using a 5-pixel radius gaussian filter to reduce noise and small gaps in coverage. For each pixel,

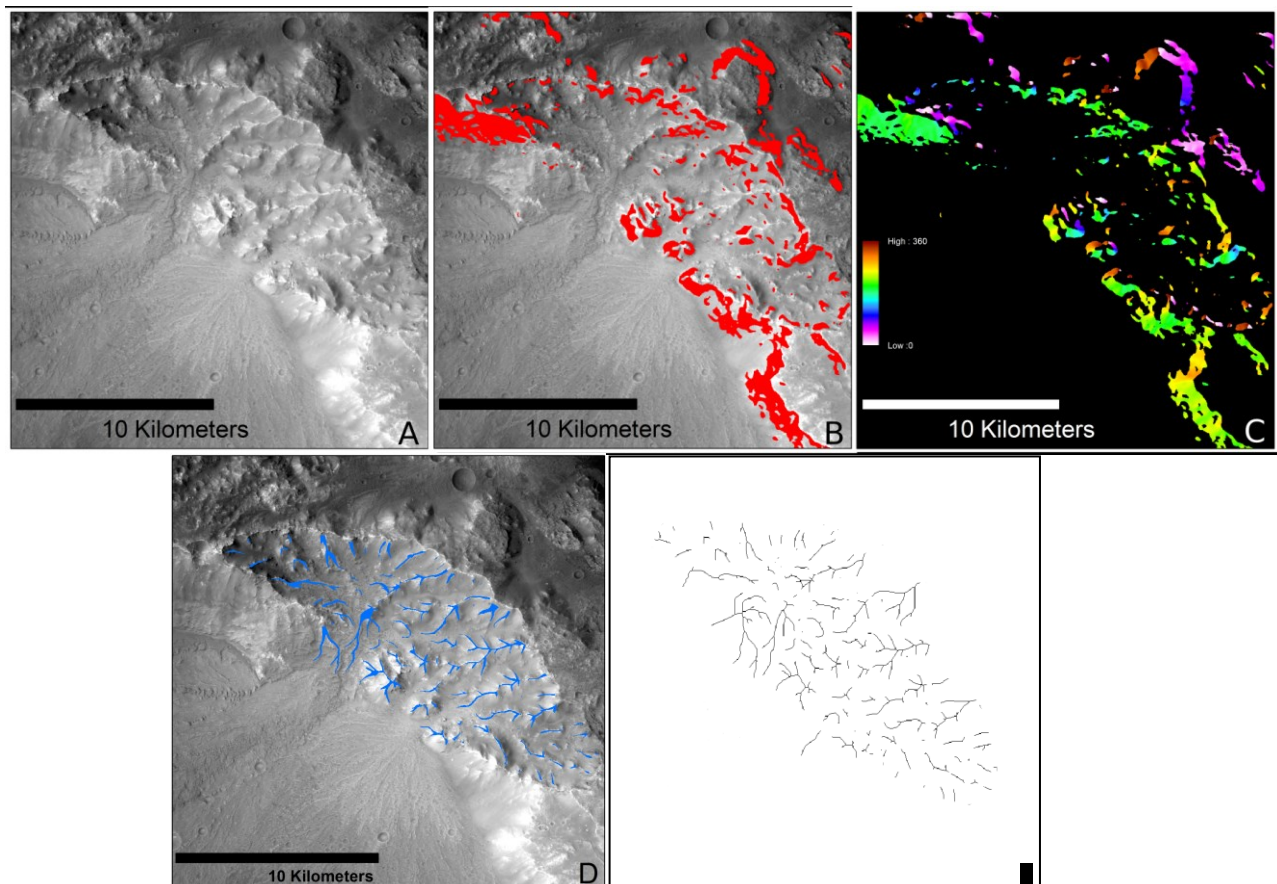


Figure 1: **A:** CTX orthopairs are selected for analysis. B10_013503_1583_XI_21S292W (Harris Crater) shown here. **B:** Using DTM elevation data, we identify each pixel with slope greater than 20° **C:** Direction of slope and angle from crater center are calculated separately for each point. Aspect (clockwise from north) is shown here. **D:** Using D-Infinity drainage modeling of an inverted elevation map, ridgeline zones are identified. **E:** Ridgeline data are skeletonized prior to statistical analysis.

we calculate a slope, aspect, and angle with respect to the crater's center. Pixels with slope $< 20^\circ$ are excluded from this study.

Each pixel value is binned in ten-degree arcs with respect to their angle from the crater center, effectively creating a weighted average of crater wall aspects according to the radial position of each point. Using a Monte Carlo simulation with 10^3 passes, we sample 10^3 points from each bin per pass.

We will present an analysis of this dataset that includes comparison to equatorial craters with few alluvial fans, as a control set.

Preliminary Results: An early survey of 8 craters shows a clear preponderance of north- and south-facing slopes relative to those facing east and west (Fig. 2). In a sample of 36,000 points drawn evenly from each cardinal direction, differences between the most overrepresented and most underrepresented aspect populations reached a factor of ~ 1.4 . However, this effect exists in fresh (non-fan-bearing) craters as well.

Furthermore, this difference appears to be driven almost entirely by high variance in the aspects measured on the east and west slopes of each crater relative to those in the north and south.

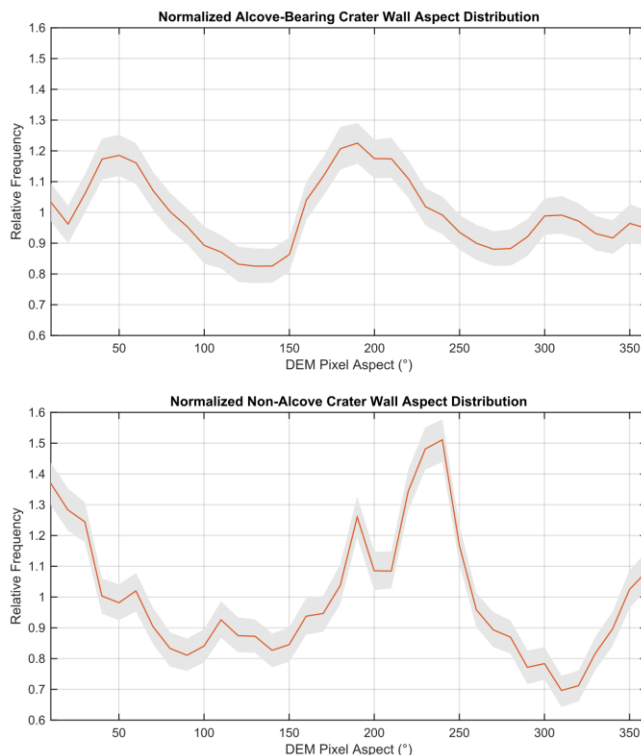


Figure 2: Measured aspect ratios in sampled crater wall sections. 180° = south-facing slopes, 90° = west-facing slopes. Shaded regions show 95% confidence interval in Monte Carlo simulation. **Top:** Alcove walls, **Bottom:** Fresh crater walls (null case). DEM pixel anisotropy shows greater magnitude in fresh craters (NNW orientation) than in fan-bearing alcoves.

Interpretation: Although we find anisotropic aspect frequencies in both alcove and non-alcove crater wall segments, neither of these is higher in amplitude than the null case of fresh crater walls.

Notably, this result diverges from strong anisotropic signals seen in younger features. For example, < 5 Ma gullies show a strong north/south orientation preference, in addition to their preferential incision within (themselves anisotropically oriented) water ice mantles [6].

In order to expand the scope of this investigation, we are further examining ridgeline systems within crater wall alcoves; ridgeline tracing is automated using both raw curvature measures and D-Infinity drainage modeling over inverted elevation maps. We define a ridgeline zone as any pixel with an inverse drainage area of greater than 0.9km^2 . After both curvature and ridgeline data are skeletonized, and the orientation of ridge segments relative to the crater center can be measured in each case.

It would be unexpected if neither snow accumulation, snow runoff production, nor solifluction-driven mass flows showed sensitivity to cardinal direction. Therefore, isotropic aspect frequencies in crater wall alcoves- consistent with our initial results- might suggest substantially different crater wall erosion regimes in the late Hesperian or early Amazonian than those found today. For example, in a much thicker atmosphere, greenhouse warming and turbulent exchange with the atmosphere would reduce the aspect-dependence of snowmelt runoff, and potentially allow for rainfall rather than snowmelt as a source of liquid water for erosion.

Acknowledgments: We are grateful for financial support from the U.S. taxpayer via NASA grants NNX16AG55G and NNX15AM49G.

References: [1] Sagan C, and George M. *Science* 177.4043 (1972): 52-56. [2] Kasting J. *Icarus* 94.1 (1991): 1-13. [3] Kreslavsky M. *Seventh International Conference on Mars*. (2007) [4] Laskar J, et al. *Icarus* 170.2 (2004): 343-364. [5] Kite E, et al. *Icarus* 223.1 (2013): 181-210 [6] Kreslavsky M, and Head J. *GRL* 30.15 (2003). [7] Mayer D, and Kite E. *LPSC*. Vol. 47. 2016.